Expansions in the Non-Ideal Compressible Flow Regime

A Numerical and Experimental Study

Gayathri Hariharan

TU Delft
Delft University of Technology

Propulsion & Power

Expansions in the Non-Ideal Compressible Flow Regime

A Numerical and Experimental Study.

by
Gayathri Hariharan

to obtain the degree of Master of Science
at the Delft University of Technology,
to be defended publicly on Oct 25, 2021 at 9:30 am.

Student number:	5023351	
Project duration:	Jan. 2021 - Oct. 2021	
Thesis committee:	Associate Prof. Rene Pecnik,	TU Delft, Chair & Supervisor
	Assistant Prof. Matteo Pini,	TU Delft, Responsible supervisor
	Dr. A. J. Head,	TU Delft, Daily Supervisor

An electronic version of this thesis is available at
http://repository.tudelft.nl/.

TU Delft

Abstract

Organic Rankine Cycle systems are gaining increasing attention as a modular, cost-effective and decentralised thermal energy recovery solution. The design of an efficient expander in the ORC system is crucial to its rapid uptake by the industry. Compared to volumetric expanders, a radial turbine provides advantages in terms of flexibility and better part-load performances. The design of ORC radial turbines is faced with two challenges. Firstly, the expansion in the stator occurs close to the vapour-liquid dome and the critical point, where the ideal gas assumption is no longer valid. Such expansions fall under the Non-ideal thermodynamic regime. Secondly, due to the lower speed of sound in the working fluid, the expansions are supersonic and are accompanied by compressible flow features such as shock waves, expansion fans which generate entropy and reduce the performance of the expander. There exists significant validated design methodologies and empirical relations for conventional turbomachinery. However this is not the case for unconventional turbomachinery where established loss correlations are not applicable. Hence, there is a knowledge gap in validated design tools for unconventional turbomachinery like ORC radial turbines. The thesis forms a part of the validation campaign of the open-source flow solver, SU2 and approaches the exercise by studying expansions in two paradigmatic test cases, namely (i) a linear stator cascade and (ii) a converging - diverging nozzle.

The study of expansions through a linear cascade is a preceding step to the study of a rotating radial turbine. Consequently, a RANS simulation on the single channel blade passage is studied under the validated assumption of flow periodicity. The expansion takes place from inlet total conditions of 18.4 bara and 525 K (Z =0.558) to a static pressure of 1.95 bara (Z = 0.951) and exit flow of Mach 2. Two types of response quantities are studied namely direct and system response quantities. Direct response quantities are those that can be measured directly such as the pressure, Mach, density. System response quantities are derived from direct measurements and provide information to characterise the performance of the stator. The selected system response quantities are: (i) Pressure loss coefficient (C_p= 0.074), (ii) Kinetic energy loss coefficient (ζ_{KE}=0.115), (iii) Entropy loss coefficient (ζ_s=0.118), (iv) Base pressure loss coefficient (C_{pb}= -0.065), (v) Standard deviation of exit flow angle ($\sigma_{\beta 2}$ = 1.244) and (vi) Standard deviation of exit Mach (σ_{M2}= 0.033). Experimentally, it is possible to measure the pressure loss coefficient, base pressure loss coefficient and the flow uniformity at the outlet using a combination of pressure and direct velocity measurements. Through a Design of Experiments approach, the sensitivity of the flow to input uncertainties was studied through a stochastic collocation based forward propagation of the uncertainty. The input uncertainties considered are the inlet total pressure, fluid viscosity and critical point properties. The Sobol indices from the uncertainty quantification indicate the more dominant influence of the critical point properties over other inputs considered. The results also validate the use of a constant viscosity assumption for the RANS simulation. The subsequent planned unit test case was to characterise the expansion through an optimised stator blade row. To this end, a deterministic adjoint based optimisation was performed with the objective function of minimising entropy generation. The resulting geometry was studied and resulted in a pressure loss coefficient improvement of around 4%, although stator flow uniformity at the exit was compromised. The uncertainty quantification performed on the optimised blade geometry yielded robustness improvements on the pressure loss coefficient and reduction in uncertainties associated with direct response quantities, although no strong correlations can be drawn between the improvements in uncertainty and the deterministic optimisation. Given current machining tolerances, the realisation of such a negligible geometry change is not viable from an experimental perspective.

The second section of the thesis deals with experimental investigation of expansions in a converging-diverging nozzle through a matrix of isobars with increasing degree on non-ideality. Two isentropes with inlet pressure of 2.73 bara (Z = 0.9526) and 6 bara (Z = 0.901) with pressure ratio of 8.76 were performed with recording of pressure, temperature, flowrate and density measurements along the ORCHID. The flow field was visualised using the schlieren method using a z-type layout. The thesis reports the first measurements of total pressure before the nozzle inlet and vapour density and flowrate measurements. The experimental data was post-processed to identify steady-state and quantify the Type A and Type B uncertainties. The schlieren images were used to extract information on the Mach distribution along the nozzle mid-plane using an in-house line extraction tool. Lastly, a 2.5° wedge at the exit of the nozzle is used to generate oblique shock waves that are then manually measured. The flow field at the exit of the nozzle is in the ideal region where the shock

angle only depends on upstream Mach number. Hence, the experimentally observed oblique shock angles for the off-design case are close to on-design (Inlet pressure = 18.4 bara) predictions.

Acknowledgements

This report is the culmination of the tasks performed over a duration of 9 months for the MSc thesis. I would like to extend my gratitude to Dr. Rene Pecnik and Dr. Matteo Pini for supervising the project progress. Through the course of the thesis, I had help from an army of people at the P&P group. I would like to thank Nitish Anand for helping us troubleshoot any SU2 roadblocks and providing us with the optimised geometry. Thank you, Matteo Majer for your readiness to answer even my seemingly mundane doubts regarding the simulations. My gratitude goes to Fabio Beltrame for helping me post-process the schlieren images. Thank you Theo, for explaining the experimental procedure, helping us with the calibration and the post-processing of the images. I would also like to thank Riccardo Vello for patiently initiating me into the project.

Lastly, this entire thesis would not have been possible without the constant guidance and support of my mentor Dr. Adam Head. Thank you for being a patient guide, right from helping me selecting a thesis topic to reviewing this document even during your break. Working with you has been an inspiring journey and I hope our paths cross again.

Contents

List of Figures

List of Tables

Glossary

Acronyms

ASME American Society Of Mechanical Engineers. 18
CFD Computational Fluid Dynamics. 2, 18
DAQ Data Acquisition. 74
DAQC Data Acquisition And Control. 51
DOE Design Of Experiments. 23
DRQ Direct Response Quantities. 31
ECS Extended Corresponding States. 11
EOS Equation Of State. 9
JANNAF Joint Army Navy NASA And Air Force. 10
JST Jameson-Schmidt-Turkel. 30
NICFD Non-ideal Compressible Fluid Dynamics. ix, 2, 8, 24
ORC Organic Rankine Cycle. 2, 5, 74
ORCHID Organic Rankine Cycle Hybrid Integrated Device. 2, 47
PID Process And Instrumentation Diagram. 48
PIV Particle Image Velocimetry. 73
PRSV Peng-Robinson EoS Modified By Stryjek And Vera. 9
SA Spalart–Allmaras Turbulence Model. 29
SRQ System Response Quantities. 32
SU2 SU2 Multiphysics Simulation And Design Software. 2
T-S Temperature Entropy. xi, 6, 56
UMG2 Unstructured Mesh Generator 2 Dimensional. 28
UQ Uncertainty Quantification. 20, 27, 73
VBD Variance Based Decomposition. 31

Notation

Refractive index	n	[-].	53
Isobaric heat capacity	C_p	[kJ /kg.K].	10, 14
Enthalpy	h	[kJ/kg].	14
Thermal conductivity	k	[-].	11
Mach number	M	[-].	13
Pressure	p	[Pa].	6
Temperature	T	[C].	6
Specific volume	v	[m^3/kg].	6
Compressibility factor	Z	[-].	6
Specific gas constant	R	[J /kg.K].	6
Reduced pressure	p_r	[-].	7
Reduced temperature	T_r	[-].	7
Shock wave angle	β	[deg].	15, 68
Ideal specific heat ratio	γ	[-].	7
Fundamental derivative	Γ	[-].	8
Density	ρ	[kg/m^3].	12
Expansion angle	μ	[deg].	15
Viscosity	μ^v	[kg/(m s)].	11
Acentric factor	ω	[-].	10, 12
Density ratio	v	[-].	16
Prandtl meyer function	v	[-].	16
Simulation error	δ_S	[-].	18

Experimental error	δ_D	[-].	18

Subscripts

Critical	cr	6	**Property before shock**	1	13
Departure	d	11	**Property after shock**	2	13

1 Introduction

1.1. Motivation

Global energy demand has experienced exponential growth due to increased population and economic growth. The International Energy Agency (IEA) predicts almost 50% growth is energy demand between 2018-2050 [73]. In the current energy scenario, almost two-thirds of the global greenhouse gas emissions can be traced to energy production. Therefore, there is a strong need to decarbonise energy production.

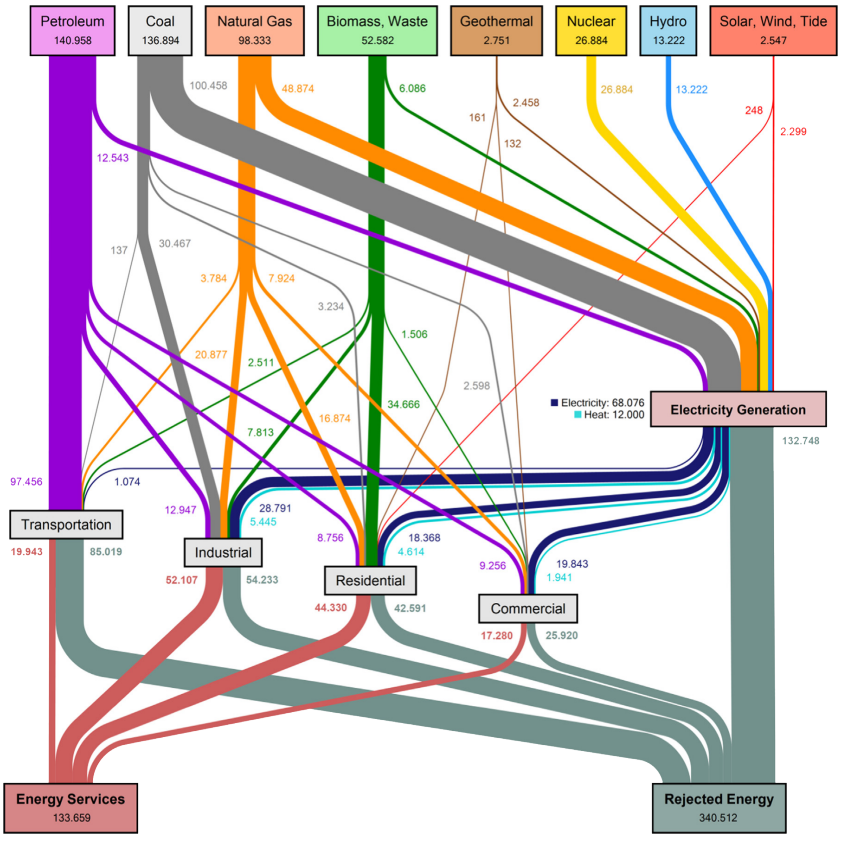

Figure 1.1: Estimated world energy use of 2021 in PJ. Taken from [36].

For instance, the Roadmap 2050 project of the European Climate Foundation [80] proposes the following modifications to the current energy system: (i) a decrease in the energy intensity of buildings and industry, (ii) electrification of processes for instance in transportation and space heating, (iii) clean power generation by a massive shift toward renewable energies, comprising wind energy, PV, CSP, biomass, geothermal and large

hydro projects and, (iv) A reinforcement of the grid capacity and inter-regional transmission lines to absorb daily and seasonal fluctuations. **O**rganic **R**ankine **C**ycle (organic Rankine cycle (ORC)) systems are a viable solution for objectives (i) and (iii). Figure 1.1 depicts the flow of energy from various sources to energy services. A significant amount of energy is rejected as waste heat. A significant proportion of this rejected heat is low- medium grade waste heat as well that cannot be recovered through conventional steam Rankine cycles. For such applications, ORC systems which employ working fluids with higher molecular mass and lower boiling points compared to water can be employed. ORC systems offer modularity, flexibility and scalability [96].
The expander of the ORC system is vital to the system's overall performance and efficienct. Amongst available options such as scroll expanders, radial turbines etc., radial inflow turbines are the optimum choice due to its compactness, high power density and capability of operating with high flow coefficient at rotor outlet [31]. However, the combined effect of high-pressure ratio and low speed of sound in the organic vapours results in supersonic flow in the stator and transonic flow in the rotor. Supersonic flow in the stator is characterised by flow features such as shock waves that generate losses and reduce overall efficiency. Additionally, the expansion occurs close to the liquid-vapour dome where the conventionally used Ideal Gas law is not valid. Therefore, conventional design guidelines cannot be employed to design ORC expanders and there is a knowledge gap for validated numerical tools for design of machinery operating in this regime of non-ideal compressible fluid dynamics (NICFD). Experimental facilities like the organic Rankine cycle hybrid integrated device (ORCHID) at the Propulsion & Power laboratory, TU Delft aim to bridge this gap by enabling the study of expansion of organic vapours through an expander. The purpose of the experimental facility is to: (i) validate computational fluid dynamic (computational fluid dynamics (CFD)) design tools, (ii) validate CFD based design methodologies (like adjoint based shape optimisation) and (iii) calibrate loss correlations to enhance reliability of preliminary design methods [5]. Once validated, these design tools will enable more robust design of ORC machines. The present research work contributes to the validation framework for the open source CFD suite, SU2 multiphysics simulation and design software (SU2) [35].

1.2. Research Questions & Scope of Work

The objective of the thesis is to advance the validation program for the open source flow solver SU2. This is done by a hierarchical approach where simplified flow unit cases such as a converging-diverging nozzle or a linear cascade is numerically modelled and validated against well designed experiments. Within this context, the overarching research question is,

"Can the SU2 flow solver accurately predict the flow field of supersonic test cases operating in non-ideal flow conditions for complex geometries?"

The primary research question consists of the following subquestions:

1. ***What are the relevant metrics to characterise the performance of the stator?***
   A numerical validation infrastructure for the proposed linear cascade section has been created [103]. Only direct response quantities such as static pressure and Mach numbers have been studied. Metrics such as loss coefficients, flow uniformity parameters at the stator outlet can quantify the performance of the blade design and assist in developing correlated loss coefficients. This research will identify and study such system response metrics and quantify the uncertainty arising from model input uncertainties.

2. ***What are the optimal design of experiments needed to assess the capabilities of the adjoint-based solver?***
   With increase in computational power, application of optimisation methods to turbomachinery design has gained unprecedented attention. One of the many available tools, is the discrete adjoint based shape optimisation method. The optimisation is performed with a single objective function making it a deterministic optimisation. ORC systems are subject to fluctuating operating conditions. In this case, a multi-point optimisation can provide more robust designs. Such a method is computationally expensive. Thus, this thesis aims to understand how a deterministically optimised design behaves under the effect of model input uncertainties. The robustness of the optimised design can also be experimentally validated in future experiments at the ORCHID.

3. ***Can the shockwave angle be accurately quantified and provide useful information for code valida-***

tion? What is the impact of nozzle geometry on response quantities?
The last subquestion is experimental in nature and deals with the installed nozzle geometry with a wedge at the exit that generates oblique shock waves. Quantifying the shock wave angle, pressure and Mach from experiments and comparing them to numerical simulations will complete the validation framework for simple Euler flows through nozzles. The thesis will also report improvements that resolve shortcomings from previous runs.

Chapter 3 answers research questions 1 and 2 while Chapter 4 reports the experimental observations for subquestion 3. The novelty of the work done in this thesis can be categorised and detailed as follows:

- **Numerical Scope:** The thesis contributed to extending the capabilities of the numerical infrastructure to compute system performance metrics like loss coefficients. Additionally, the work is a first step in assessing the robustness of single-point adjoint optimised stator design under the effect of model input uncertainties.
- **Experimental Scope:** The thesis reports the measurements and associates uncertainties of newly installed measuring devices at the ORCHID. A novel nozzle geometry characterisation method is reported. Lastly, a discussion on standardised steady state estimation methods is presented.

1.3. Report Overview

Figure 1.2 shows a hierarchy from the radial inflow turbine expander in a typical ORC system. The stator section of the turbine can be simplified into a stack of stator blades forming a linear cascade test section. The flow passage between the stator blades is a converging-diverging nozzle that is designed based on the Method of Characteristics. Chapter 1 and chapter 2 provide the motivation, context and relevant background literature for the thesis. Chapter 3 deals with the numerical investigation of flow through the stator linear cascade while chapter 4 discusses the experiments performed in a converging diverging nozzle installed at the ORCHID.

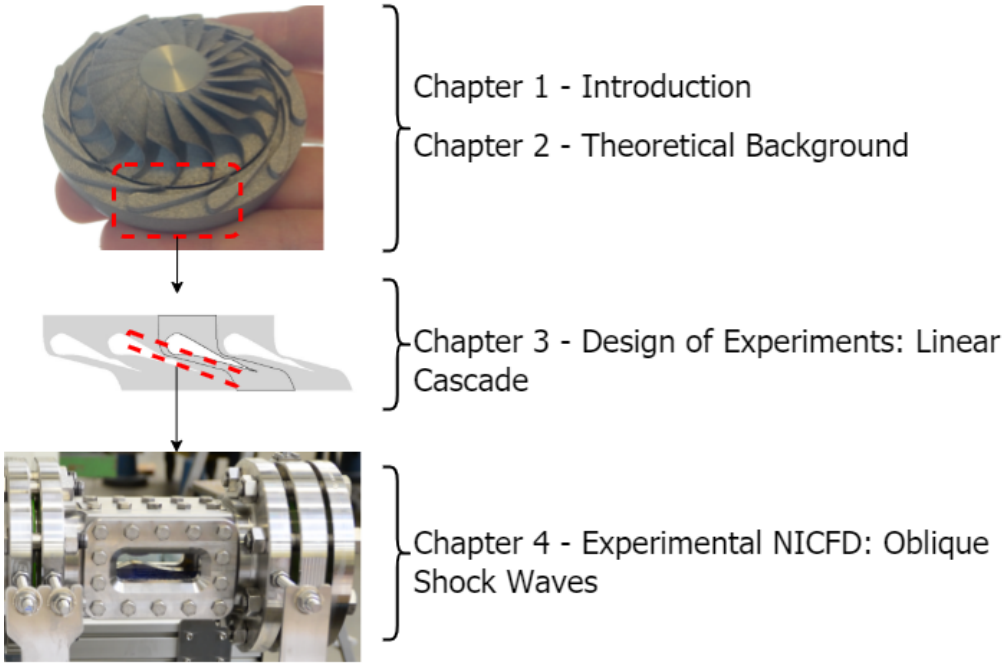

Figure 1.2: Hierarchical breakdown of a typical ORC expander. The chapters that deal with individual blocks of the flowchart are indicated.

2

Theoretical Background & State of the Art

2.1. Organic Rankine Cycles & Organic Fluids

Organic Rankine Cycles offer a viable solution to decentralised power generation for thermal energy sources that have low-to-medium peak temperatures (< 400°C) or a power capacity of few KW to tens of KW. The decentralised nature of ORC cycles also eliminates transmission requirements and associated losses. Thermodynamically, ORC systems are similar to conventional steam Rankine cycles and follow the loop of (i) compression, (ii) evaporation (Heat addition) at constant pressure, (iii) expansion and (iv) condensation (Heat removal) at constant pressure. Figure 2.1 depicts the layout of an exemplary ORC system and a related *T-s* diagram.

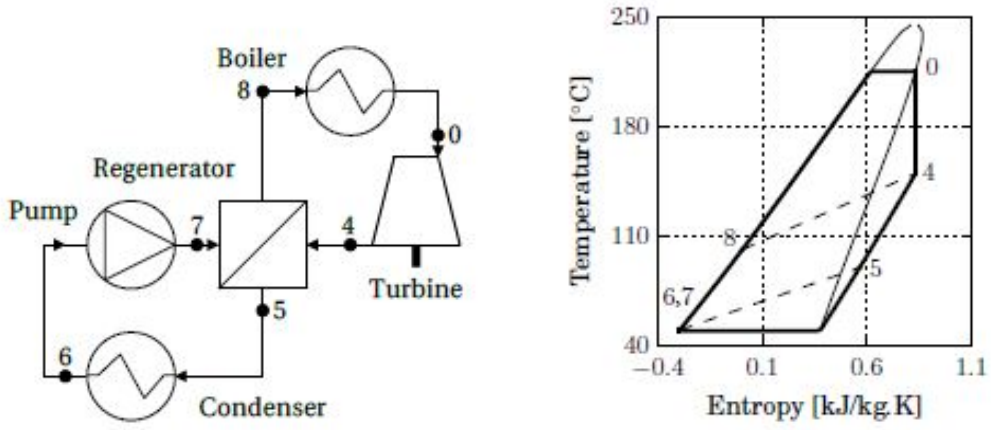

Figure 2.1: Exemplary ORC unit with regeneration. **(a)** Process flow diagram. **(b)** Temperature-entropy diagram of a thermodynamic cycle operating with hexamethyldisiloxane ($O[Si(CH_3)_3]_2$). Specifications: condensing temperature 50°C, evaporating pressure 12 bar, regenerator pinch temperature 40 K, no superheating, no pressure losses, isentropic compression/expansion. Taken from [8].

ORC systems use organic fluids(defined as molecule containing atleast one C-atom [88]) which have higher molecular weight and lower boiling point compared to water which allows for heat recovery from low-medium grade sources. The application of organic fluids to the Rankine cycle provides the following advantages to the system [25, 66]:

- The selection of working fluid provides an additional degree of freedom to maximise thermodynamic efficiency according to available source and sink temperature values.
- The operating pressure levels can be selected, to a certain extent, independent of the cycle temperatures allowing the realisation of novel cycle configurations like a supercritical cycle at low temperature.

- For applications where steam turbines are impractical, use of organic fluids allows for an expander design with lower rotational speed and higher volumetric flow for a given power output. This is due to the much smaller enthalpy decrease of the expanding vapour. Additionally, the organic fluids also serve as lubricants for the system.

- The expansion process in the ORC system is dry thereby avoiding issues related to blade erosion and expansion inefficiencies associated with condensation.

Therefore, the selection of an appropriate working fluid is an important design choice that has implications on the thermodynamic performance of the system and on the design of the components [25]. For instance, the large volume flow due to smaller enthalpy drop translates to a reduction in the number of turbine stages and lower rotational speed. Given the lower speed of sounds, the expanding flow easily reaches **supersonic** conditions requiring appropriate design of the flow passages. The larger volume flow rates also mean the system requires bulky regenerator and condenser. In the light of the current thesis, the organic fluid of interest is siloxane MM, an organo-silicon compound with the characteristic Si-O-Si bond. Table 2.1 provides a comparison of critical point properties (temperature, T_{cr} and pressure P_{cr}), the boiling temperature T_{boil} and the thermal stability limit T_{td}. Figure 2.1(b) is a representative T-s diagram for siloxane MM. The critical point is the top of the dome (within the dome the fluid is in the two-phase region) and is important for ORC systems since expansions occur close to the critical point. Within this region of operation, the fluid does not behave as an ideal fluid and displays strong non-ideal effects.

Table 2.1: Thermodynamic data- MM & Water

Fluid	CAS Nr.	T_{cr}/°C	P_{cr}/bar	T_{boil}/°C	T_{td}/°C
Water	7732-18-5	373.95	220.64	100	-
MM	107-46-0	245.6	19.4	100.2	350

In summary, due to their higher molecular mass, organic fluids have a low speed of sound resulting in supersonic flow through the internal passages of the expander. Additionally, the expansion occurs close to the saturation dome and critical point where strong non-ideal effects are present. Hence, the flow in the expander of an ORC system can be termed as non-ideal compressible flow. The following sections will equip the reader with the basics of supersonic compressible flow and non-ideal thermodynamics.

2.2. Characterisation of Non-Ideal Behaviour

A relation between the different state parameters of a system in thermodynamic equilibrium is called an equation of state. The ideal gas equation of state describes a hypothetical fluid that satisfies the following relation between the state parameters,

$$pv = RT \tag{2.1}$$

where p is the pressure, v is the specific volume, R is the specific gas constant and TT is the temperature of the system. Although the ideal gas approximation is a convenient simplification for modelling processes, it is a limiting case of a non-ideal gas when the pressure $p \rightarrow 0$ and inter-molecular forces are negligible. Non dimensional parameters discussed in the following sections provide information regarding the degree of non-ideal behaviour and assist the choice of appropriate modelling strategies.

2.2.1. Compressibility Factor

The compressibility factor Z is a dimensionless thermodynamic property that captures the deviation of a non-ideal gas from ideal gas assumptions.

$$Z = \frac{p\overline{v}}{\overline{R}T} \tag{2.2}$$

where p is the pressure, $\overline{v}$ is the molar specific volume, $\overline{R}$ is the universal gas constant and T is the temperature. For an ideal gas, it is assumed that there the volume occupied by the molecules and the strength of the intermolecular forces are negligible. This is true for high temperatures and low pressures and in this range $Z = 1$. But at higher pressures and lower temperatures, the volume occupied by the molecules and the

inter-molecular forces become significant and Z deviates from the ideal value of 1. Generalised compressibility charts plot Z as a function of the reduced parameters and according to the principle of corresponding states, the curves are $T_r(T_r = T/T_{cr})$ and p_r ($P_r = \frac{P}{P_{cr}}$). Z values provide a qualitative indication of degree of deviation from ideal gas assumption.

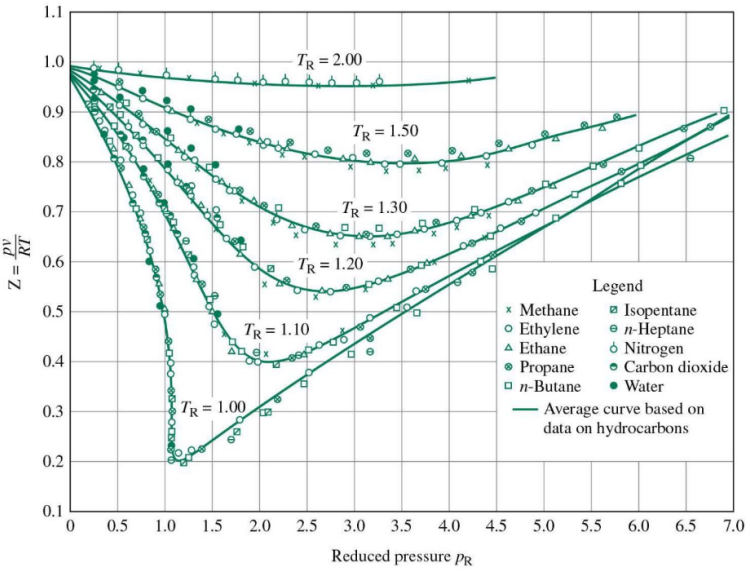

Figure 2.2: Generalised compressibility chart for various gases. Taken from [71].

2.2.2. Isentropic Relations

Based on the work by Kouremenos et al. [58], generalised isentropic relations have been derived where the ideal gas isentropic exponent, $\gamma = \frac{c_p}{c_v}$ is replaced by γ_{Pv}, γ_{Tv} and γ_{PT}. Relations 2.3 to 2.5 provide a summary of the final results. The derivation of these generalised expressions is beyond the scope of the thesis although the reader can refer to the work by Nederstigt [72] for more information.

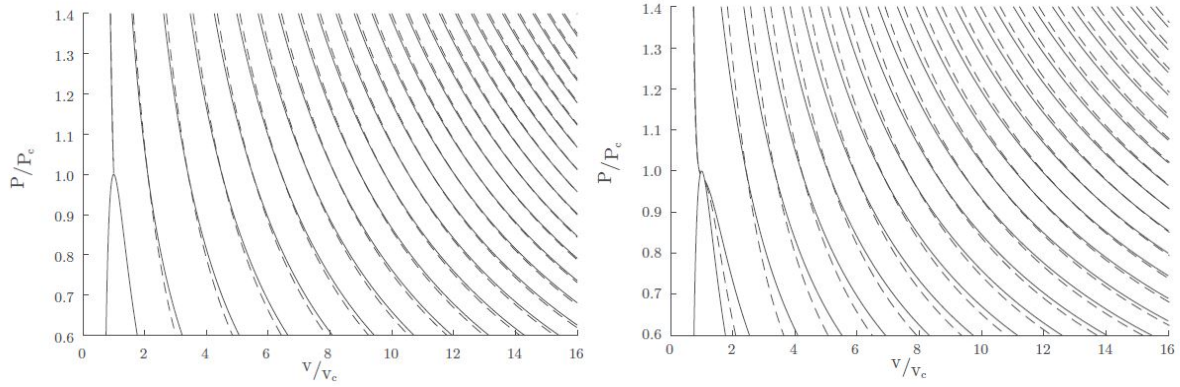

(a) Low molecular weight $c_v = 2.5R$

(b) High molecular weight $c_v = 50R$

Figure 2.3: Pressure-volume isentropes with variable (-) and constant (–) exponents for a molecular light and heavy Van der Waals substance. Taken from [72].

$$\gamma_{Pv} = -\frac{v}{P}\frac{c_p}{c_v}\left(\frac{\partial P}{\partial v}\right)_T \tag{2.3}$$

where γ_{Pv} is the pressure-volume exponent.

$$\gamma_{Tv} = 1 + \frac{v}{c_v}\left(\frac{\partial P}{\partial T}\right)_v \tag{2.4}$$

where γ_{Tv} is the temperature-volume exponent.

$$\gamma_{PT} = \frac{1}{1 - \frac{P}{c_p}\left(\frac{\partial v}{\partial T}\right)_P} \tag{2.5}$$

where γ_{PT} is the pressure-temperature exponent.
For the ideal case, all these exponents are equal to the ratio of specific heats. Nederstigt arrives at two important conclusions from isentropes plotted in Fig. 2.3 with constant and variable pressure-volume isentropic exponent. Firstly, that for higher temperatures, the isentropes with constant and variable γ_{Pv} increasingly coincide i.e., ideal gas assumption is valid in these regions. Secondly, the difference between the approximate and continuous isentropes increase with increasing molecular weight and complexity. Both these conclusions are relevant for the ORC cycle which uses working fluids with high molecular complexity close to the saturation dome.

2.2.3. Fundamental Derivative of Gas Dynamics

The deviant behaviour of fluids in the dense gas region can be explained by a non-ideal relation between the speed of sound and density along the isentrope. The complexity of the molecule and the thermodynamic region of the flow determine the value of speed of sound and its variation with density [23]. This behaviour is captured through derived thermodynamic parameter, Γ or the fundamental derivative of gas dynamics [98] given by Eqn. 2.6.

$$\Gamma = 1 + \frac{\rho}{c}\left(\frac{\partial c}{\partial \rho}\right)_s \tag{2.6}$$

Table 2.2 highlights three possible cases of fluid complexity influencing the behaviour of speed of sound during an isentropic expansion or compression process. The associated range of Γ is also indicated. For low molecular complexity (LMC) fluids, the speed of sound monotonically increase during compression and decreases during an expansion, independent of the thermodynamic region. Therefore, they can be treated as ideal gases. However for fluids of high molecular complexity (HMC), there exists a thermodynamic region close to the critical point where speed of sound increases during an expansion and decreases during compression. This regime of classical non-ideal gas dynamics is of relevance to the study of ORC expansion devices. The last case on non-classical gas dynamics captures behaviour of complex fluids called Bethe–Zel'dovich–Thompson (BZT) fluids that are theoretically predicted to show unique gas dynamic behaviour such as rarefaction shock waves.

Table 2.2: Regimes of gas dynamics and range of related fundamental derivative function [23].

Γ	**Regime of gas dynamics**	**Fluid type**
$\Gamma > 1$	Classical ideal gas dynamics	LMC-fluid
$0 < \Gamma < 1$	Classical non-ideal gas dynamics	HMC-fluid
$\Gamma < 0$	Non-classical gas dynamics	BZT- fluid

2.2.4. Expansions in the NICFD Regime

Figure 2.4 shows the *T-s* chart for the organic fluid, MM siloxane expansion in the vicinity of the vapour liquid critical point where strong NICFD effects are present. While Fig. 2.4a is plotted against the velocity of sound contour, Fig. 2.4b is plotted on $1 - Z$ and Γ contours. Consider the two expansion processes A and B - both from initial pressure of 100 bar to 5 bar and operating in the non-ideal thermodynamic state (Z < 1). Since both the processes operate in the region of $0 < \Gamma < 1$, they are classical non-ideal processes. As the fluid expands, the speed of sound decreases and then increases - a phenomena which is not expected in the ideal regime. Additionally, since process A is closer to the saturation dome it experiences stronger non-ideal effects compared to process B (Z value is significantly lower than 1 and Γ is close to 0).

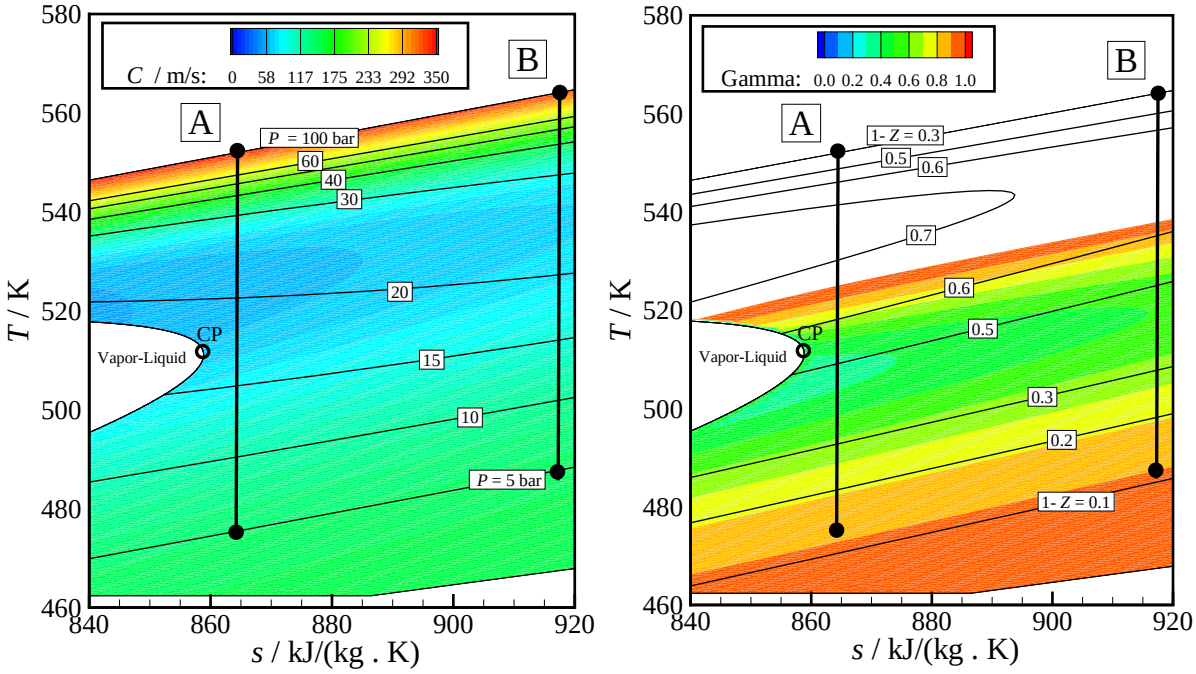

(a) (b)

Figure 2.4: *T-s* charts for isentropic expansion in the classical NICFD regime. Two representative isentropic expansions are plotted on **(a)** contours of speed of sound and pressure and **(b)** $1\text{-}Z$ and Γ Taken from [5].

2.3. Non-ideal Gas Thermodynamics

Given the shortcomings of the ideal gas law close to the critical point, alternate definitions of thermal and calorical properties are required to capture the non-ideal effects. In this section, the relevant equations of state (EoS), specific heat functions and departure functions will be discussed.

2.3.1. Equation of State (EoS)

Several alternate equations of state have been developed to describe the behaviour of thermally imperfect gases (i.e., a thermally perfect gas is one that satisfies the relation $p = \rho RT$). The van der Waals equation modifies the ideal gas equation of state by introducing two parameters a and b that account for molecular attraction and the co-volume factor (accounting for the volume occupied by molecules) respectively. The equation of state (EoS) is written as,

$$p = \frac{RT}{V-b} - \frac{a}{V^2}; \tag{2.7}$$

where a is,

$$a = \frac{27R^2T_c^2}{64p_c} \tag{2.8}$$

and b is,

$$b = \frac{RT_c}{8p_c} \tag{2.9}$$

While the model is theoretically sound, it fails to accurately predict flows close to the critical point. Hence, improvements have been made through alternate models such as Redlich-Kwong (RK) EoS, Soave-Redlich-Kwong (SRK) EoS, Peng-Robinson (PR) EoS , Stryjek-Vera-Peng-Robinson (Peng-Robinson EoS modified by Stryjek and Vera (PRSV)) EoS and the Improved Stryjek-Vera-Peng-Robinson (iPRSV) EoS. Given the specific interest of the thesis, the discussion is restricted to the PRSV and iPRSV models.
The Peng-Robinson EoS,

$$p = \frac{RT}{V-b} - \frac{a(T)}{V(V+b)+b(V-b)} \tag{2.10}$$

improves on the VdW EoS by introducing a dependency on the reduced temperature, T_r through the α function. Parameters a and b are defined as,

$$a = \left(\frac{0.457235 R^2 T_C^2}{P_c}\right)\alpha; \quad b = \frac{0.077796 R T_c}{P_c} \tag{2.11}$$

where α is,

$$\alpha = \left(1 + \kappa\left(1 - \sqrt{T_r}\right)\right)^2 \tag{2.12}$$

In Eqn.2.12, κ is a function of the acentric factor, ω that accounts for deviation of molecular shape from a spherical structure. The PRSV model modifies the κ term by making it dependent on both the acentric factor and reduced temperature. Under the PRSV definition, κ is defined as

$$\begin{aligned} \kappa &= \kappa_0 + \kappa_1\left(1 + \sqrt{T_r}\right)(0.7 - T_r) \\ \kappa_0 &= 0.378893 + 1.4897153\omega - 0.17131848\omega^2 + 0.0196554\omega^3 \end{aligned} \tag{2.13}$$

where ω is the acentric factor and T_r is the reduced temperature.
The PRSV model suffers from temperature continuity and a modification was introduced in the iPRSV EoS [100] to resolve the discontinuity by modifying the definition of κ as,

$$\kappa = \kappa_0 + \kappa_1\left[\sqrt{\left(A - D\left(\frac{T}{T_{cr}} + B\right)\right)^2 + E} + A - D\left(\frac{T}{T_{cr}} + B\right)\right]\sqrt{\frac{T}{T_{cr}} + C} \tag{2.14}$$

Table 2.3 provides the coefficients of the κ according to the iPRSV model.

Table 2.3: Coefficients of the κ function of the iPRSV EoS [100].

Coefficient	Value
A	1.1
B	0.25
C	0.2
D	1.2
E	0.01

The models discussed so far fall under the category of cubic EoS and have inherent disadvantages close to the critical point [22]. An alternate to the cubic EOS is an empirical approach where available data is fitted into a multi-parameter equation and provides results closer to experimental values. One such fit is the Span-Wagner functional form [94], derived from the Helmholtz free energy which can represent thermodynamic data within the experimental uncertainty of the measured properties.

2.3.2. Specific Heat Functions

From the generalised isentropic gas model, it is evident that there exists a multivariate dependency on mechanical and thermal properties. Similarly, specific heat relations for a calorically imperfect gases depend on state properties and the ideal gas relation $C_p - c_v = R$ is a special case of a generalised expression. Equation 2.15 describe the generalised isobaric and isochoric specific heat functions and Z is the compressibility factor.

$$c_p = \frac{\gamma_{PT}}{\gamma_{PT} - 1} R\left[Z + T\left(\frac{\partial Z}{\partial T}\right)_P\right]; \quad c_v = \frac{R}{\gamma_{Tv} - 1}\left[Z + T\left(\frac{\partial Z}{\partial T}\right)_v\right] \tag{2.15}$$

The pressure-volume isentropic exponent can be rewritten in terms of the generic heat capacities as,

$$\gamma_{Pv} = \frac{c_p}{c_v}\left[\frac{Z + T\left(\frac{\partial Z}{\partial T}\right)_v}{Z + T\left(\frac{\partial Z}{\partial T}\right)_P}\right] \tag{2.16}$$

A commonly used relation when the constant heat capacity assumption is not valid, is based on the joint army navy NASA and air force (JANNAF) database,

$$c_p = \eta_1 + \eta_2 T + \eta_3 T^2 + \eta_4 T^3 + \eta_5 T^4. \tag{2.17}$$

where T is the temperature and the various coefficients, η are determined experimentally for each gas. For the scope of this thesis, the implementation is a polytropic model, meaning that the ratio of specific heat capacities remains constant. It must be noted that this is a shortcoming of the available modelling tool and in reality a non-polytropic implementation would be required for non-ideal flows.

2.3.3. Departure Functions

The departure functions for extensive thermodynamic properties like internal energy U, enthalpy H, entropy S, Gibbs energy G and specific heat at constant pressure C_p and volume C_v provide information on the deviation between real and ideal property values. The variables with superscript d in Eqn.2.18 quantifies this deviation and at zero pressure conditions would be zero.

$$H_d = H - H_{ig}, \quad S_d = S - S_{ig} \quad \text{and} \quad C_{P,d} = C_P - C_{P,ig} \tag{2.18}$$

Equations 2.19 to 2.21 provide the analytical description of the departure functions [79],

$$\frac{H_{ig} - H}{RT} = \int_V^\infty \left[T\left(\frac{\partial Z}{\partial T}\right)_V \right] \frac{dV}{V} + 1 - Z \tag{2.19}$$

$$\frac{S_{ig} - S}{RT} = \int_V^\infty \left[T\left(\frac{\partial Z}{\partial T}\right)_V - 1 + Z \right] \frac{dV}{V} - \ln Z \tag{2.20}$$

$$\frac{C_P}{R} = \frac{C_{P,ig}}{R} - 1 - T\int_V^\infty \left[T\left(\frac{\partial^2 P}{\partial T^2}\right)_V \right]_T dV - T\left(\frac{\partial P}{\partial T}\right)_V^2 \Big/ \left(\frac{\partial P}{\partial V}\right)_T \tag{2.21}$$

2.3.4. Transport Models

The final set of equations describe how heat and momentum and transported in the flow. As seen in Eqn. 2.22 and 2.23, transport of both heat and momentum are proportional to the gradient of temperature and velocity respectively,

$$q_x = -k\frac{\partial T}{\partial x}, \tag{2.22}$$

$$\tau_x = \mu^\nu \frac{\partial u}{\partial y}, \tag{2.23}$$

where q and τ are the heat flux density and shear stress in the x-direction. The proportionality constants are thermal conductivity, k and fluid viscosity, μ^ν.
Usually μ^ν can be either a constant or given by the Sutherland's law which introduces a dependency on temperature. Although the Sutherlands model is applicable only to cases that satisfy the ideal gas criteria, it usually suffices for most practical applications. But, for turbomachinery operating in the non-ideal regime more sophisticated models that take into account non-ideal effects exist. Two models available in NICFD literature and implemented in modelling tools will be discussed, namely: (i) the Extended Corresponding States model (implemented in RefProp [64]) and (ii) the Chung's transport model (implemented in StanMix [7]).
Viscosity of fluids can be expressed as the sum of dilute gas viscosity, μ^* (which is a function of T only) and a residual viscosity term, $\Delta\mu$ (which is a function of T & P or ρ).

$$\mu(T,\rho) = \mu^*(T) + \Delta\mu(T,\rho), \tag{2.24}$$

$$\Delta\mu(T,\rho) = \Delta\mu_0\left(T_0,\rho_0\right) F_\mu(T,\rho). \tag{2.25}$$

The Extended Corresponding States (Extended Corresponding States (ECS)) model is applied to the residual viscosity term. Developed by Huber *et al.* [52] for dense gases and refrigerants, it is often used to predict thermophysical properties of fluids with limited experimental data [54]. The model stems from the concept of corresponding states which states that "substances with the same reduced states behave similarly". Reduced states are described by the ratio of properties with their respective critical values. The ECS model applies the principle of corresponding states to the fluid of interest and a reference fluid. The viscosity of the reference fluid is calculated at thermodynamic point (T_0,ρ_0) which conform to the thermodynamic point of the fluid of interest by following Equations,

$$T_0 = T/f, \tag{2.26}$$

$$\rho_0 = \rho h \tag{2.27}$$

where f and h are called equivalent substance reducing ratios and are defined as,

$$\begin{aligned} f &= \frac{T_c}{T_{c0}}\theta(T,\rho), \\ h &= \frac{\rho_{c0}}{\rho_c}\phi(T,\rho) \end{aligned} \tag{2.28}$$

θ and ϕ are shape factors that depend on temperature and density. The exact shape factor method proposed by Huber *et al.* requires the choice of an appropriate reference fluid that resembles the fluid of interest chemically and structurally. Once the fluid is identified, the thermodynamic surfaces of one fluid is mapped onto another to directly find the conformed thermodynamic points.

An alternate transport model is that predicted by Chung's approach which empirically correlates viscosity and thermal conductivity as functions of density and temperature [17]. The dilute gas viscosity is extended to fluids at high densities by introducing empirically correlated density functions that use : (i) Pitzer's acentric factor, ω; (ii) dimensionless dipole moment, η_t and (iii) an empirically determined association parameter, κ. Thus, the model only needs critical temperature, volume and acentric factor as inputs for predictions of non-polar fluids. The viscosity is then given by,

$$\mu = \mu_\kappa + \mu_p \tag{2.29}$$

where μ_κ is dependent on the dilute gas viscosity prediction and μ_p is the empirically correlated function dependent on temperature and density along with the previously mentioned variables. At the limiting value of low density, μ_p is negligible and the prediction becomes consistent with the dilute gas viscosity case. It was observed that the viscosity increases significantly with density as the fluid becomes dense which indicates that for prediction of dense gas fluid viscosity, density is a very sensitive parameter. The Chung's predictive method has been extensively used in literature and found to be satisfactory in predicting transport properties for polar, non-polar and associating pure fluids for wide range of conditions. For the operating condition of interest to the thesis, Table 2.4 summarises the computed transport property values from both approaches. At the inlet the transport properties show a deviation of around 31% and 7.6% for viscosity and thermal conductivity respectively. At the outlet, this difference reduces to 10.7% for viscosity and increases for thermal conductivity to 13.3%.

Table 2.4: Transport properties computed with ECS (from RefProp) and Chung's model (from StanMix) for inlet and outlet conditions at the ORCHID, TU Delft.

	RefProp		**StanMix**	
	μ **(Pa-s)**	k **(W/m-K)**	μ **(Pa-s)**	k **(W/m-K)**
Inlet (P_o= 18.4 bar; T= 525K)	1.17e-05	0.0395	1.7e-05	0.0367
Outlet (P_o= 1.95 bar; T= 483.2K)	1.05e-05	0.0278	9.51e-06	0.0245

2.4. Compressible Fluid Dynamics- A Theoretical Background

2.4.1. Fundamentals of Compressible Flow

As indicated previously, the expansion of flows in ORC systems display non-ideal thermodynamic (covered in Sec. 2.2 and 2.3) and supersonic fluid behaviour. Hence, it is relevant to understand compressible flow phenomena and how they differ for non-ideal flows. As the flow velocity approaches local speed of sound, density changes become appreciable and cannot be neglected. For a change of pressure dp, the corrsponding change in density dρ is related to the compressibility τ of the fluid by,

$$d\rho = \rho\tau dp \tag{2.30}$$

As a rule of thumb, if the density of the fluid varies by more than 5% , the fluid is considered compressible [6]. The speed of sound in the medium is an important parameter for the distinction of compressible and incompressible flow because sound travels through compression waves in a medium and is dependent on the compressibility of the medium. The speed of sound is given by,

$$a = \sqrt{\gamma_{Pv} ZRT} \tag{2.31}$$

where γ_{Pv} is the pressure-volume isentropic exponent, Z is the compressibility factor, R is the gas constant and T is the local flow temperature. Hence, the Mach number M, which is the ratio of flow speed to local speed of sound is widely used to describe compressible flows.

The compressible flow through a control volume $\mathcal{V}$ and control surface area S can be modelled by the conventional conservation laws:

- **Continuity equation:**

$$-\underset{\text{(I)}}{\oiint_S \rho \mathbf{V} \cdot d\mathbf{S}} = \frac{\partial}{\partial t} \underset{\text{(II)}}{\iiint_{\mathcal{V}} \rho d\mathcal{V}} \tag{2.32}$$

  where (I) is the net mass flow into the control volume through entire surface area S and (II) is the time rate of the change of the mass inside the control volume.

- **Momentum equation:**

$$\underset{\text{(I)}}{\oiint_S (\rho \mathbf{V} \cdot d\mathbf{S})\mathbf{V}} + \underset{\text{(II)}}{\iiint_{\mathcal{V}} \frac{\partial(\rho \mathbf{V})}{\partial t} d\mathcal{V}} = \underset{\text{(III)}}{\iiint_{\mathcal{V}} \rho \mathbf{f} d\mathcal{V}} - \underset{\text{(IV)}}{\oiint_S p d\mathbf{S}} \tag{2.33}$$

  where (I) is the net rate of flow of momentum over the control surface area, (II) is the change in momentum within the control volume due to unsteady flow, (III) represents the net body force over the control volume and (IV) represents the net surface force over the control surface.

- **Energy equation:**

$$\begin{aligned} &\underset{\text{(I)}}{\dot{Q}} + \underset{\text{(II)}}{\dot{W}_{\text{shaft}}} + \underset{\text{(III)}}{\dot{W}_{\text{viscous}}} - \underset{\text{(IV)}}{\oiint_S p \mathbf{V} \cdot d\mathbf{S}} + \underset{\text{(V)}}{\iiint_{\mathcal{V}} \rho(\mathbf{f} \cdot (\mathbf{V}))d\mathcal{V}} \\ &= \underset{\text{(VI)}}{\iiint_{\mathcal{V}} \frac{\partial}{\partial t} \left[\rho \left(e + \frac{V^2}{2} \right) \right] d\mathcal{V}} + \underset{\text{(VII)}}{\oiint_S \rho \left(e + \frac{V^2}{2} \right) \mathbf{V} \cdot d\mathbf{S}} \end{aligned} \tag{2.34}$$

  where (I) is the heat added across the control surface, (II) is the work done on the fluid inside the control volume, (III) is the work done by the viscous stresses on the control surface, (IV) and (V) is the net work done on the fluid inside the control volume by surface and body forces, (VI) is the time rate of change of energy inside the control volume and (VII) is the net flow of energy across the control surface.

The above equations in conjunction with an appropriate EoS, transport relations and a turbulence model provide closure for modelling compressible flows. An ORC turbine stator is essentially a converging-diverging nozzle (variable area ducts). Variation of flow parameters in compressible flow lead to flow features such as mach waves, shock waves and expansion fans. These flow features can be seen as inefficient compression (or expansion) processes accompanied with entropy generation. Shocks in turbomachinery lead to significant losses, lower performance and compromise on structural integrity. Hence, to make a stronger case for the competitiveness of ORC systems, it is important to design the internal channels of the turbomachinery to reduce shock phenomena and related losses.

2.4.2. Shock Waves & Expansion Waves

Shock waves perpendicular to the free stream direction are normal shocks whereas shocks inclined at an angle with the free stream direction are oblique shocks. The conditions across the discontinuity are governed by the integral conservation equations (2.35) for mass, momentum and energy (subscripts 1 & 2 indicate before and after the normal shock respectively).

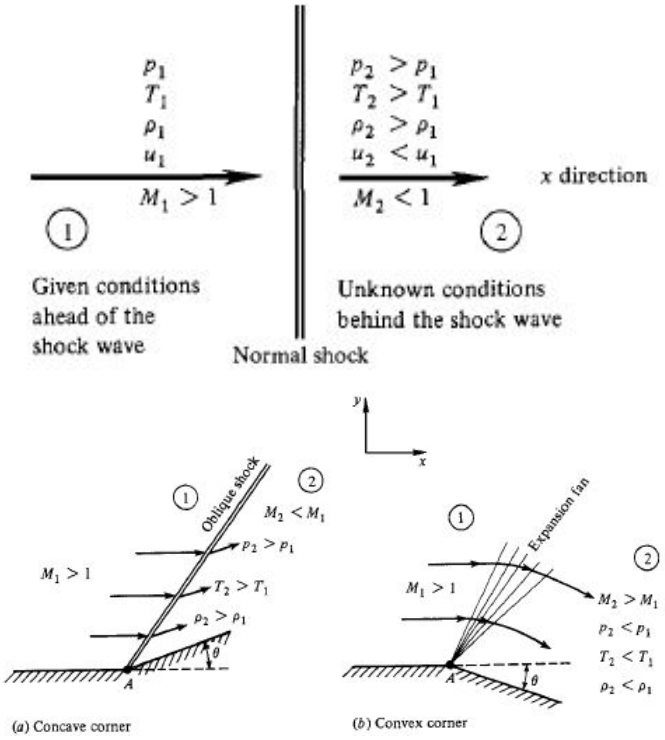

Figure 2.5: Shock waves in compressible flow : **(a)** Normal shock, **(b)** Oblique shock and expansion waves. Taken from [6, p. 130].

$$\begin{aligned} \rho_1 u_1 &= \rho_2 u_2 \\ p_1 + \rho_1 u_1^2 &= p_2 + \rho_2 u_2^2 \\ h_1 + \frac{u_1^2}{2} &= h_2 + \frac{u_2^2}{2} \end{aligned} \tag{2.35}$$

For the case of perfect gases, the following thermodynamic relations can be used for closure.

$$\begin{aligned} p &= \rho R T \\ h &= c_p T \end{aligned} \tag{2.36}$$

where h is the enthalpy and C_p is the specific heat capacity at constant pressure. Solving the above set of equations yields important relations of interest for normal shocks which are as follows: The Mach number M_2 after the shock is,

$$M_2^2 = \frac{1 + [(\gamma-1)/2] M_1^2}{\gamma M_1^2 - (\gamma-1)/2} \tag{2.37}$$

The density, pressure and temperature ratio across the shock are given by,

$$\frac{\rho_2}{\rho_1} = \frac{u_1}{u_2} = \frac{(\gamma+1) M_1^2}{2 + (\gamma-1) M_1^2} \tag{2.38}$$

$$\frac{p_2}{p_1} = 1 + \frac{2\gamma}{\gamma+1}\left(M_1^2 - 1\right) \tag{2.39}$$

$$\frac{T_2}{T_1} = \frac{h_2}{h_1} = \left[1 + \frac{2\gamma}{\gamma+1}\left(M_1^2 - 1\right)\right] \frac{2 + (\gamma-1) M_1^2}{(\gamma+1) M_1^2} \tag{2.40}$$

It should be noted that the relations solely depend on M_1 for the case of calorically perfect gas (constant γ). For thermally perfect gases the changes depend on M_1 and T_1. Of special interest for the thesis, are oblique shock waves. An important distinction is made between Mach waves and oblique shock waves. Mach waves

are a limiting case for oblique shocks, i.e. it is an infinitely weak oblique shock. While the mach angle μ is calculated as $\mu = \sin^{-1}\frac{1}{M}$, the oblique angle β can be derived from resolving the conservation equations for the flow geometry shown in Fig. 2.6.

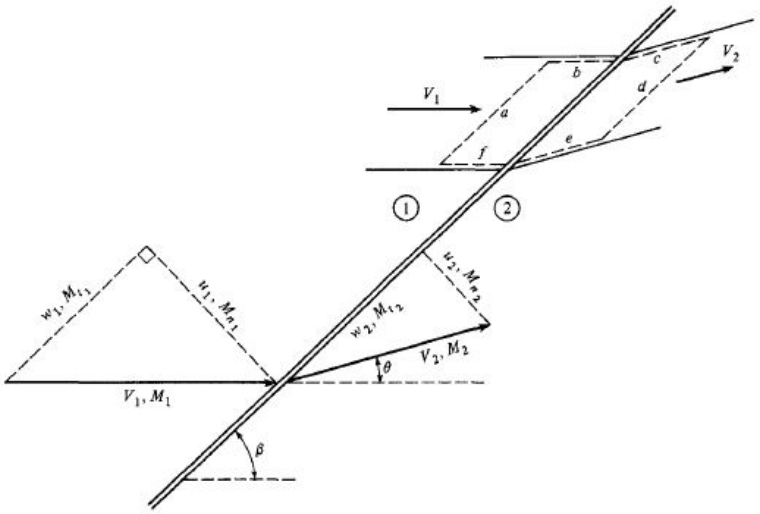

Figure 2.6: Oblique shock wave geometry. Taken from [6, p. 134].

The normal component of the upstream Mach number is M_{n1} is,

$$M_{n_1} = M_1 \sin\beta \tag{2.41}$$

The normal component of the downstream Mach number, M_{n_2} can be computed from,

$$M_{n_2}^2 = \frac{M_{n_1}^2 + [2/(\gamma-1)]}{[2\gamma/(\gamma-1)]M_{n_1}^2 - 1} \tag{2.42}$$

Consequently, the density, pressure and temperature ratios across the oblique shock are given by,

$$\frac{\rho_2}{\rho_1} = \frac{(\gamma+1)M_{n_1}^2}{(\gamma-1)M_{m_1}^2 + 2} \tag{2.43}$$

$$\frac{p_2}{p_1} = 1 + \frac{2\gamma}{\gamma+1}\left(M_{n_1}^2 - 1\right) \tag{2.44}$$

$$\frac{T_2}{T_1} = \frac{p_2}{p_1}\frac{\rho_1}{\rho_2} \tag{2.45}$$

The total Mach number at station 2 after the shock wave can be computed from,

$$M_2 = \frac{M_{n_2}}{\sin(\beta-\theta)} \tag{2.46}$$

where θ , the deflection angle made by the obstacle with respect to the flow, is given by the $\theta-\beta-M$ relation,

$$\tan\theta = 2\cot\beta\left[\frac{M_1^2\sin^2\beta - 1}{M_1^2(\gamma+\cos 2\beta)+2}\right] \tag{2.47}$$

Figure 2.7 is a representation of the $\theta-\beta-M$ relation and is a vital component of analysing oblique shock waves. The shape of the curve represnets the non-linear relations in oblique shock analysis. Some salient conclusions from the plot are: (i) there exists a θ_{max} for a given Mach number. For θ greater than that value, the shock will be curved and detached, (ii) For any θ below θ_{max}, there are two values of β possible (shown by the blue and yellow lines in Fig. 2.7). The occurrence of weak or strong shocks is determined by the backpressure although weak shocks are more common. (iii) For $\theta = 0$, there are two possibilities - normal

shocks ($\beta = 90$) or Mach waves ($\beta = 0$), (iv) In the weak shock regime, for a fixed θ the shock angle increases as the Mach number decreases.

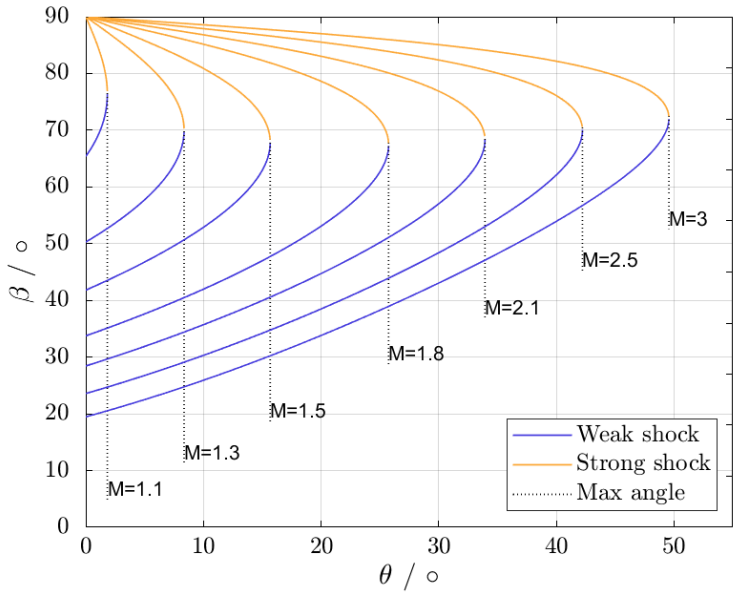

Figure 2.7: $\theta - \beta - M$ plot for Siloxane MM. Taken from [13].

While the closed form $\theta - \beta - M$ relation holds true for perfect gases, it is not possible to derive a similar closed form expression for the non-ideal case since the fluid properties across the shock are not constant. Thus an iterative process must be used based on Eqn. 2.48. Given the flow conditions p_1, ρ_1, and V_1 Grossman [44] proposes the following:

$$\tan\beta = \frac{\left(1-\frac{\rho_1}{\rho_2}\right) \pm \left[\left(1-\frac{\rho_1}{\rho_2}\right)^2 - 4\frac{\rho_1}{\rho_2}\tan^2\theta\right]^{1/2}}{2\frac{\rho_1}{\rho_2}\tan\theta} \tag{2.48}$$

1. From the initial known conditions, the initial enthalpy h_1 can be found, i.e. $h_1 = h(p_1, \rho_1)$.
2. An initial density ratio $\upsilon = \frac{\rho_1}{\rho_2}$ is guessed. Then $\rho_2 = \frac{\rho_1}{\upsilon}$.
3. If the shock is oblique Eqn. 2.48 is evaluated from the guessed density ratio. Then $V_{n1} = V_1 \sin\beta$.
4. Using the equations defined in the oblique shock chapter, it is possible to find $V_{n_2} = V_{n_1}\upsilon, p_2 = p_1 + \rho_1 V_{n1}^2(1-\upsilon)$ and $h_2 = h_1 + \left(V_{n1}^2/2\right)\left(1-\upsilon^2\right)$.
5. Using the equation of state, enthalpy downstream can be found from $\tilde{h}_2 = h\left(p_2, \rho_2\right)$.
6. If $h_2 = \tilde{h}_2$ state two is solved. If not, the process starts again from step two with a new guess of density ratio.

The previous sections discuss the compressible flow dynamics in the 1D case (normal shocks) and 2D flow around concave corners (oblique shocks). When a supersonic flow is turned away from itself (convex corner), expansion waves are formed. Unlike in oblique waves, the Mach number after the shock increases while pressure, density, temperature decrease. In addition, the expansion is isentropic because the expansion takes place through a continuous succession of Mach waves ($\mu_1 = \arcsin 1/M_1$ and $\mu_2 = \arcsin 1/M_2$) and ds=0 for Mach waves. The kind of expansion fan in Fig. 2.8 is called a centered expansion fan or a Prandtl-Meyer expansion wave. The expansion is characterised by the Prandtl-Meyer function, ν which is derived for a small increment $d\theta$ from the mass, momentum and energy conservation relations. Eqn. 2.49 is applicable only for perfect gases.

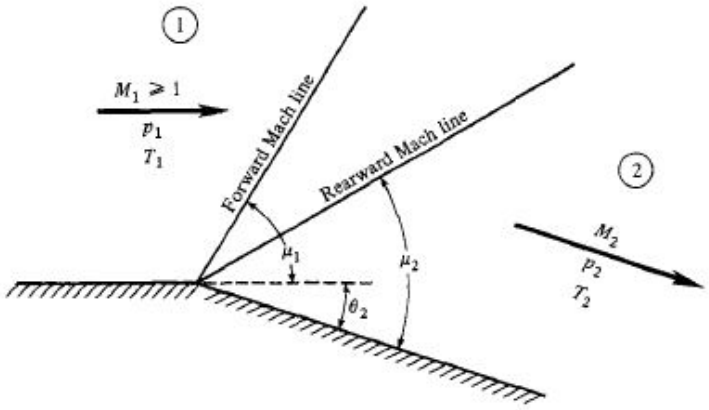

Figure 2.8: Prandtl-Meyer expansion. Taken from [6, p. 168].

$$\upsilon(M) = \sqrt{\frac{\gamma+1}{\gamma-1}}\tan^{-1}\sqrt{\frac{\gamma-1}{\gamma+1}\left(M^2-1\right)} - \tan^{-1}\sqrt{M^2-1} \tag{2.49}$$

For alternate cases, such as dense gas expansion [28] discusses the analytical solution for calculating ν. Nederstigt [72] has derived the closed form expression for the real gas Prandtl Meyer function in terms of the real isentropic exponent , $\gamma_{P\nu}$,

$$\nu = -\sqrt{\frac{\gamma p_\upsilon+1}{\gamma p_\upsilon-1}}\tan^{-1}\sqrt{\frac{\gamma_{p\upsilon}-1}{\gamma_{p\upsilon}+1}\left(M^2-1\right)} + \tan^{-1}\sqrt{M^2-1}. \tag{2.50}$$

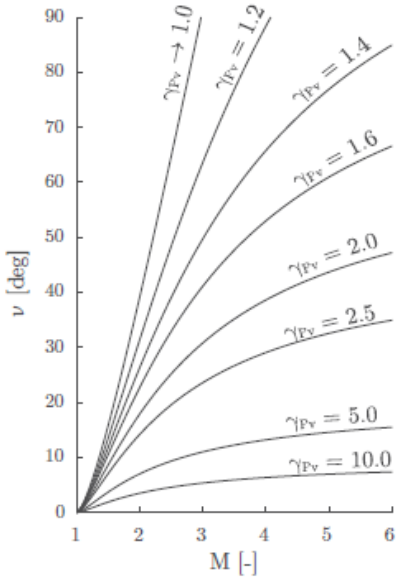

Figure 2.9: Prandtl- Meyer angle as a function of the Mach number for different values of the isentropic exponent $\gamma_{P\nu}$. Taken from [72].

Figure 2.9 plots the Prandtl-Meyer function against the Mach number for different values of the isentropic exponent. For non-ideal gases, the isentropic exponent is above the ideal theoretical limit of 1.6. As it increases, the compressibility of the medium decreases and it can be seen from the graph that the Prandtl-Meyer expansion function decreases i.e. smaller deflection angles will be observed.

2.5. Validation of CFD Solvers through Uncertainty Quantification

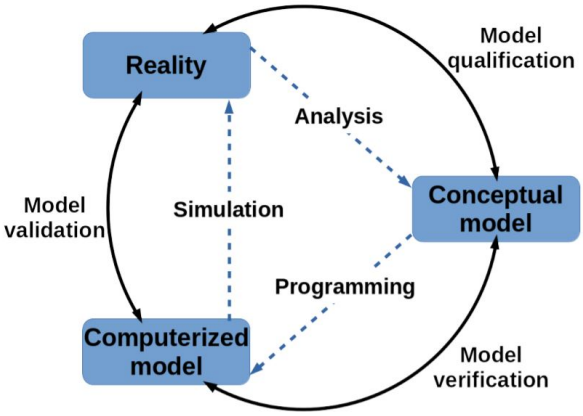

Figure 2.10: Phases of modelling and simulation. Taken from [89].

Computational fluid dynamics (CFD) tools are extensively used in the fluid dynamic design of machinery due to their relative ease of use and robustness compared to experiments. CFD simulations form the computerised model block in Fig. 2.10. However, the credibility of such tools must be validated with experimental data which is often difficult to obtain for nascent technology such as ORC systems. Thus, there is a need to fill the knowledge gap regarding the reliability of modelling tools. Once experimental results are available, there is also a requirement for the definition and application of an appropriate validation methodology. Industry standard Verification and Validation (V&V) methodologies such as the American Society of Mechanical Engineers (ASME) guidelines [2] have been widely implemented in various scenarios. According to the standards, a model is 'validated' if it represents the physical phenomena in question within some pre-defined statistical degree of confidence. Both experiments and simulation models suffer from uncertainties. Once these uncertainties are quantified, the predictive capabilities of the model can be assessed through appropriate statistical tests or metrics.
A well tested and accepted validation metric is that defined by ASME V&V 20 framework and is the approach implemented in this thesis. It is a a binary approach that involves running a simulation in the flow solver of interest and an identical case in a controlled experiment while recording all parameters of interest. Consider the situation in Fig. 2.11 where T is the unknown true value, D is the experimental value and S is the simulation result. The comparison error E is the difference between the simulation result, S and the experiment results, D and can be computed from data available.

$$E = S - D, \tag{2.51}$$

Let δ_S and δ_D represent the simulation and experimental errors respectively. They can be calculated as,

$$\delta_S = S - T, \tag{2.52}$$

$$\delta_D = D - T, \tag{2.53}$$

Combining the two, the comparison error, E can be expressed as,

$$E = S - D = (T + \delta_S) - (T + \delta_D) = \delta_S - \delta_D \tag{2.54}$$

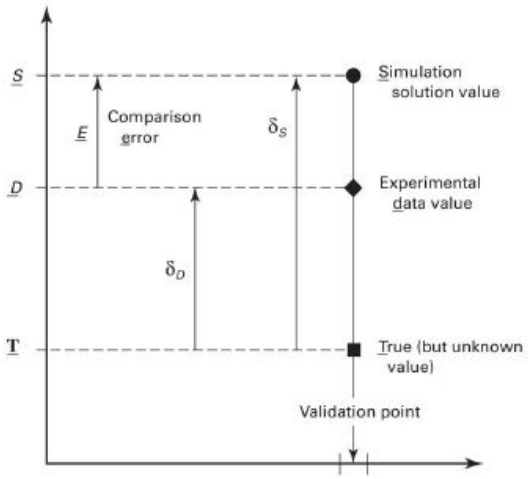

Figure 2.11: Relation between the true, but unknown, value with the simulation and experimental ones for a given validation point. Taken from [2].

Prior to discussing the quantification of errors, it is important to dilineate the difference between an error and uncertainty. Errors refer to the difference between the measurement or prediction and the true value of the measurand [20]. Although complementary to the concept of error, uncertainty is an interval within which measured/predicted values are likely to lie. The experimental error δ_D can be broken into Type A and Type B uncertainties. Type A includes all the uncertainties in an experiment that can be quantified from a statistical analysis of the data such as the mean and standard deviation. Type B uncertainties cover the remaining sources of experimental uncertainty that cannot be statistically captured, for example human error. Quantifying experimental uncertainties require rigorous bookkeeping and thorough statistical analysis which are reported in the following references [3, 14, 21, 53]. The simulation error, δ_S consists of the following three components:

- δ_{model} due to modelling assumptions and approximations;
- δ_{num} due to numerical methods implemented to solve the equations. It includes three different components: round-off error, iterative error and the discretisation error. Round-off and iterative errors can be cosnidered negligible if startegies such as double precision and appropriate residual convergence is achieved. Discretisation errors can be reduced with increased grid-refinement and methods such as Richardson extrapolation as described by Eca *et al.*[34] can be used to quantify the same.
- δ_{in} due to uncertainties associated with the input parameters. Section 2.6 provides a detailed description of methods employed to compute the input uncertainty.

The objective of the analysis is to capture the modelling error δ_{model} since our interest lies in knowing whether the numerical model accurately capture real physics. The modelling error can be written in terms of known parameters as,

$$\delta_{\text{model}} = E - \left(\delta_{\text{num}} + \delta_{\text{input}} - \delta_D\right), \tag{2.55}$$

The standard uncertainties associated with each of these errors are u_{num}, u_{input} and u_{D} , which correspond to an estimate of the standard deviation of the parent distribution. Given the three errors are independent of each other, a combined validating standard uncertainty, u_{val} can be defined,

$$u_{\text{val}} = \sqrt{u_{\text{num}}^2 + u_{\text{input}}^2 + u_{\text{D}}^2} \tag{2.56}$$

Once u_{val} is known, the goal is to identify the interval $[E - u_{\text{val}}, E + u_{\text{val}}]$ which contains the modelling error. The model needs to be improved if $|E| \gg u_{\text{val}}$. However,if $|E| \leqslant u_{\text{val}}$ then the model is capable of predicting the physics of the problem under investigation with sufficient accuracy.

2.6. Forward Propagation of Input Uncertainty

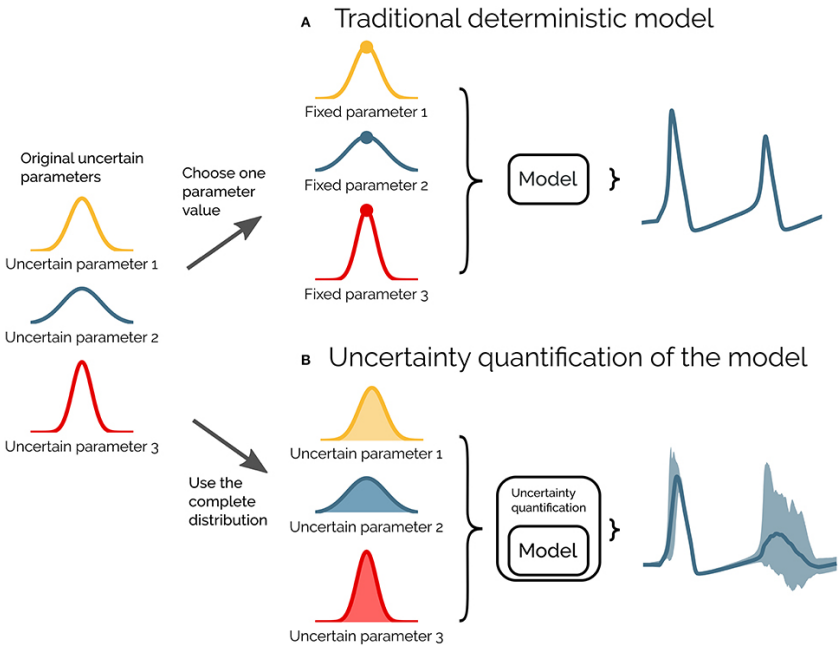

Figure 2.12: Illustration of forward uncertainty propagation through a comparison with a deterministic simulation. Taken from [97].

In complex simulation cases such as those of turbomachinery, a large number of inputs and their associated uncertainties contribute to the total uncertainty. In such scenarios, the associated input uncertainties cannot be simply added. They are instead estimated by a rigorous uncertainty quantification (uncertainty quantification (UQ)) procedure that involves: (i) characterising the input uncertainties, (ii) propagating the uncertainties through the computational model and (iii) performing a statistical analysis on the results obtained [4]. The input uncertainties can either be aleatory or epistemic. Aleatory uncertainties are random, irreducible variabilities present in nature by default.As adequate information is available, the distribution of these uncertainties are known and hence common probabilistic methods can be used to determine their effect on the response functions. On the other hand, epistemic uncertainties are reducible uncertainties resulting from a lack of knowledge. They are generally characterized in terms of an interval i.e. by specifying the upper and the lower bounds of the variation [56]. As the available data is limited, sampling based methods are used to ascertain their effect on the response functions. Once the nature of the input uncertainty is ascertained, the uncertainties can be propagated through sampling techniques like Monte-Carlo sampling, Latin Hypercube sampling, stochastic collocation methods, importance sampling, adaptive sampling etc [18, 19, 27, 43]. A choice can be made depending on the fidelity of the computational model. For instance, the Monte Carlo technique samples realisations of the inputs using a random number generator. Subsequently for each sample, the computational model is run and a statistical analysis of the responses is generated. To accurately capture statistical quantities such as mean and standard deviation, the Monte Carlo method requires an estimated 1000 runs. For complex cases, this is not affordable in terms of computation time. As an alternative, surrogate modelling (or metamodelling) offsets the increased costs of modelling by employing inexpensive to evaluate surrogate models. For example, Polynomial chaos expansion (PCE) is a powerful metamodelling technique that aims at providing a functional approximation of a computational model through its spectral representation on a suitably built basis of polynomial functions.

2.7. Summary

Chapter 2 intended to provide the reader with sufficient background knowledge on non-ideal compressible flows. This is relevant to the design of the stator for radial inflow turbines for ORC systems which operate at regions close to the critical point where the ideal gas law is not valid anymore. Additionally, the properties of the working fluid specifically the lower speed of sound makes the flow in the stator supersonic and leads to loss generating shocks. Design of stators operating in this regime require experimentally validated auto-

mated design tools. Quantifying the effect of model input uncertainties is an integral step in the validation procedure. Standardised methods for validation and forward input uncertainty propagation were discussed.

3

Design of Experiments - Linear Cascade

The flow through the stator row of a radial ORC turbine can be understood by simplified flow field cases such as a linear blade cascade and a converging-diverging (CD) nozzle. Consequently, this chapter deals with the study of dense gas supersonic expansions through a proposed 5 channel linear stator cascade that will be realised at the ORCHID. The chapter begins with a discussion on the validation hierarchy developed for the prediction of flow physics in a blade row (Sec. 3.1) followed by a summary of the mechanical design of the linear cascade test section (Sec. 3.2). The flow physics of the 5 channel blade row is studied through a 2D single channel blade under the verified assumption of periodicity and 2D flow field simplification. Design of Experiments (DOE) is a statistical method to examine the behaviour of a simulation model and quantify how changes in parameter values and their interaction affects the output [106]. Van Schepdael *et al.* [102] outlines a three step process for a sensitivity analysis using Design of Experiments (DOE). The first step is to construct a design of a number of parameter combinations for which the model will be run. Following this, simulations are run with the identified parameter combinations and a statistical analysis of the results is carried out to draw conclusions. The details of the DOE approach are presented in Sec. 3.3.

Within the turbomachinery community, there is a growing interest to couple numerical simulations with optimisation procedures. The design chain used in turbomachinery optimisation problems is schematically represented in Fig. 3.1. The common optimisation approaches can be classified into gradient-based and gradient-free or stochastic methods. For the gradient-based methods, information on how the objective function changes with respect to the design variables is used to identify the minimum. On the other hand, gradient free (or stochastic) methods search for a global minimum and hence require a large number of flow evaluations making it computationally expensive for complex turbomachinery cases. The adjoint based shape optimisation falls under the former category. The chapter reports (Sec. 3.4) a critical assessment of the adjoint shape optimisation capabilities within the open source flow solver, SU2 through a DOE based sensitivity analysis on the optimised geometry.

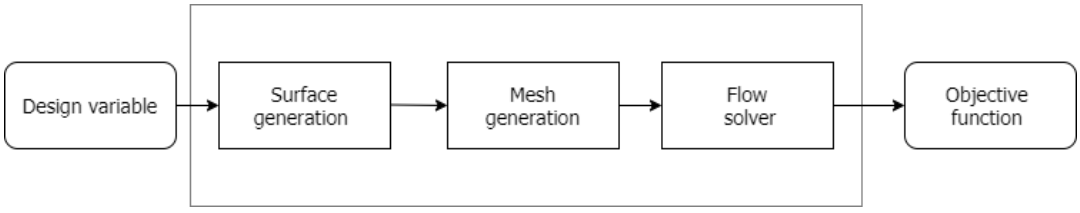

Figure 3.1: Schematic fluid-dynamic design chain in turbomachinery shape optimisation problems. Taken from [39].

3.1. Validation Hierarchy

Internal flow fields of turbomachinery are viscous, compressible and unsteady. The understanding of such a complex flow field has developed through the study of simplified models that allow the detailed investigation into a particular flow phenomena, for example, a flat plate that mimics the trailing edge of a blade [91]. Figure 3.2 presents the hierarchy of unit blade row test cases that are proposed to be studied at the ORCHID. The hierarchy has been developed based on the validation guidelines proposed by the American Institute of

Aeronautics and Astronautics (AIAA) [26] and allows the realisation of ORCHID's objectives to experimentally assess turbomachinery performance and investigate the fundamentals of gas dynamics.

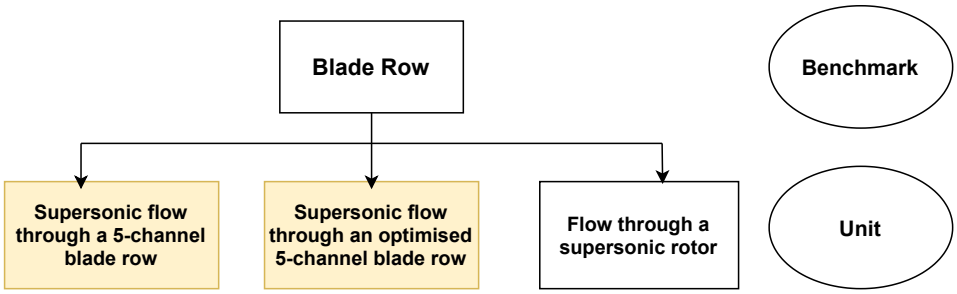

Figure 3.2: List of unit cases envisioned to validate a NICFD capable flow solver for the prediction of the flow physics inside a blade row. The yellow boxes represent the unit cases explored in this thesis.

The validation hierarchy follows a building block approach which divides a complex engineering system into progressively simpler cases: subsystem, benchmark and unit cases. The subsystem of focus in the current scope of work is the radial turbine. The blade row is a benchmark case for the stator and rotor subsystem. Such an arrangement allows for uncertainty quantification at various levels of complexity. At the time of writing the thesis, the linear cascade test section is yet to be realised. Hence, the work is an exploratory numerical approach into the design of experiments for the linear cascade where the two yellow boxes indicated in Fig. 3.2 are the unit cases studied.

3.2. An ORC Linear Blade Cascade

At present, the ORCHID at TU Delft is fitted with a de Laval nozzle test section which allows for the credibility assessment of thermodynamic models used in computational tools and a fundamental investigation of gas dynamics. The next step is to reproduce the flow physics through complex flow channels such as a stator blade channel where turbulence and transport models play a significant part. Hence, an exercise for the preliminary design of a linear cascade test section was undertaken and reported in [46], [30] and [29].The linear blade row is designed for expansions within the operating limitations of the ORCHID with inlet total pressure of 18.4 bara and total temperature of 525K to an exit pressure of 1.95 bara and exit Mach of 2.

Linear cascade test sections are extensively used in the field of experimental turbomachinery to study blade optimisation, shock-boundary layer interaction, coolant flow effects, trailing edge flows and wake mixing [51]. They are geometrically simple compared to annular or rotating cascade sections while being more realistic compared to simplified duct flows. Linear cascades introduce the aspect of flow periodicity due to the stacked arrangement of blades at a stagger angle and pitch. Additionally, they provide flexibility to adjust the flow field, operating conditions and also allow for clear flow path visualisation [51]. For true periodic conditions, an infinite number of blades is required. Given the impracticality of this, The Advisory Group for Research & Development (AGARD) [51] recommends a range of 6-15 blades for sufficient periodic flow conditions. Given the internal flow field dimensions, mass flow rate and thermal power limitations, a design choice of a 5 channel blade row was made for the ORCHID. Upstream flow uniformity ensures that the measuring passage sees the same flow conditions as the top and bottom channels. This was verified by a preliminary CFD simulation (See Fig. 3.4). Downstream of the stator, the flow is supersonic and is characterised by flow features such as shock waves, trailing edge wakes and expansion fans. The downstream periodicity is affected by reflection of shock waves from the boundaries and can influence the back pressure and be reflected back into the flow deteriorating flow periodicity. Improper flow periodicity can also interfere with any pressure or velocity measurements downstream. Although it is impossible to entirely eliminate this effect in linear cascades, use of perforated tailboards can resolve this issue to an extent [51].

Figure 3.3a presents a schematic representation of the sub-components of the cascade vapour tunnel. The entire tunnel will be mounted on a frame with a surface area of 1.4 x 1.6 m. A horizontal configuration of the blade row is selected. This configuration was selected due to advantages on the mechanical design (e.g. sealing the housing), position inside the Balance of plant and the diffuser design. A vertical configuration would require change in the position of the receiver and inlet lines. The material of choice is stainless steel and entire setup is designed for flexible use of alternate working fluids.

The Settling Chamber (SC) is equipped with instrumentation for upstream measurements and flow condi-

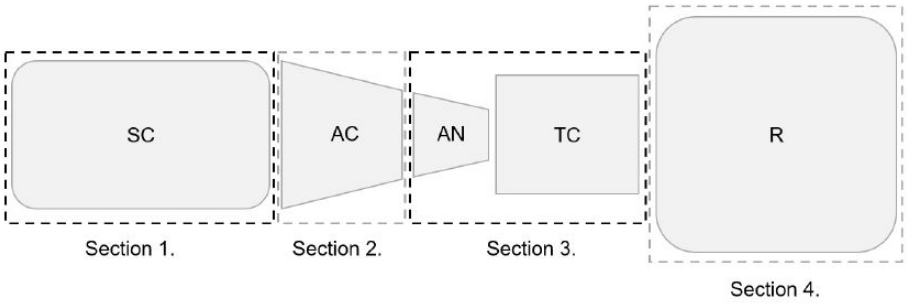

(a)

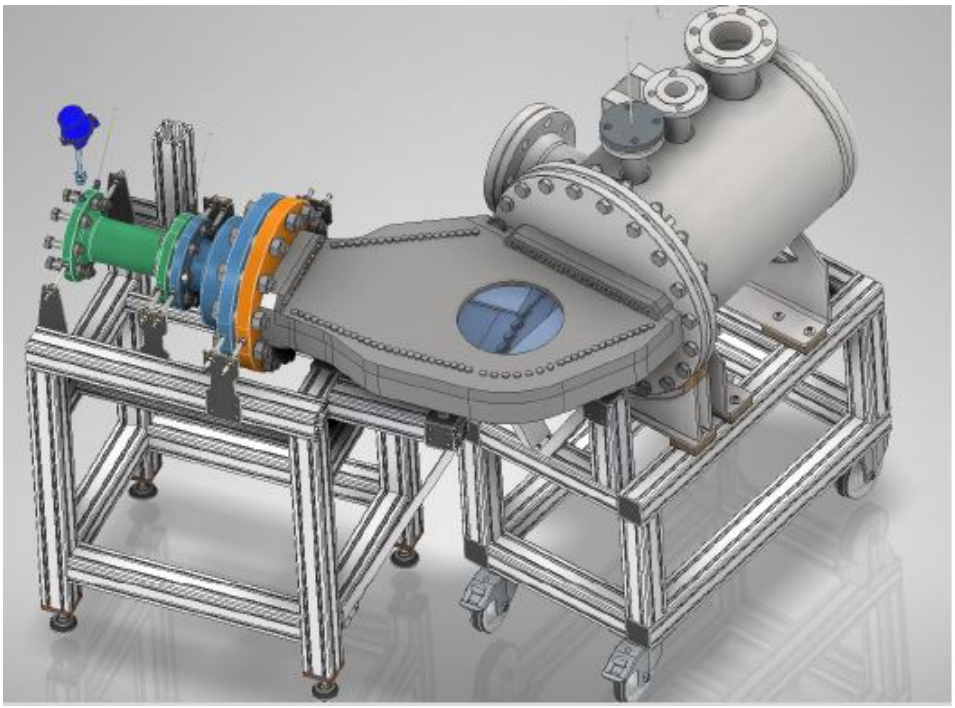

(b)

Figure 3.3: Conceptual mechanical design of the vapour tunnel and linear cascade test section. **(a)** Schematic representation of sub-components of the vapour tunnel. SC is the settling chamber, AC is the axisymmetric contraction, AN is the adjustable inlet nozzle, TC is the test channel and R is the receiver. **(b)** Layout and mechanical design of the cascade vapour test section. Reproduced from [30] and [46].

tioning devices such as screens and honeycombs. It is a cylindrical pressure vessel with maximum operating conditions of 300 °C and 25 bar. Following the SC is the axisymmetric contraction (AC) which connects the SC to the test section channel (TC). The contraction provides a geometry change from a circular to rectangular cross section resulting in increase in mean flow velocity and reducing absolute flow velocity deviations. The profile of the axisymmetric contraction is designed using the super-ellipse theorem that provides a smooth transition between the geometries. Downstream of the AC is the test section channel (TC) containing the upstream nozzle, test section and the outlet diffuser. Downstream of the test section, a diffuser recovers the kinetic energy of the flows and leads into the receiver which is a pressure vessel equipped with instrumentation for downstream pressure and temperature measurements. Further details on the flange sizing, bolt stress calculations and gasket specifications can be found in Ref. [30].

3.2.1. Measurement Techniques

The inear cascade was conceived to accommodate various measurement techniques that allowing the flow field to be fully characterised. Direct response quantities are those parameters that can be measured directly such as pressure, temperature, density etc. Depending on the required time resolution, temperature measurements, upstream and downstream of the cascade can be obtained through either thermocouples or

resistance thermometers. To enable the measurement of static pressure, the design of the measuring passage accommodates pressure taps. For total pressure measurements, the channels have been designed to avoid probe blockage effects. Design of total pressure probes that can provide both static and total pressure measurements for supersonic ORC flow is a field of active research. Compared to the perfect gas scenario, pressure probes operating in non-ideal flows requires a calibration procedure that is both fluid specific and thermodynamic condition specific [38]. The design of the blades also allows integration of heated film measurements that can enable studies into the turbulence transition, boundary layer phenomena and heat transfer in NICFD.

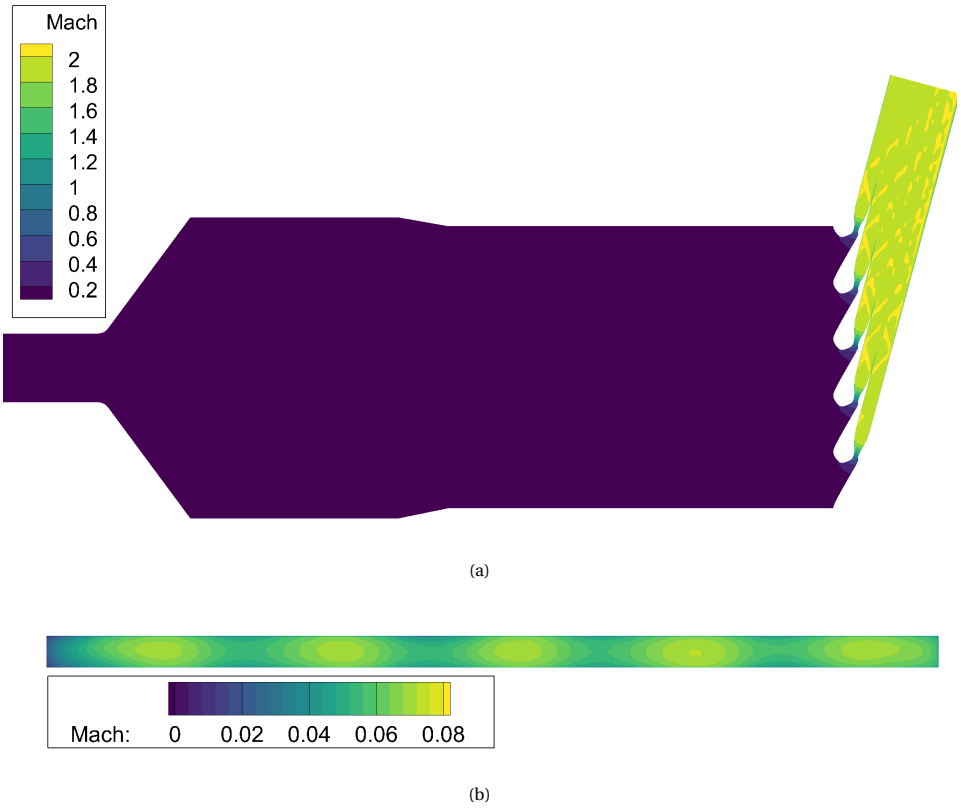

Figure 3.4: Results of the 3D RANS simulation performed on the entire linear cascade test section from the settling chamber to the exit of the test section into the receiver. **(a)** Mach contour of the test section along with streamlines. The absence of recirculation zones affirms the suitability of the selected design. **(b)** Mach contour of a sliced plane before the blade row shows the upstream flow periodicity.

The optical access window allows to resolve the Mach field through Schlieren imaging, while the velocity field can be investigated using Particle image velocimetry (PIV) or Laser Doppler velocimetry (LDV). Schlieren imaging resolves the density gradients in the flow providing images from which Mach lines and shocks can be resolved. Point-wise density measurements using the Background oriented Schlieren (BOS) method. Simultaneous pressure/ temperature and density measurements can help validate the applicability of thermodynamic models to NICFD flows. PIV and LDV are direct flow velocity measurement techniques and are more accurate compared to indirect velocity measurements where the flow velocity is inferred from temperature and pressure measurements through the fluid thermodynamic model. Both the techniques are laser based, optical flow techniques in which seed particles are introduced into the flow and their motion is tracked in time to determine the velocity of the flow. The major difference is that the LDV is a point-measurement technique which uses a photo-detector while PIV is a planar method that uses a camera. The feasibility of PIV/ LDV for dense organic vapour flows was explored in the works of [37, 49, 99]. Recently, Spinelli *et al.* [38] reported the first result of LDV measurements through a supersonic nozzle for organic vapours. Hence, the proposed linear cascade test section is designed to enable PIV or LDV measurements and work is being done to design an appropriate seeding system for the particles. Direct velocity measurements in combination with temperature or pressure measurements can enable the experimental assessment of performance metrics like

loss coefficients. These are discussed in detail in Sec. 3.3.4.

Hot wire anemometry (HWA) is a potent tool to investigate highly fluctuating flow phenomena [92], which is the case for flow through the passages of the linear cascade. The technique is based on the convection of heat between a heated thin cylinder (wire) and the fluid. Preliminary experiments with HWA in subsonic organic vapour flows were reported by [84]. The work concluded that HWA has the potential to characterise turbulence levels in organic flows although some open questions regarding improvements in spatial and temporal resolution and signal processing still remain open. Additionally, some challenges associated with HWA measurements for supersonic flow are related to the response time, laws of supersonic heat loss and interpretation of the measurements [59]. HWA measurements can be integrated into the facility following a preliminary study in the currently installed de Laval nozzle.

3.3. Uncertainty Quantification Framework

Figure 3.5 indicates the steps involved in the uncertainty quantification process. The first step requires a definition of the relevant input uncertainties and the associated uncertainty range. These are then provided as inputs to a model, which in the present study is a CFD model of the stator row. This is done through the forward propagated uncertainty quantification (UQ). The result of the forward propagated input uncertainties provides outputs with means and associated uncertainties which can then be studied by a rigorous statistical analysis. The following sections will cover the details of the UQ infrastructure employed in the study.

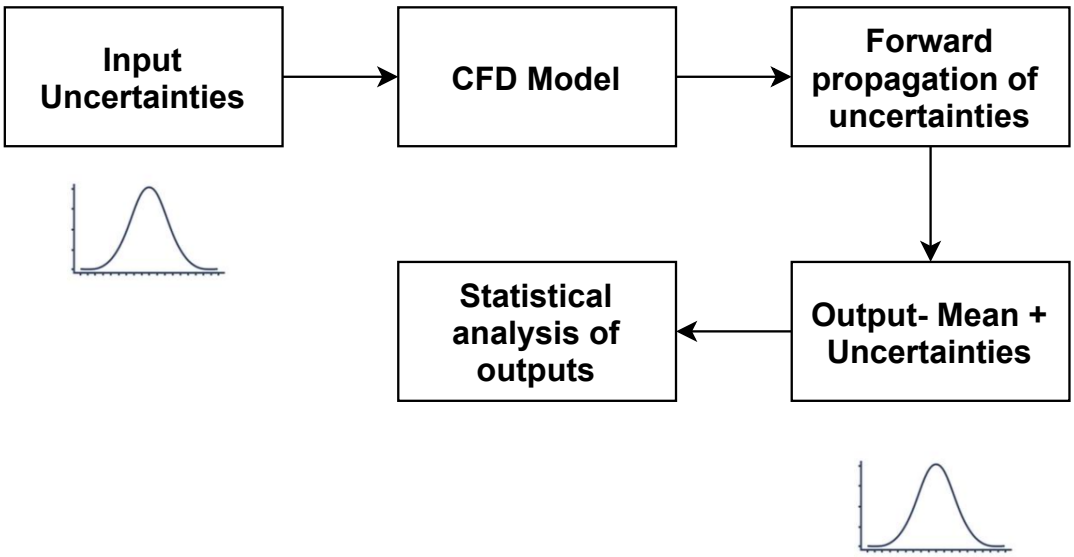

Figure 3.5: Building blocks of the Uncertainty Quantification flowchart.

3.3.1. Sources of Input Uncertainty

Model input parameters have an associated uncertainty and distribution which is often neglected when modelling the physics. They have a non- negligible effect on the model outputs. In reality, boundary conditions such as the inlet pressure or temperature fluctuate. Similarly, close to the critical region, the change of thermodynamic properties is complex and non-linear making the experimental measurements and consequent determination of critical point complicated [68, 79]. Hence, these inputs cannot be taken as absolute values and instead need to be considered with appropriate known uncertainty bands. Previous studies explored the impact of boundary condition uncertainty and thermodynamic uncertainties on the behaviour of flow [13, 55, 103]. The results from previous theses [55, 103] on a supersonic nozzle test section and the linear cascade respectively, showed that the critical point properties were dominant. Hence, in the current UQ study the uncertainty associated with determination of critical point properties is considered.

SU2 allows for only a constant viscosity or Sutherland's law implementation for modelling viscous flows. As detailed in Sec. 2.3.4, these models fail to corretly predict the transport properties close to the critical region. The complexity of variation of viscosity in the dense gas regime can be qualitatively understood by

Table 3.1: Bounds of input uncertainties considered in the present study.

Uniformly distributed input uncertainty		
Parameter	**Minimum**	**Maximum**
T_{cr} /K	511.3335	526.0665
P_{cr} /Pa	1,842,050	2,035,950
ν / Pa-s	8.1e-06	19.6e-06
Normally distributed uncertainty		
Parameter	**Nominal**	**Standard deviation**
P_o /Pa	1,840,000	1755.5

comparing the differing impact of temperature on viscosity in liquids and gases. The variation of transport model variables is included in the current UQ. Previous investigations demonstrated the negligible influence of turbulence intensity and thermal conductivity in the determination of output quantities. This could be due to the minimal influence of bulk turbulence levels on the direct response quantities and the adiabatic nature of the flow. Therefore, a choice was made to not include them in the further UQ study. Additionally, since system response functions like loss coefficients depend on the total inlet pressure, the inlet pressure boundary condition is also considered as an input uncertainty. Table 3.1 provides details on the bounds of the uncertainties considered in the present study.

3.3.2. Model Definition

The next activity in the flowchart described in Fig. 3.5 is to describe the computational model and the method of forward propagation of the input uncertainties.

Geometry & Meshing

A 2D section of the blade is selected as the geometry of interest. For verification of the 2D domain assumption, a 3D simulation of the same geometry extruded 8 mm along the span is done on the commercial CFX solver. Being a state-of-the-art flow solver, CFX was adopted as a baseline comparison against the open source flow solver, SU2. A two dimensional slice of the 3D domain is shown in Fig. 3.7. The more robust multi-parameter EoS is implemented through a lookup table provided to the solver. SST turbulence model is employed for turbulence closure. At the inlet, total pressure and temperature of 18.4 bara and 525 K are given as boundary conditions. At the outlet, a static backpressure of 1.95 bar is specified. The blades are adiabatic walls while the periodic domains are given a translational periodicity. Figure 3.19 shows the Mach contour at midspan of the blade and a comparison of static pressure plots at 10%, 50% and 90% blade span. The overlapping pressure plots confirm the 2D assumption.

Figure 3.7 shows the proposed cascade blade row section and the associated periodic single channel domain. The results from [103], verified the periodicity assumption by comparing flow quantities of the entire cascade blade row to the single blade domain. Although flow features such as reflected shockwaves introduced some deviation from the entire blade row flow field, these differences were within acceptable limits validating the study of only a single channel. Developing on some of the suggestions from [103], two modifications were introduced in the geometry namely:

- The periodic boundary was shifted to the mid channel between FBN1 and FBN2 (or FBS1). This was done keeping in mind that experimental Schlieren images will provide Mach lines along the mid plane and for an accurate validation, the geometry of the numerical domain must match with experiments.
- The trailing edge of the blade was improved by matching the pressure and suction sides such that the curves are C2 continuous, allowing for reduction in mesh skewness at the region. This is relevant to the objective of the current thesis where attention is given to the trailing edge region for computation of base pressure coefficient.

The geometry and meshing is done with the in-house tool, unstructured mesh generator 2 dimensional (UMG2) (Unstructured mesh generator 2D). A y^+ value less than 1 is maintained throughout the boundaries of the domain, as shown in Fig. 3.9a. A global mesh refinement study satisfying mesh independence and convergence criteria was done in a previous work [103]. In this thesis, a local mesh refinement at the trailing edge was performed. The mesh refinement was done keeping in mind the computational power for the

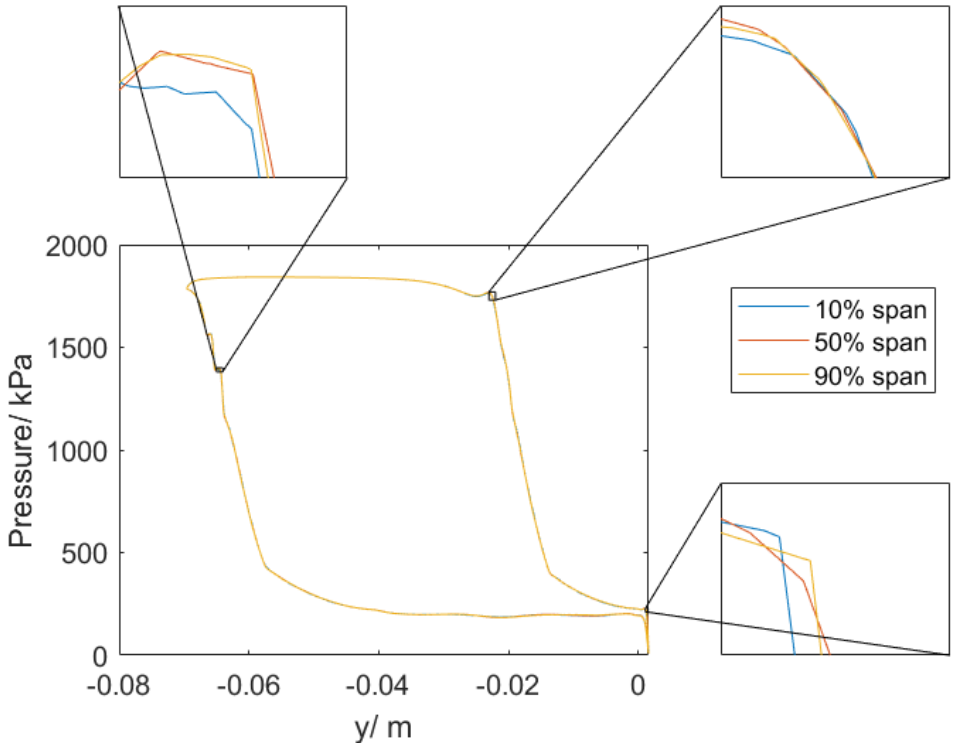

Figure 3.6: Surface pressure distribution on the blade surface at 10%, 50% and 90% span from 3D simulations done on CFX. The region around the throat and trailing edge is zoomed in for clarity.

uncertainty quantification study that will follow. Figure 3.9b shows the average base pressure values for the various local mesh refinements and Mesh 4 with a total of 199,158 elements was selected.

Flow Solver Settings

To solve the conservation equations, the SU2v5.0 flow solver is utilised [35]. The SU2 software suite is a robust, open source alternative to solve multi-physics PDE problems and PDE-constrained optimisation problems on unstructured meshes. Efforts have also been devoted to extending SU2 to solve NICFD flows [78, 105]. To run SU2, a configuration file is modified with appropriate case settings. To solve the RANS equations for compressible flow, the following modelling choices are made:

- **Turbulence model:** The Spalart-Almaras (Spalart–Allmaras turbulence model (SA)) model [93] has been implemented in accordance with previous research works. Additionally, Otero *et al.* [75], has shown that the SA model gave accurate results for fully developed non-ideal flows when compared to DNS results performed on the same case.

- **Thermophysical model:** Two EoS are available in SU2 to model non-ideal flow behaviour namely, (i) the polytropic Van der Waals EoS and (ii) the polytropic Peng-Robinson EoS. Previously, it was possible to connect external thermodynamic databases for example from FluidProp and model the non-idealities better with the more accurate non-polytropic multi-parameter EoS. For the current simulation, the polytropic Peng Robinson EoS is implemented. For the transport properties, constant viscosity and constant conductivity are chosen.

- **Boundary Conditions:** The non-reflecting Giles boundary condition is selected over the Reimann type. The need for a non-reflecting boundary condition arises from the closeness of various components in turbomachinery rendering far-field boundary conditions impractical. Alternate boundary conditions like total inflow or outflow back pressure, suffer from artificial reflection of information waves travelling through the flow. Non-reflecting boundary conditions decompose the information waves at the boundary through a Fourier transformation resolving the issue of reflections distorting the flow field. The

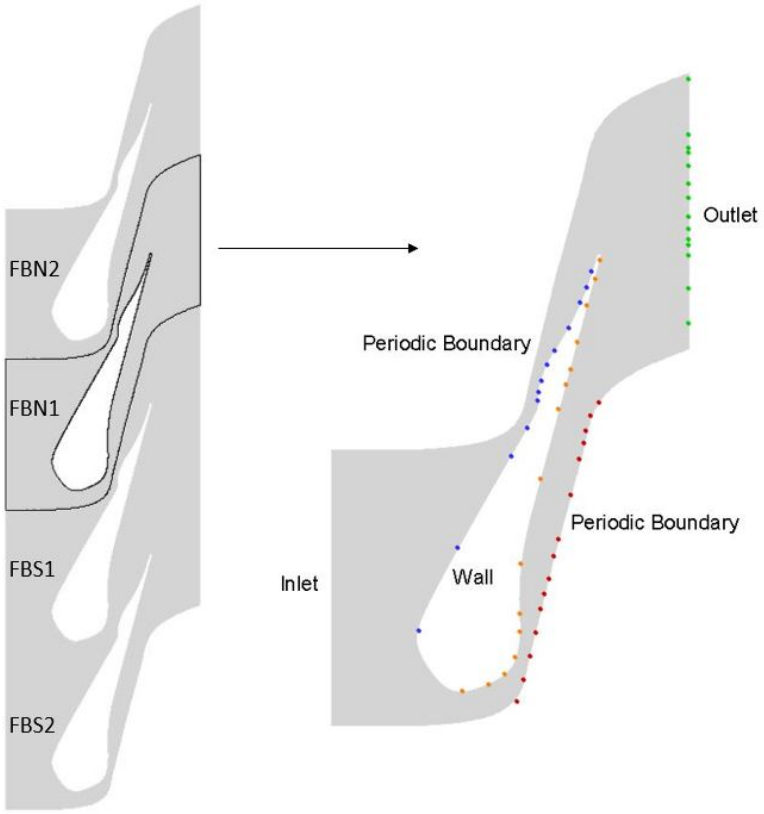

Figure 3.7: Proposed 5 channel blade row. The measuring passage is highlighted and boundary conditions are specified. The measuring location on all the boundaries indicated by the coloured dots.

numerical implementation of the Giles reflective boundary condition is beyond the scope of the thesis and the reader is directed to [81] and [40, 41] for further reading. Table 3.2 summarises the boundary conditions imposed on the domain.

Table 3.2: Boundary conditions implemented for the deterministic simulation of single blade channel.

Boundary	**Boundary condition**	**Value**
Inlet	Total temperature (K)	525
	Total Pressure (Pa)	1,840,000
Outlet	Static Pressure (Pa)	195,000
Blade wall	Adiabatic wall	-
Periodic	Periodic boundary	-

- **Numerical Scheme:** The discretisation of the advective fluxes can be done either through the upwind discretised ROE scheme or the central discretised JST scheme. Second order accuracy for the ROE scheme can be achieved by enabling the MUSCL (Monotone Upstream-centered schemes for conservation laws) feature while the Jameson-Schmidt-Turkel (JST) scheme is second order accurate by default. A comparative study by [103], identified that the two schemes show around 5% deviation in areas of strong property gradients such as the trailing edge region or shock impingement locations. Owing to its better convergence behaviour, the JST scheme was adopted. The turbulent fluxes are discretised using a scalar upwind approach with MUSCL feature enabled.
- **Solver control:** The simulation stops when either the convergence criteria of -5.5 for the density residual or maximum number of iterations (17,000) is reached. The maximum number of iterations was decided after analysing the results of a preliminary UQ study where around 3.25% of the total iterations did not converge. The CFL number is set at 5 and the solution file is rewritten after every 100 iterations.

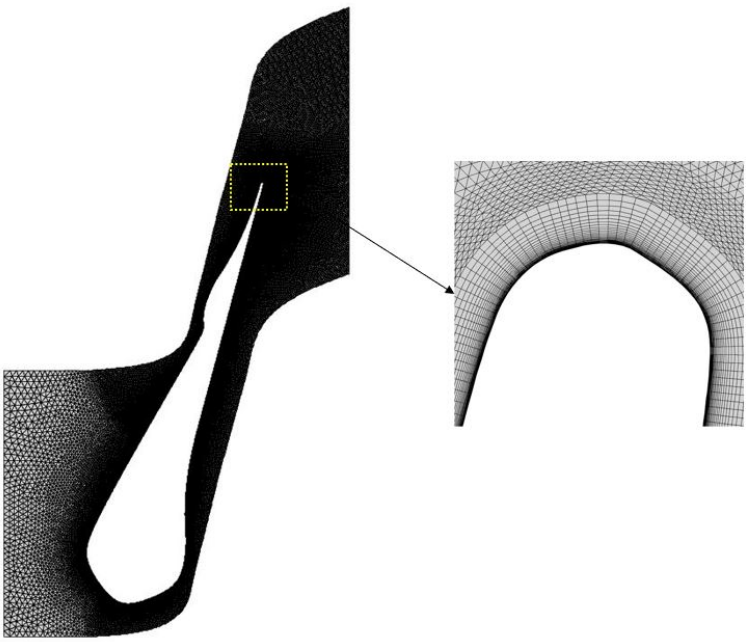

Figure 3.8: Unstructured meshing in the computational domain with focus on trailing edge mesh refinement.

3.3.3. Forward Uncertainty Propagation

The implemented method for the input uncertainty quantification is a 3rd order polynomial chaos Stochastic Collocation method with Smolyak sparse grid representation [4]. For this purpose, Dakota version 6.11 on a Linux Ubuntu 16.04 LTS operating system is used. A python 2.7 interface with additional MATLAB post-processing codes calculates the required response functions. To run the UQ, the following files need to be modified: (i) the Dakota input file, (ii) SU2 configuration file, (iii) Python scripts and (iv) MATLAB scripts. Figure 3.10 shows the top level of the UQ infrastructure. The forward propagation of the input uncertainties results in outputs with uncertainties as well. A statistical analysis of first order moments like mean and second order moments like standard deviation is manually computed. The total expanded input uncertainty is twice the standard deviation (2σ) and represents a 95% confidence interval.

The effect of the sources of uncertainty can be identified using a variance based decomposition (variance based decomposition (VBD)) sensitivity study. This is useful in identifying which input uncertainties are more influential on the response functions. The sensitivity of a parameter is represented by the Sobol index which is generated automatically by the Dakota tool. The Sobol index reflects the degree of variation of the response function Y due to the input x_i. The primary Sobol index is defined as,

$$S_i = \frac{\mathrm{Var}_{x_i}\left[E\left(Y \mid x_i\right)\right]}{\mathrm{Var}(Y)} \tag{3.1}$$

It captures the effect of an input parameter independent of all other input parameters. The total Sobol index is,

$$T_i = \frac{\mathrm{Var}(Y) - \mathrm{Var}\left[E\left(Y|_{x_{-i}}\right)\right]}{\mathrm{Var}(Y)} \tag{3.2}$$

where $x_{-i} = (x_1, \ldots, x_{i-1}, x_{i+1}, \ldots, x_m)$ represents the effect of an input parameter independently and in combination with other input parameters. Higher the Sobol index, more sensitive is the response function to that particular input parameter. For a well converged UQ, the sum of the primary Sobol indices is equal to one while the sum of the total Sobol indices is greater than one. A negative Sobol index is nonphysical and could indicate an insufficient sample size.

3.3.4. Response Quantities

Direct response quantities (direct response quantities (DRQ)) are those quantities that are directly measured through measurement techniques discussed in Sec. 3.2.1. They are: (i) pressure, (ii) temperature, (iii) density, (iv) flow velocity, (v) Mach number and (vi) total pressure. System response quantities (system response

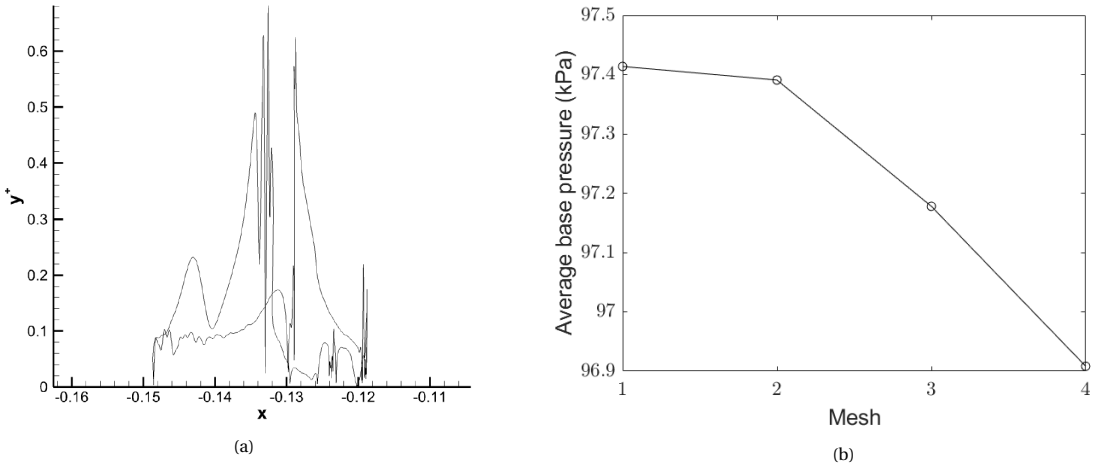

(a) (b)

Figure 3.9: **(a)** y^+ value along the domain boundaries. **(b)** Average base pressure mesh convergence plot.

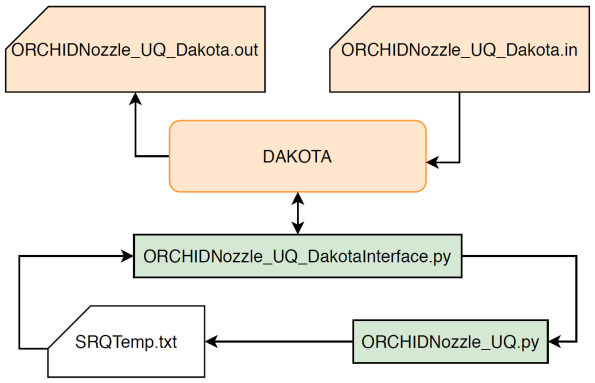

Figure 3.10: Top level of the UQ infrastructure. Taken from [13].

quantities (SRQ)) are derived from the direct measurements and help characterise the performance of the system by taking into account various loss mechanisms that affect the overall efficiency. The system performance metrics are derived from averaged flow parameters at the inlet and outlet of the system.

For computing the flow quantities at the exit, different averaging techniques can be employed such as: (i) Area averaging, (ii) Mass-flow averaging and (iii) Mixed-flow averaging. The averaging of the variables at the inlet and outlet plane converts the values from a spatially non-uniform initial state to a single value representative of flow at that particular station. This is crucial in thermodynamic analysis of gas turbine components since they use single values for the calculations. The selection of averaging procedure has been quite arbitrary although literature such as [76] discuss the suitability of each method. Area averaging is the simplest form of averaging and more suited for experimental validation studies while mass flow averaging approaches are extensively used in CFD studies and for compressible flows. A more robust treatment of the averaging is the mixed-flow averaging which assumes the flow undergoes a mixing process to a final uniform state. The averaged values are obtained by an iterative procedure which solves the mass, momentum and energy conservation equations. In the present study a mass flow averaging procedure is implemented. If the flow quantity to be mass averaged is given by ϕ, the mass averaged valued along the n discretised points is calculated as,

$$\overline{\phi} = \frac{\sum_i^n \phi_i * f_{1,i} * \sqrt{(x_{i+1} - x_i)^2 + (y_{i+1} - y_i)^2}}{\sum_i^n f_{1,i} * \sqrt{(x_{i+1} - x_i)^2 + (y_{i+1} - y_i)^2}} \tag{3.3}$$

$$f_{1,i} = \rho_i v_i \tag{3.4}$$

where ρ_i is the density and v_i is the normal velocity at the discretised node. Once the mass flow averaged values are computed, the following system performance metrics can be derived [32] (1 refers to the inlet and 2 to the outlet shown in Fig. 3.7):

- **Pressure loss coefficient:**

$$C_p = \frac{\overline{P_{01}} - \overline{P_{02}}}{\overline{P_{02}} - \overline{P_2}} \tag{3.5}$$

where P_{01} is the inlet total pressure, P_{02} is the outlet total pressure and P_2 is the static pressure at the outlet. This definition of the pressure loss coefficient is called the stagnation pressure loss coefficient and is commonly used due to the ease of calculating it from cascade test data [32].

- **Kinetic energy loss coefficient:**

$$\zeta_{\mathrm{KE}} = \frac{2(\overline{h_2} - \overline{h_{2s}})}{\overline{v_2}^2} \tag{3.6}$$

where h_2 is the exit enthalpy and h_{2s} is the isentropic exit enthalpy. The isentropic enthalpy is the ideal case of the enthalpy assuming an isentropic expansion. It can be calculated using the entropy known at the inlet and the pressure at the outlet. The kinetic energy loss coefficient is commonly used to account for both boundary layer and mixing losses [87].

- **Entropy loss coefficient:**

$$\zeta_s = \frac{2\overline{T_{01}}(\overline{s_2} - \overline{s_1})}{\overline{v}^2_{\mathrm{spout},2}} \tag{3.7}$$

where,

$$\overline{v_{\mathrm{spout},2}} = \sqrt{2(\overline{h_{01}} - \overline{h_{2s}})} \tag{3.8}$$

The spouting velocity at the exit indicates the velocity which has associated kinetic energy equal to the isentropic enthalpy difference *i.e,* the velocity that the flow would have in the case of an isentropic process. s_1 and s_2 are the inlet and outlet entropy and T_{01} is the total temperature at the inlet.

- **Base pressure loss coefficient:**

$$C_{\mathrm{pb}} = \frac{\overline{P_b} - \overline{P_{02}}}{\overline{P_{02}} - \overline{P_2}} \tag{3.9}$$

where $\overline{P_b}$ is the average base pressure around the trailing edge region where the triangular dead water region is present. The region right behind the trailing edge is region of mixing between the supersonic flow on the suction surface and sonic flow on pressure surface. The base region is triangular (refer Fig. 3.11) and characterised by a lower constant pressure and it is usually followed by a shock that is generated when the flows turn to a common flow direction [33].

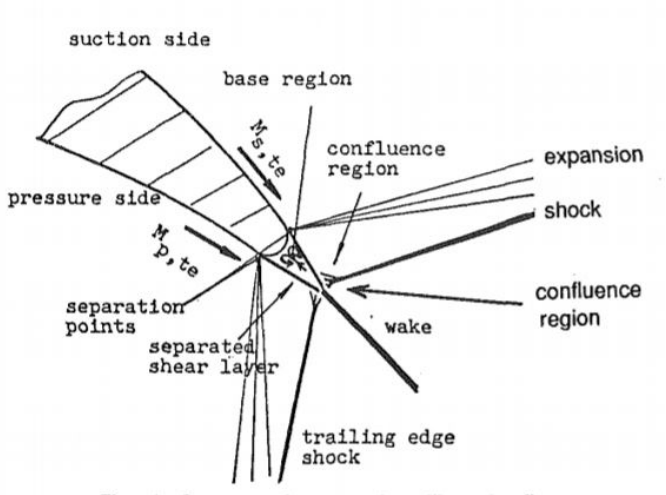

Figure 3.11: Structure of supersonic trailing edge flow. Taken from [33].

- **Flow uniformity parameters:** The flow uniformity at the exit of the stator is an important quantity that has effects on the performance of the rotor downstream. Hence, the standard deviations of the exit flow

angle and Mach number along the N points along the outlet are computed as,

$$\sigma_\beta = \sqrt{\frac{\sum \left(\beta - \beta_{\text{mean}}\right)^2}{N}} \tag{3.10}$$

$$\sigma_{M_2} = \sqrt{\frac{\sum \left(M_2 - M_{2,\text{mean}}\right)^2}{N}} \tag{3.11}$$

where β is the outlet flow angle and M_2 is the outlet Mach.

From the perspective of experimental validation, it is possible to measure the pressure loss coefficient using a combination of static pressure and PIV/LDV measurements. The base pressure loss coefficient can also be computed from a pressure tap placed at the trailing edge of the stator. Additionally, with PIV/LDV measurements one can also get information on the flow uniformity at the exit. Kinetic energy loss and entropy loss coefficients depend on the selection of the thermodynamic model and require atleast two direct response quantities measured at the location. Hence, these metrics are of secondary interest experimentally.

3.4. Results and Discussion

In this section, the results from the uncertainty quantification exercise will be presented. A comparison between the mid-span slice of the 3D CFX simulation will be presented. Following this, a discussion on the uncertainty quantification results for the baseline and optimised geometry cases will be presented.

3.4.1. Comparison of 3D and 2D Simulations of the Stator Channel

Three dimensional simulations of the stator channel were performed on the Ansys CFX platform with the same boundary conditions as described in Tab. 3.2. Due to some challenges faced with using the Peng-Robinson non-ideal gas model within CFX, a Lookup table generated from RefProp which uses the multi-parameter Span Wagner model, was used. Although different models were used between the two, the surface pressure plots on the blade are in close agreement with each other. The CFX solution shows no pressure dip at the location of the shock impingement on the suction side (See (1) in Fig. 3.12a). Similarly along the periodic boundary, the pressure and Mach trends are similar, although a lower Mach number is observed at the outlet and the disturbances due to trailing edge wake and reflected shock are attenuated. Similarly, at the outlet the pressure distribution is more uniform as compared to the two-dimensional SU2 simulation. This could be due to reduction in shock strength due to 3D effects. The change in density along the periodic domain predicted by the two simulations superimpose each other as seen in Fig. 3.12e.

Table 3.3 reports the outlet mass flow averaged values and performance metrics. A lower total pressure at the outlet is observed from the 3D CFX simulation and this translates to differences seen in the loss coefficients. The flow uniformity at the exit represented by the standard deviation of the flow angle and exit Mach are similar from both the simulations. The higher base pressure loss coefficient could be attributed to the different turbulence model used in the 3D CFX simulation.

Table 3.3: Comparison of mass flow averaged properties at the outlet and performance response quantities between the 2D SU2 and 3D CFX simulation of the stator channel.

	Mass flow average	
@ Outlet	**2D SU2**	**3D CFX**
Static Pressure/ kPa	195.5	195
Mach	2.003	1.92
Total Pressure/ kPa	1742.4	1363
Flow Angle/ °	74.81	74.3

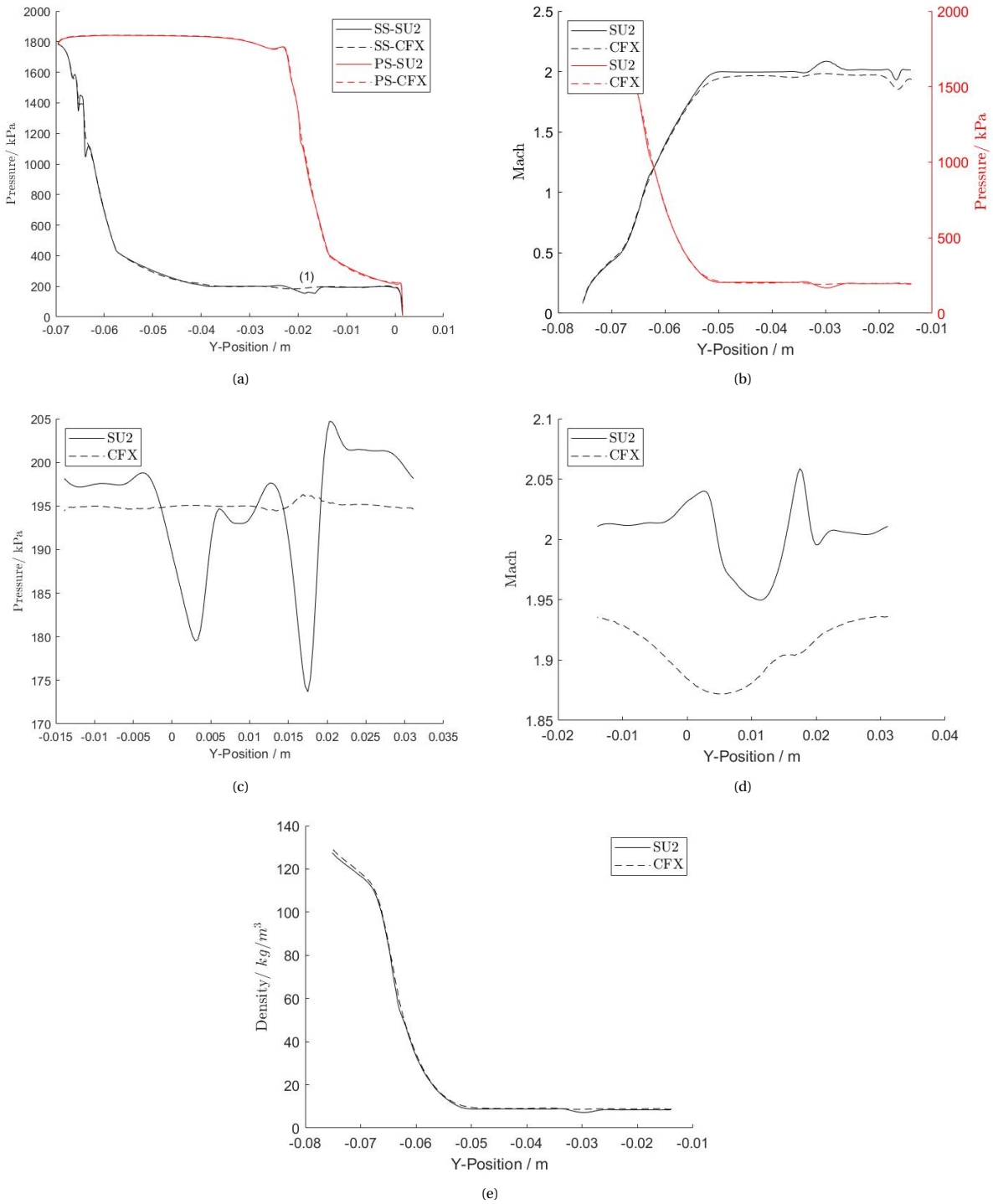

Figure 3.12: Mid span of 3D CFX simulation compared against SU2 2D simulations. **(a)** blade static pressure , **(b)** periodic pressure and Mach, **(c)** outlet pressure, **(d)** outlet Mach and **(e)** periodic density. The 3D CFX simulation uses a Span-Wagner multi-parameter EoS while the 2D SU2 solution uses the Peng-Robinson EoS.

3.4.2. Expanded Input Uncertainties- Baseline

The uncertainty quantification was performed using the Dakota tool [4] and employed a stochastic collocation method with 3 sparse grid levels. The computation took a total CPU time of 3898.4 seconds and a wall time of 358276 seconds (approx. 4 days) on a machine with 20 physical dual core processors (2 x Intel(R) Xeon(R) CPU E52687W v3 @ 3.10 GHz) and 64 GB of RAM. A total of 215 iterations were required for four input uncertainties to generate the surrogate model. It was also observed that when the exit iterations were 5000, there were around 7 unconverged iterations, *i.e.*, the density residual was more than -5.5. This was identified by studying the scatter plots for system response functions. The exit iteration count was increased to 17,000 in order to minimise the number of unconverged solutions. This was checked and confirmed that it does not pose any problems for the calculation of the sobol indices nor forming the surrogate. The statistical convergence of two exemplary response functions namely the trailing edge pressure and pressure loss coefficient are plotted in Fig. 3.13. The figures indicate a satisfactory level of statistical convergence that is essential to building an accurate surrogate model.

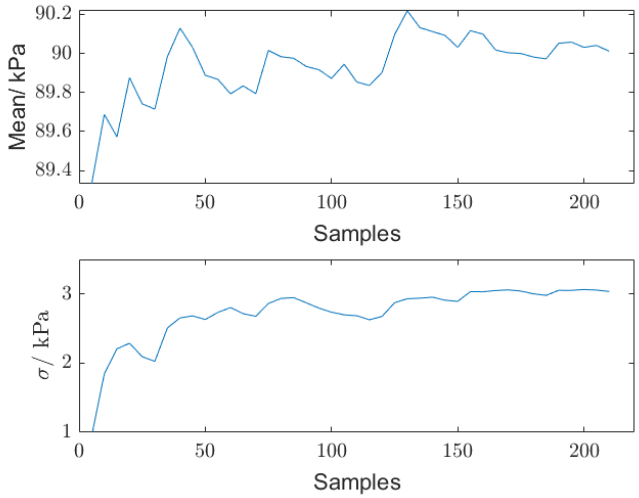

(a)

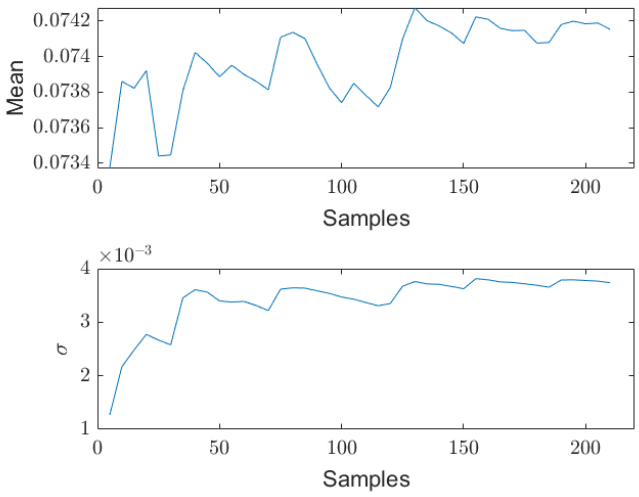

(b)

Figure 3.13: Statistical convergence plots of mean and standard deviation of **(a)** trailing edge pressure and **(b)** pressure loss coefficient.

Figure 3.14 shows the Mach contours for the expansion of MM through the single stator passage. Flow features such as reflected shocks, wake and base region are indicated. The base region, shown in Fig 3.14b is a triangular region of constant low pressure. As seen in Fig. 3.14a, at the outlet there is an interaction of

different flow features generated by the measurement blade and the blade below. Entropy generation ($\frac{s-s_{in}}{s_{in}}$) contour plot shown in Fig. 3.14c shows maximum values near the trailing edge region where the pressure and suction side flows interact.

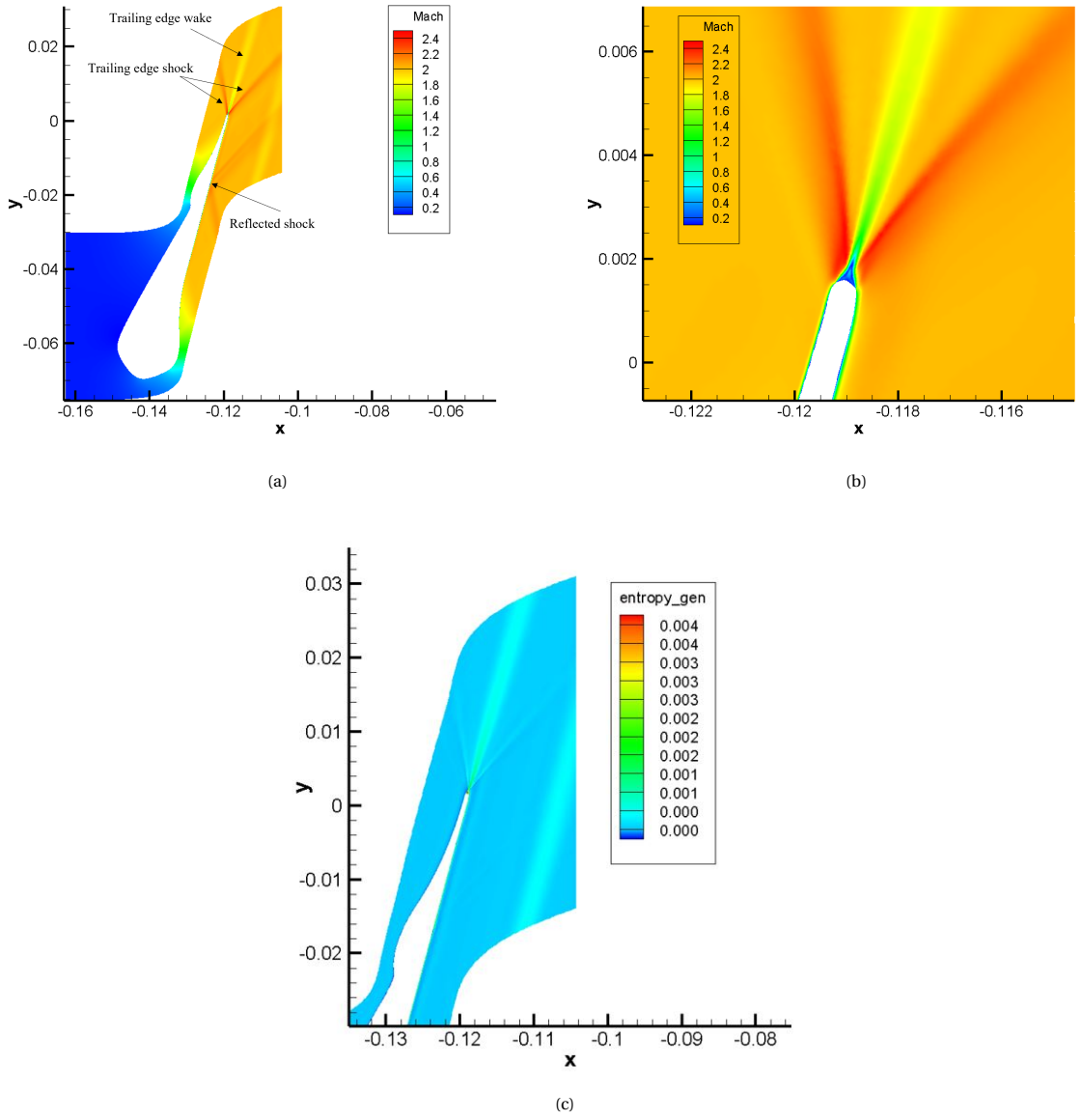

Figure 3.14: **(a)** Mach contours for the single blade channel expansion.**(b)** Base region, shock and wake generated at trailing edge of the blade.**(c)** Entropy generation contours along the stator passage.

Figure 3.15a reports the static pressure profile along the stator with 2σ expanded input uncertainties evaluated at the selected measuring locations. The expanded input uncertainties and means are derived from a statistical analysis of the response function outputs from the uncertainty quantification study. Figure 3.15b reports only the expanded input uncertainties (not relative to the mean). Higher uncertainties are observed at the throat region where there is significant pressure gradients and at the measuring station where the shock is reflected on the pressure side of the blade (See (1) and (2) in Fig. 3.15a). Nevertheless, the uncertainty is below 5% of the mean value even in areas of steep gradients such as the throat. The Figures 3.15c and 3.15d show the Sobol indices of the model input parameters namely, the critical point properties, the total pressure and the viscosity. These indices show the relative importance of the model input parameters and their influence on the response quantity pressure. On the suction side, a slight increase in the influence of viscosity and total inlet pressure is observed in the region of shock reflection. This could possibly be due to the interaction

of the shock with the boundary layer in that region.

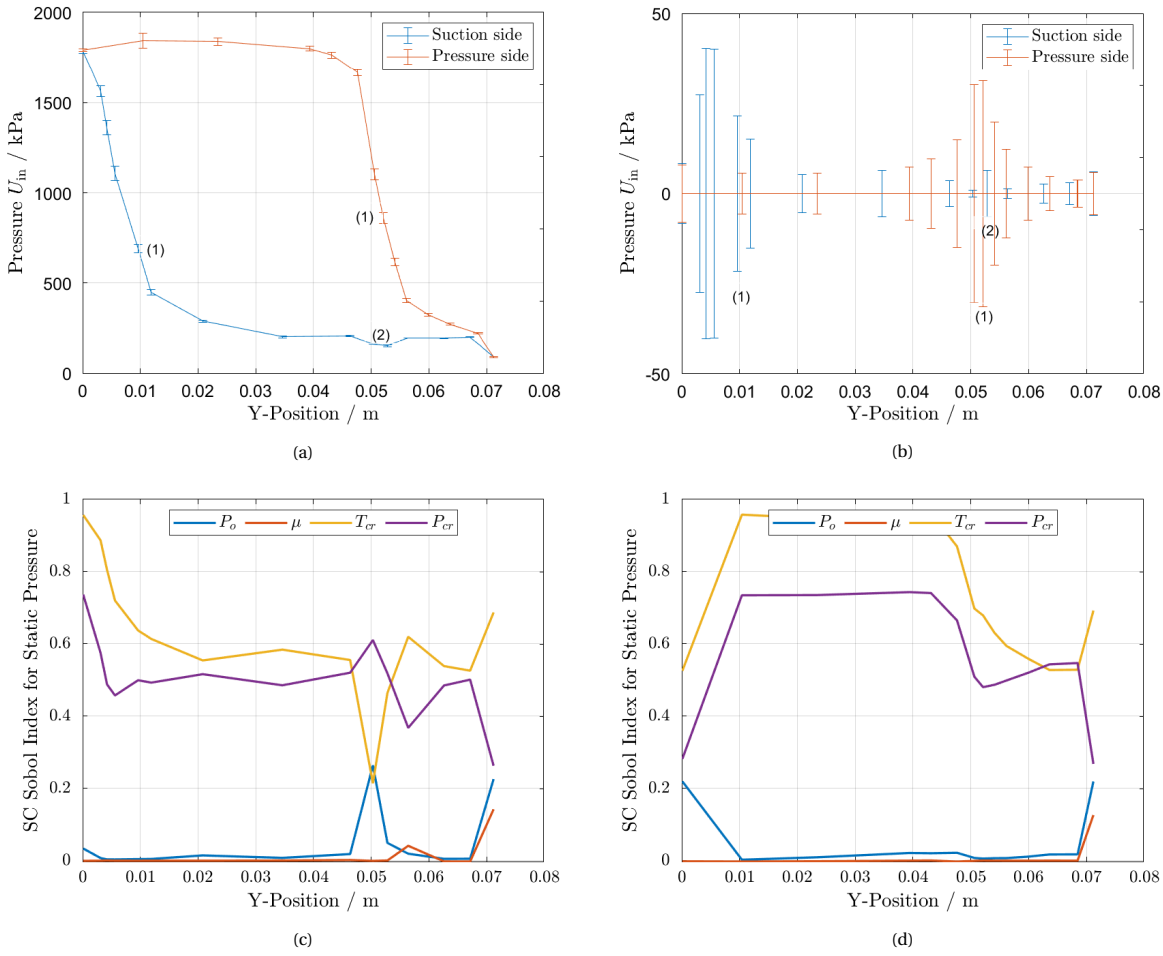

Figure 3.15: **(a)** Surface pressure plot with 2σ expanded input uncertainty indicated by the error bars. (1) indicates the throat regions on the pressure and suction side of the blade while (2) shows the position of the reflected shock wave indicated in Fig.3.14. **(b)** 2σ expanded input uncertainties along the measuring stations located on the blade. **(c)** Sobol indices for the suction side of the blade. **(d)** Sobol indices for the pressure side of the blade.

The Mach number along the periodic boundary can be experimentally captured through schlieren imaging. Figure 3.16a shows the change in Mach number and static pressure along the periodic boundary. The two plots are complementary to each other as expected. The uncertainty at the throat for Mach number is negligible because the flow is choked, and as a result, the Mach number has to be 1 at the throat. At the same location, larger pressure uncertainty is observed due to the steep gradients at the throat. The Mach uncertainty prior to the throat can be explained by analysing the trend for change in speed of sound through the channel, plotted in Fig. 3.16b. The Mach number is the ratio of local flow velocity to the speed of sound. Prior to the throat, the flow is in the non-ideal regime where the speed of sound depends on the local pressure (or density) (Refer Eqn. 2.31) which in turn is governed by the choice of EoS. As seen in Fig. 3.16b, the ideal gas predicts a 84% higher speed of sound compared to the PR model in the initial non ideal phase of the expansion. This reduces to 6.7% at the end of the expansion where the flow is in the ideal region. As indicated in Sec. 2.3, the PR implementation depends on the critical properties of the fluid and thus the predictions are expected to be strongly dependent on the input uncertainties associated with the critical point properties. Hence, the uncertainties associated with thermodynamic state properties (like pressure and density) and derived properties (like the speed of sound) are larger in the non-ideal regime due to dependence on critical point properties. This uncertainty is then propagated to quantities like the Mach number along the periodic channel. The reasoning behind the stronger influence of critical point properties is supported by the consistently larger influence of critical point properties in the Sobol plot shown in Fig. 3.16c. The Sobol plot for

static pressure shown in Fig. 3.16d shows a slight increase in influence of inlet pressure and viscosity in the region where the trailing edge wake crosses the periodic boundary. This behaviour is consistent with Sobol plots for static pressure on blades which also showed an increased importance of total pressure and viscosity in areas of wake or shock wave reflections.

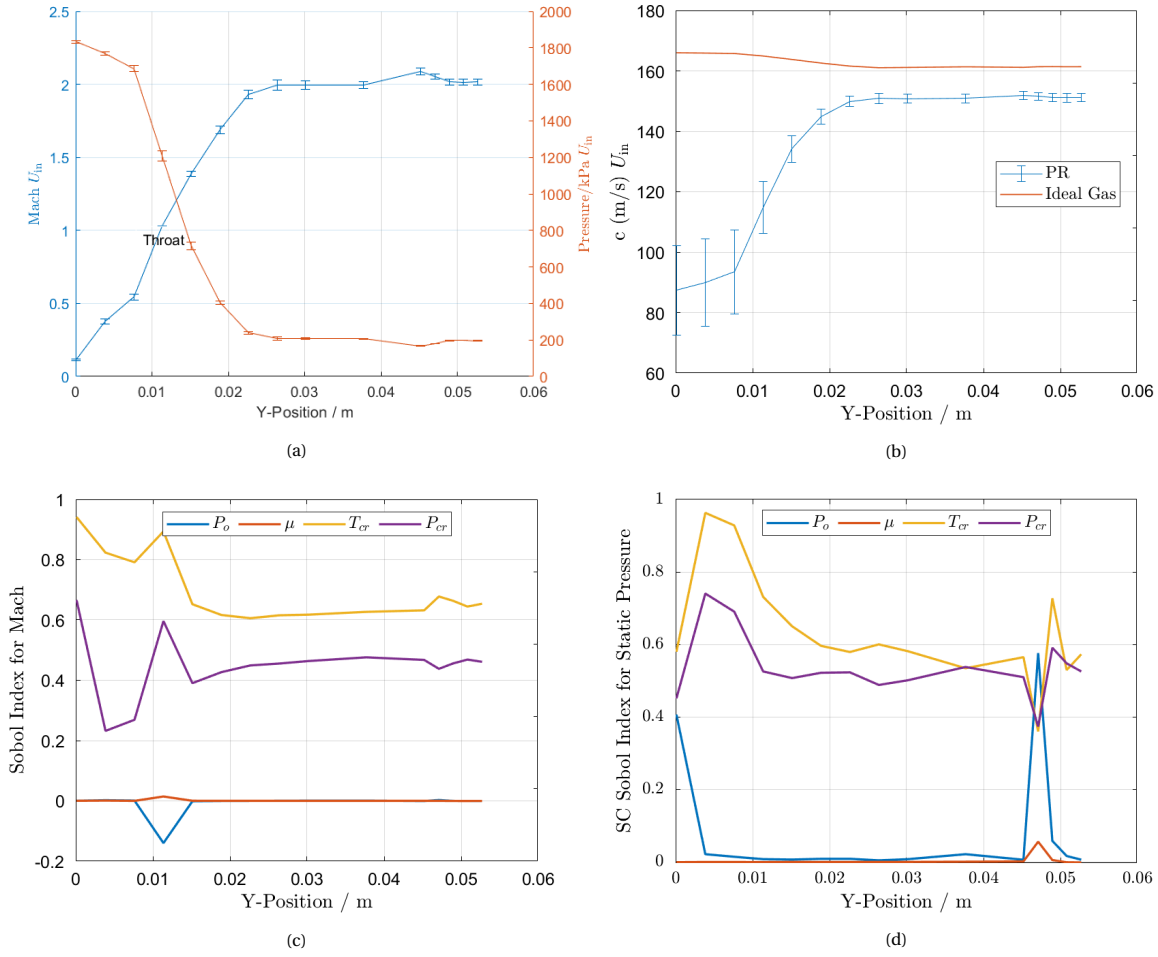

Figure 3.16: **(a)** Mach and static pressure plot along the periodic channel with 2σ uncertainties indicated by the error bars. **(b)** Speed of sound with 2σ error bars plotted along the periodic channel. The change in speed of sound along the channel for the ideal gas case is also plotted for comparison. **(c)** Sobol indices for periodic Mach. **(d)** Sobol indices for periodic static pressure.

At the outlet of the periodic domain, there is an interaction of various flow features generated from the expansion such as wake and shocks. Figure 3.18a shows the complementary pressure and Mach profiles at the outlet with 2σ expanded input uncertainty bands. The regions where the reflected shock, trailing edge wake and trailing edge shocks meet the outlet boundary are indicated by (1), (2) and (3) respectively in Fig.3.20. Higher uncertainties are also observed in these regions. Given the proposed plan to perform Particle Image Velocimetry (PIV) measurements, the Mach number trends at the outlet can be experimentally verified. Also installing pressure taps along the outlet at the locations identified in the thesis can support simulation results. The critical point properties continue to be dominant inputs even in the ideal region at the outlet. In the ideal regime, thermo-physical PR predictions are closer to ideal gas and one can assume that critical point uncertainties might not be that relevant. It could be hypothesised that upstream effects of thermodynamic model uncertainties are propagated to the ideal region at the outlet.

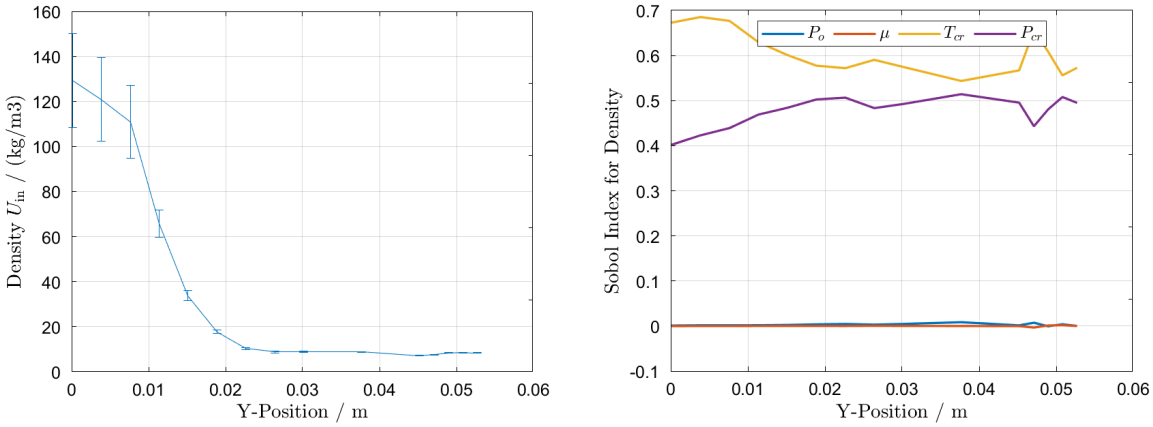

Figure 3.17: **(a)** Density along with expanded input uncertainty errorbars extracted along the periodic domain. **(b)** Sobol indices for periodic density.

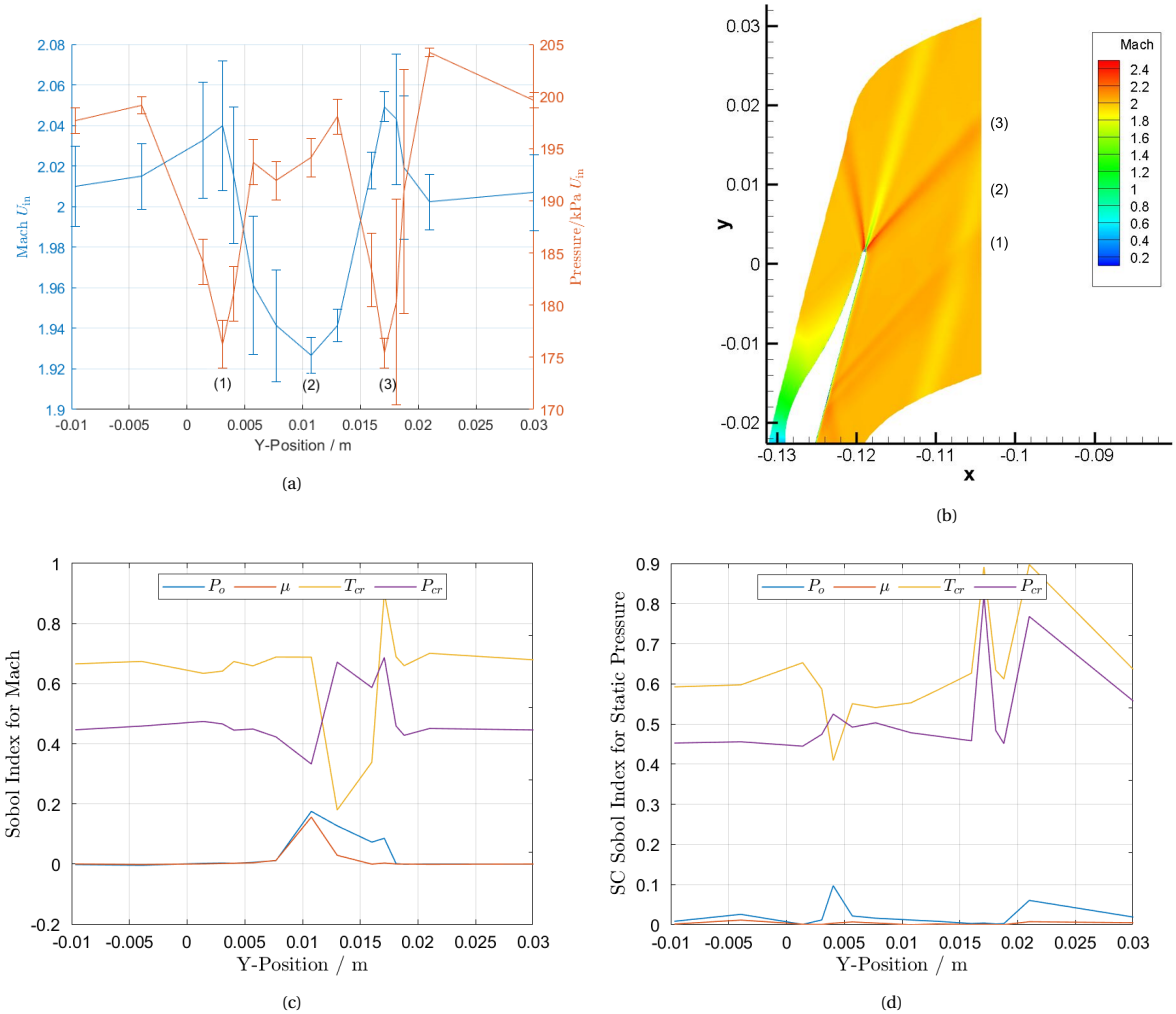

Figure 3.18: **(a)** Mach along the outlet measuring stations with 2-sigma expanded input uncertainty indicated by the uncertainty bands. **(b)** Effect of flow features such a reflected shock waves and wake at the outlet of the periodic domain.

In the present study, in addition to direct response quantities like pressure and Mach along the bound-

aries, other performance metrics have also been included. These performance metrics were discussed in Sec. 3.3.4. Table 3.4 summarises the mean, 2σ expanded input uncertainties along with the uncertainty percentage over the mean. It reports the calculated Sobol indices for all the system response quantities as well. Cases which gave negative sobol index values (unphysical results) are not reported. The values demonstrate the importance of accurate evaluation of critical point properties over other inputs. The viscosity becomes significant for the evaluation of base pressure coefficient and this is expected given the interaction of suction, pressure side flows in the region. Nevertheless, despite the broad range of viscosity uncertainty used, it shows negligible influence on the response functions. Hence, the use of a constant viscosity assumption is acceptable for the given case although this study can be continued for more turbulent flow cases or different geometries. For the measured response quantities like Mach and pressure, the inlet boundary condition seems to have negligible influence. Hence, the fluctuations which are inherent to the ORCHID setup can be considered acceptable for the validation exercise.

Table 3.4: Mean, 2σ expanded input uncertainties and associated total Sobol indices for the system response functions computed from the baseline geometry. Negative Sobol indices have been omitted.

Response Quantity, ϕ	$\overline{\phi}$	2σ	$2\sigma/\overline{\phi}\%$	**Total Sobol Index**			
				$\mathbf{P_o}$	μ	$\mathbf{T_{cr}}$	$\mathbf{P_{cr}}$
Pressure loss coefficient, C_p	0.0742	±0.0075	10.8	-	0.0079	0.9758	0.7634
Kinetic energy loss coefficient, ζ_{KE}	0.1147	±0.03447	30.05	0	0.0018	0.8179	0.6456
Entropy loss coefficient, ζ_s	0.1179	±0.0355	30.07	0	0.0018	0.8288	0.6521
Base Pressure loss coefficient, C_{pb}	-0.0649	±0.0706	5.08	0.4991	0.2713	0.3656	-
SD exit flow angle, $\sigma_{\beta 2}$	1.244	±0.0706	5.67	0.0219	0.0015	0.5959	0.5782
SD exit Mach, σ_{M2}	0.0329	±0.0036	11.08	0.0510	0.0423	0.4001	0.5299

3.4.3. Comparison of Baseline and Optimised Geometry

The discrete adjoint based unconstrained optimisation was performed on the baseline geometry with the objective function to reduce entropy generated. Figure 3.19a shows the convergence history for the optimisation. Design iteration 5 was selected as the geometry of interest for comparison. The new geometry achieved a 6.5% improvement in entropy generation, where improvement means reduction in entropy generation. Although design 6, achieves an even higher reduction in entropy generation, it is not considered because of the significantly higher mass flow rate. Figure 3.19b shows the geometry changes observed between the baseline (indicated in black) and optimised (indicated in red) blade designs. Very minute changes are observed at the throat regions on the suction and pressure side of the blade.

Figure 3.20a shows the comparison between the baseline and optimised surface pressure distributions on the blade predicted by deterministic simulations. The positions of observed geometry changes are indicated by the dotted magenta lines. On the suction side, higher static pressures are observed for the optimised case. The same trend is observed on the pressure side right before the trailing edge where the geometry was modified. The periodic Mach and pressure showed no differences and are not presented here. Figures 3.20b, 3.20c and 3.20d show the Mach, static pressure and exit flow angle plots at the outlet. A slight geometry change in the blade propagates flow physics effects downstream. Two observations from the outlet Mach and pressure plots can be made: (i) the range of variation is reduced , i.e., the flow is more uniform and (ii) higher Mach and lower pressure values are observed for the optimised geometry. This is particularly beneficial for the performance of the stator. Exit flow angle also forms a component of flow uniformity and from Fig.3.20d, it is seen that flow angles at the bottom and top of the outlet is around 2% different for the optimised case in comparison to the baseline. Surprisingly, the change in exit Mach and pressure profiles are not reflected in the mass flow averaged values shown in Tab. 3.5. The exit Mach shows negligible increase and this is propagated to a 4% improvement in pressure loss coefficient. While the standard deviation for the outlet Mach has improved by around 7% , the standard deviation of exit flow angle has increased by 31.5%. Performance parameters such as the kinetic energy loss coefficient and entropy loss coefficient show a slight improvement of 0.5%. Experimentally, it is possible to verify the improvements in pressure loss coefficient but this strongly depends on the precision of the measuring technique, which is a challenge for supersonic non-ideal flows.

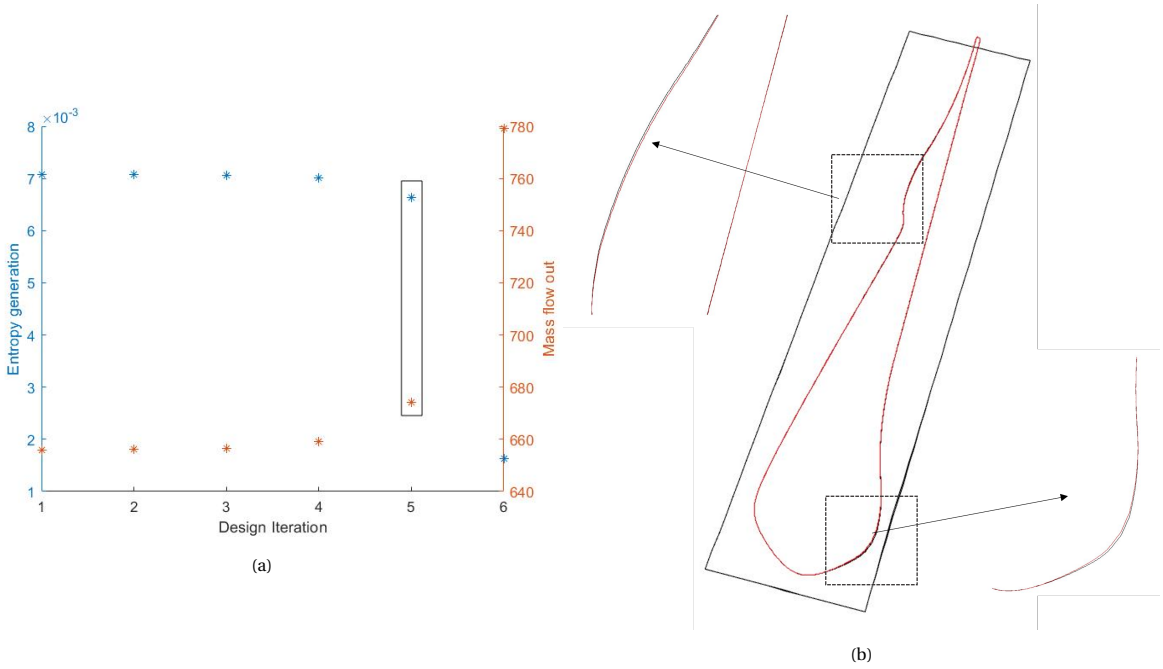

Figure 3.19: **(a)** Adjoint optimisation history. Design 5 (indicated by the rectangle) is selected for comparison against the baseline. **(b)** Deformed and baseline geometry for design case 5. (-) indicates the baseline geometry while (-) indicates the optimised geometry.

Table 3.5: Comparison of mass flow averaged properties at the outlet and performance response quantities between the baseline and optimised geometry.

	Mass flow average		Area flow average	
@ Outlet	**Baseline**	**Optimised**	**Baseline**	**Optimised**
Static Pressure/ kPa	195.5	195.86	194.8	194.6
Mach	2.003	2.0032	2.0041	2.0045
Total Pressure/ kPa	1742.4	1746	1739	1737.8
Flow Angle/ °	74.81	74.28	74.81	74.28
Performance Response Quantities				
Pressure Loss Coefficient, C_p	0.0625	0.06	0.0648	0.0656
Kinetic Energy Loss Coefficient, ζ_{KE}	0.1089	0.1083	0.1093	0.1093
Entropy Loss Coefficient, ζ_s	0.1124	0.1119	0.1128	0.1128
Base Pressure Loss Coefficient, C_{pb}	-0.078	-0.079	-0.078	-0.0788
SD exit flow angle, $\sigma_{\beta 2}$	1.1822	1.5542	1.1822	1.5542
SD exit Mach, σ_{M2}	0.0257	0.0238	0.0257	0.0238

3.4.4. Expanded Input Uncertainties- Optimised

To test the robustness of the deterministic optimised design, a UQ study was performed on the optimised blade design with the same input uncertainties of inlet pressure, viscosity and critical point properties. The expanded input uncertainty on the blade surface and the outlet is shown in Fig. 3.21. In comparison to the uncertainty distribution in Fig. 3.15b, a 19% reduction in input uncertainty of the pressure is observed at the throat. This could be attributed to the slight geometry change in the region. At the outlet, higher expanded uncertainties of Mach and pressure are observed at the regions where the trailing edge wake and reflected shock impinge the outlet. Although qualitatively this is similar to the baseline case shown in Fig. 3.18a, the expanded input uncertainties in the regions indicated have reduced (for instance, at region (1) where the trailing edge wake meets the outlet, the Mach expanded input uncertainty for the optimised case has reduced by 24% compared to the baseline case). The behaviour of sobol indices is consistent with the baseline case where the critical point properties were the dominant input uncertainties. The means and expanded uncertainties of the performance parameters are presented in Tab. 3.6. As discussed in Sec. 3.4.3, the optimisation has improved the pressure loss coefficient, entropy loss coefficient and Mach uniformity

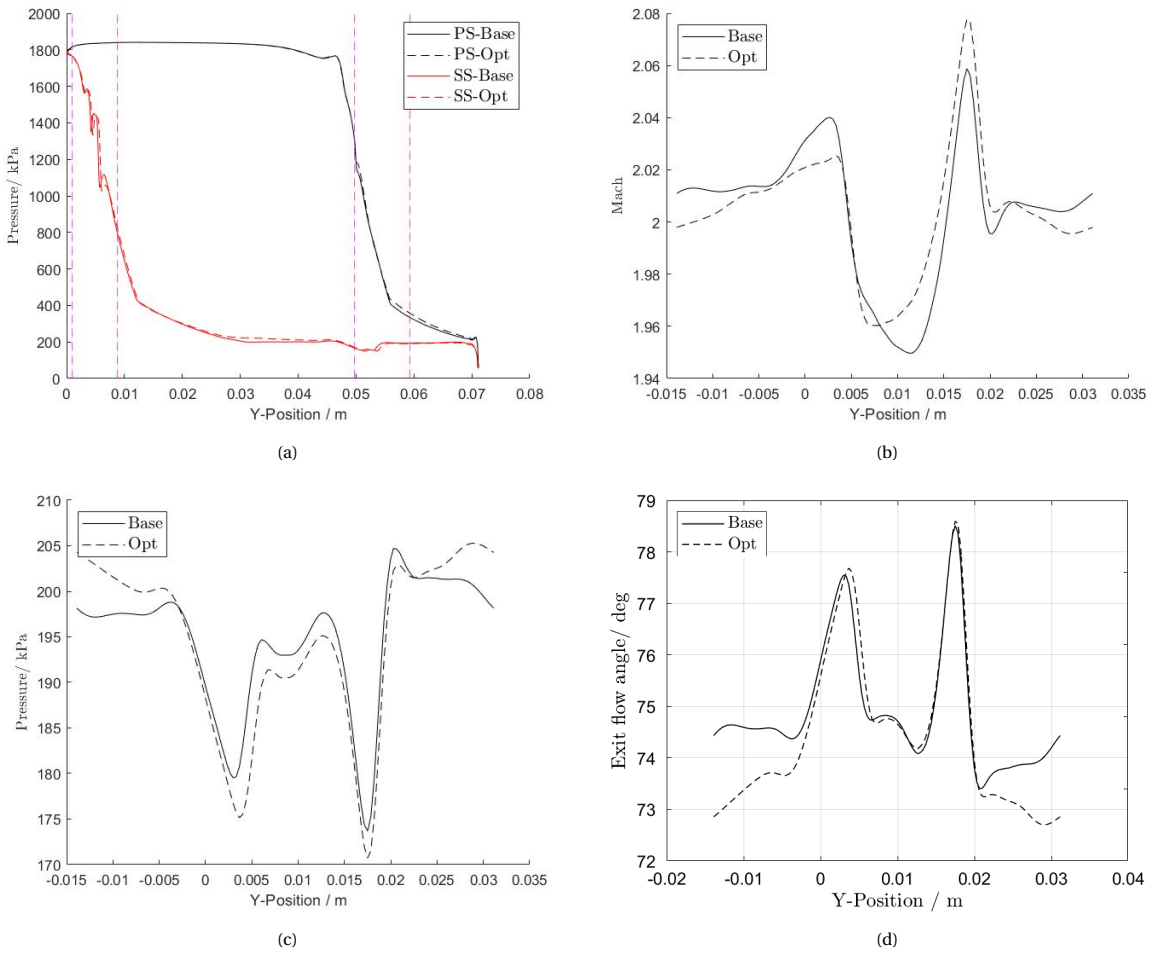

Figure 3.20: Comparison plots of deterministic simulation results of baseline and optimised geometries. **(a)** Static pressure distribution on blade surface (the dotted magenta lines indicate region of geometry change), **(b)** Outlet Mach distribution, **(c)** Outlet static pressure distribution, **(d)** Outlet flow angle distribution.

at the exit. The expanded input uncertainty has improved by 18.5% for the pressure loss coefficient. This is interesting to validate from an experimental perspective. The unconstrained optimisation has compromised on the flow uniformity at the exit with increase in uncertainties for standard deviation of both Mach and flow angle. In this case, a constrained optimisation with outlet flow angle or Mach as a constraint can yield better flow properties at the outlet of the stator.

The adjoint optimised geometry discussed above is a single-point design procedure (deterministic optimisation) where the effect of variation of operating conditions is not taken into account. On the other hand, a robust optimisation takes into account the variability of one or more input parameters. The objective of such an optimisation is to reduce the variability of the system performance, thereby improving the robustness of a system. This is relevant to design of ORC stators given the fluctuations in operating conditions and presence of strong shock waves at off-design conditions at the outlet which leads to performance deterioration [77]. For a more robust optimisation accounting for uncertainties in operating conditions, two approaches exist in literature: a multi-point optimisation and a stochastic optimisation design methodology [77]. Romei et al. [86] studied the robustness of deterministically optimised designs under flow and turbulent boundary condition uncertainties. The aim of the work was to justify the need for computationally expensive robust optimisation methods. The deterministic optimisations were performed with two independent objective functions: (i) minimisation of entropy generated and (ii) minimisation of standard deviation of azimuthal pressure distribution downstream of the trailing edge. The mass flow rate was constrained within 1% of the base value. The work concluded that certain techniques of deterministic optimisations like constrained optimisation resulted in robust designs. Pini et al. [77] performed a multi-point optimisation which minimises both the mean and standard deviation of a given function on a supersonic cascade. The work considers the

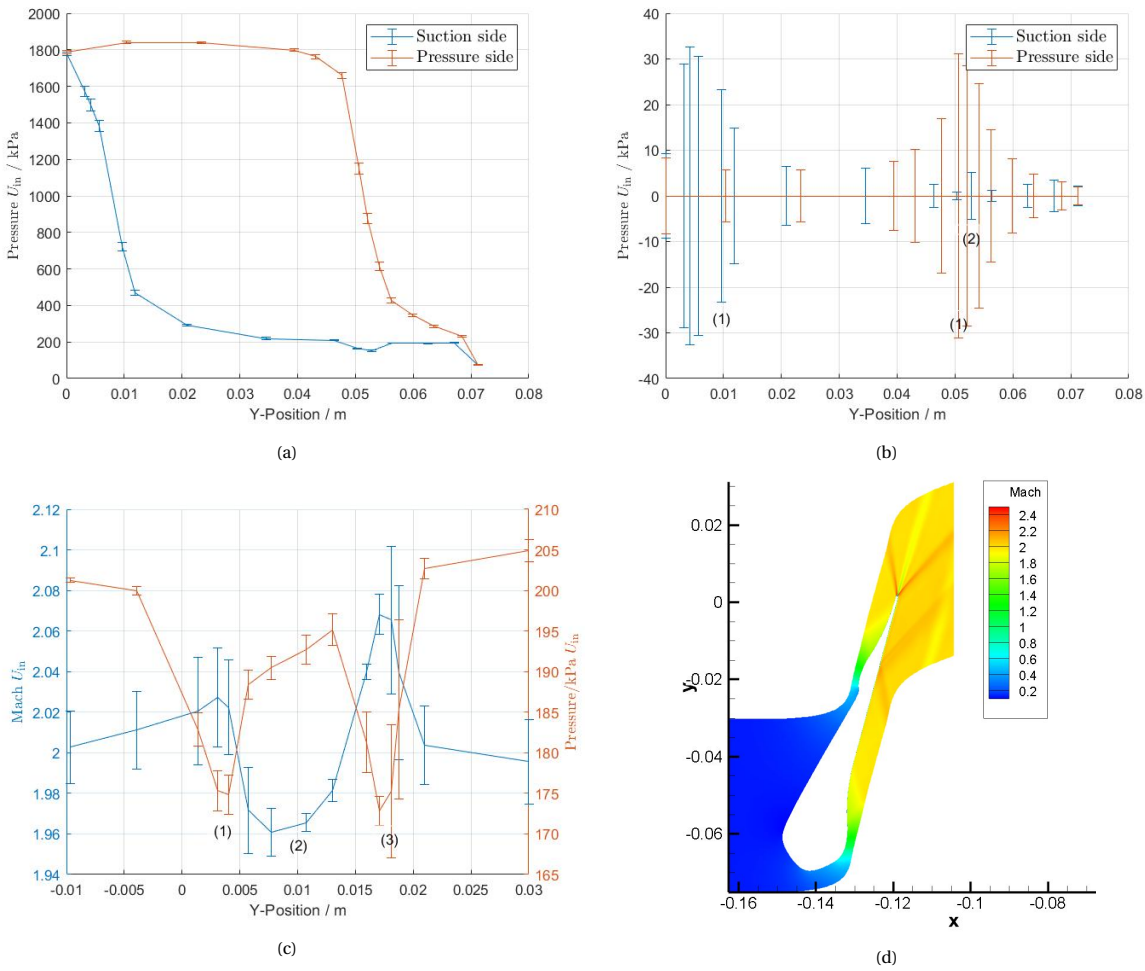

Figure 3.21: **(a)** Surface pressure plot with expanded input uncertainty errorbars for the optimised geometry, **(b)** Expanded input uncertainties of static pressure at the blade surface, **(c)** Mach and pressure distribution at outlet and **(d)** Mach contours for the optimised geometry.

back pressure to be an aleatory uncertainty. A comparison between the baseline, single point and multi point optimised blade designs showed an improvement in terms of both the mean and standard deviation for the multi-point case. Thus, the multi-point approach resulted in a more robust blade design. In the work by Cinella et al. [50], a turbine cascade operating in the dense gas regime was optimised using a multi-objective genetic algorithm. A Probabilistic collocation method is used to ascertain the effects of upstream thermodynamic condition uncertainties. The objective of the optimisation was to simultaneously maximise the mean turbine efficiency while minimising the variance of power output. A comparison was done between 3 pareto front candidates and a deterministic optimisation case. While the deterministic case yielded a higher turbine efficiency, the robust designs could maintain a low variability of power output affirming the proposed advantages of a robust optimisation methodology despite the elevated computational costs. Work from Congedo et al. [82] applied a quantile-based Bayesian optimisation framework for a robust ORC turbine cascade optimisation with boundary operating conditions as aleatory uncertainties. The objective function was the standard deviation of the pressure distribution downstream of the trailing edge. The conclusions were in line with similar previous studies that confirm the improved robustness from a multi-point optimisation methodology compared to a deterministic optimisation. Although the scope of the optimisation in the present work is restricted to a deterministic case, a multi-point optimisation of the stator design will provide valuable insights into the robustness of the stator. Validating the robustness experimentally under off-design conditions will also be a first in the ORC community. The results presented in this section serve as a first step towards assessing the robustness of a deterministic optimisation using a DOE approach.

Table 3.6: Mean, 2σ expanded input uncertainties and associated total Sobol indices for the system response functions from the optimised geometry. Negative Sobol indices have been omitted.

Response Quantity	$\overline{\phi}$	2σ	$2\sigma/\overline{\phi}\%$	**Total Sobol Index**			
				$\mathbf{P_o}$	μ	$\mathbf{T_{cr}}$	$\mathbf{P_{cr}}$
Pressure loss coefficient, C_p	0.0606	±0.0054	8.88	0.0515	0.0047	0.7711	0.537
Kinetic energy loss coefficient, ζ_{KE}	0.1102	±0.0398	36.14	0	-	0.5797	0.4925
Entropy loss coefficient, ζ_s	0.1139	±0.0413	36.29	0	-	0.5799	0.4932
Base Pressure loss coefficient, C_{pb}	-0.0753	±0.00095	1.26	-	0.707	0.002	-
SD exit flow angle, σ_2	1.568	±0.1460	9.3142	0.0083	0.0039	0.5290	0.4917
SD exit Mach, σ_{M2}	0.0240	±0.0036	14.97	0.0083	0	0.5041	0.4858

3.5. Summary

The purpose of the chapter was to identify relevant metrics to quantify the performance of the stator and assess the variation of output quantities of the stator under the selected input uncertainties. Amongst the identified metrics, the pressure loss coefficient, base pressure loss coefficient and standard deviation of exit flow angle and Mach can be experimentally studied using the linear cascade test section. Challenges related to total pressure probes operating in the dense gas supersonic regime is still a open question that needs to be explored. It is possible to install a total pressure measurement at the receiver for this purpose. The base pressure loss coefficient can be investigated by placing a pressure tap close to the trailing edge of the stator. Future particle image velocimetry (PIV) experiments can provide information on the flow velocity at the outlet and Schlieren visualisation can provide Mach data. From the uncertainty quantification performed on the baseline geometry, it was observed that higher pressure expanded input uncertainties are observed close to the throat due to the large pressure gradients. The Sobol indices are in agreement with previous results that concluded the elevated importance of the critical point properties over boundary condition uncertainties. The study also supports the use of a constant viscosity value for the simulation, based on the fact that it has negligible influence on the response quantities.

The subsequent unit test case planned at the ORCHID is a study of the flow through an optimised stator row. To assess, the possibility of such a study an optimised blade design from a deterministic adjoint based shape optimisation was compared with the baseline case. A 4% improvement in the pressure loss coefficient and enhanced Mach uniformity at the exit is observed. But the unconstrained optimisation has resulted in compromise on flow angle uniformity at the exit. A constrained optimisation could yield better flow uniformity at the outlet. The results of the UQ study on the optimised geometry show reduced uncertainties for certain metrics like the pressure loss coefficient. However, no strong conclusions regarding the robustness of the deterministic optimisation can be made without a comparison with a stochastic or multi-point optimised blade design. Nevertheless, from an experimental perspective, the geometry and performance changes for the optimised design are too minimal to be realised given the present machining tolerances and instrumentation sensitivities. It is possible that the baseline stator is optimally designed and the unit case can progress to studying the rotor cascade. From a numerical perspective, it might be interesting to compare deterministic and stochastic optimisation designs and analyse any improvements in the robustness of the stator.

4

Experimental NICFD: Oblique Shock Waves

Experimental data for NICFD flows is quite limited due to challenging operating conditions such as high temperature, vicinity of the flow to the saturation curve and the thermal stability limits of the working fluid. Existing wind-tunnel facilities cannot be easily refurbished to accommodate the experiments to investigate fundamentals of NICFD flows or performance of ORC expanders. Therefore, construction of new test facilities and associated measurement campaigns is of interest to the community. Given the combined temperature and pressure requirements for organic working fluids, conventional wind tunnels cannot be used for NICFD experiments and novel vapour tunnels are required. Based on the mode of operation, the tunnels can be classified as intermittent or continuous. The choice is based on a trade-off analysis between the planned experiments, test section dimensions, thermal input/output required/discharged by the facility and the required equipment [5, Chapter 4].

The main facilities for research into the expansion of organic vapours are (i) the CLOWT at Muenster University of Applied Sciences [83], (ii) the Test rig for organic vapors (TROVA) at the CREA lab of Politecnico di Milano [95], (iii) the FAST [67] and ORCHID at TU Delft [48] and (iv) the Imperial College Dense gas blowdown facility [85]. Table 4.1 summarises the salient features of the facilities and the subsequent section will discuss in detail the design and operation of the ORCHID at the TU Delft.

Table 4.1: Specifications of NICFD experimental vapour tunnels.

Facility	**Type**	**Working fluid**	**Operating conditions**
CLOWT, Muenster University	Continuous	Novec^{TM}649	T_{max}=150°C; P_{max}= 6 bar
TROVA, Politecnico di Milano	Blowdown	MDM Siloxane	T_{max}= 400°C ; P_{max}= 50 bar
ORCHID, TU Delft	Continuous	MM Siloxane	T_{max}= 300°C; P_{max}= 25 bar
City University, London	Closed-loop	R1233zd	T_{max}= 125°C; P_{max}= 20 bar
Imperial College, London	Blowdown	R1233zd(E)	T_{max}= 138°C; P_{max}= 20 bar

This chapter reports two representative isentropic expansions that were performed at the ORCHID facility. The details of the facility, test section and measurement capabilities are discussed in Sec. 4.1 and 4.2. Following this, the experimental test matrix and the post processed results are presented in Sec. 4.3 and Sec. 4.5. Finally, a comparison of experimental measurements against CFD simulations is discussed in Sec. 4.6.

4.1. The ORCHID

The Organic Rankine Cycle Hybrid Integrated Device (ORCHID) is a continuous supersonic vapour tunnel and turbomachinery facility at the Power & Propulsion (P&P) facility at TU Delft, Netherlands [48]. The ORCHID is conceived for both fundamental studies on NICFD flows and for testing of ORC components, initially high-speed mini ORC turbines and later heat exchangers. It features a balance of plant implementing a high-temperature regenerative organic Rankine cycle. Two different test sections are closely *integrated* into this BoP, and they can be alternatively fed and used, thus making the setup *hybrid*. The first one is a nozzle with

optical access to perform fundamental experiments, whose research objectives are (reproduced from [5]): (i) to verify the NICFD theoretical fundamentals, and (ii) to validate the CFD flow solvers implementing the related thermodynamic models and turbulence models. The second is a test-bench for mini-ORC expanders of any configuration (i.e., turbines, scroll, screw, and piston) up to a power output of 80 kWe, whose aim is to provide data to validate or develop semi-empirical correlations for fluid dynamic losses, to assess design methodologies, and to evaluate the accuracy of CFD tools. The ORCHID can be operated with a variety of working fluids. The maximum achievable working fluid temperature and pressure can be as high as 300°C and 25 bar respectively, allowing for the realization of a wide range of thermodynamic regimes of interest for NICFD studies and ORC applications namely: subcritical, supercritical, and two-phase liquid-vapor expansions [5]. Table 4.2 summarises the operating conditions of the ORCHID.

(a) Isometric view of the ORCHID.

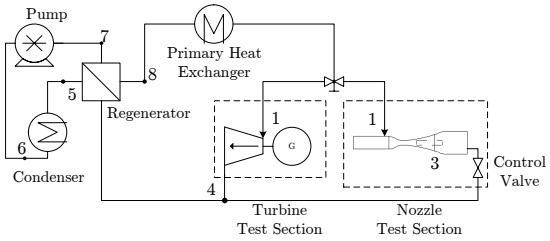

(b) Simplified PFD of the ORCHID [48].

Figure 4.1: **(a)** Isometric view and **(b)** simplified PFD of the ORCHID facility at the Propulsion & Power (PP) lab, TU Delft. Taken from [48].

4.1.1. Balance of Plant

The configuration of the balance of plant for the ORCHID is illustrated in the Process and Instrumentation Diagram (Process and Instrumentation Diagram (PID)) shown in App. A. A detailed discussion on the BoP is beyond the scope of the thesis and the reader is directed to [5, Chapter 5]. Briefly, the process flow diagram of the facility contains three fluid loops (the reference colour in the P&ID is indicated within brackets): (i) the heating loop (red), (ii) the working fluid loop (orange) and, (iii) the cooling loop (blue). The nozzle test section can be isolated from the working fluid loop by means of a bypass line and two pneumatically actuated gate valves. The working fluid loop is subdivided into a high-temperature and low-temperature section. The high

Table 4.2: Main design specifications for the ORCHID balance of plant [5, Chapter 5].

Working Fluid Loop	
Maximum temperature / $^{\circ}C$	300
Maximum pressure / bara	25
Volume flow rate range / l/min	10-140
Maximum condensing pressure / bara	5
Maximum temperature in the condenser / $^{\circ}C$	90
Heating loop	
Maximum temperature/ $^{\circ}C$	320
Maximum thermal power/ kW	400

temperature section extends from the booster pump (D2/item3) and the orifice plate OR01 (B4) in the bypass line. The low temperature loop is the return line of the vapour from the outlet of the test section to the fluid buffer vessel. All piping is made of stainless steel. The main component of the cooling loop is the centrifugal pump (D6/item 17) and the aircooler. The coolant used is a mixture of water and ethylene glycol. Heat is supplied to the system by an electric heater which is a bank of resistors. The heat transfer fluid, *Therminol VP1* in turn heats up the working fluid in the evaporator. The maximum power output for the electric heater is 400 kW_{th} and maximum working fluid pressure is at 25 bara. The temperature and pressure of the working fluid loop was set to 5 bara and 150°C. The nominal mass flow rate of the main pump of the facility is 136 l/min (2.2 x 10^3 m^3/s). The entire system is connected to a vacuum system which is essential to remove the non-condenseable gases in the loop and verify leak tightness. Vacuum tests are performed before every start-up of the system.

4.1.2. The Nozzle Test Section

The installed nozzle test section at the ORCHID is designed as a modular system containing three compartments: (i) the settling chamber, (ii) the nozzle housing and, (iii) the receiver as shown in Fig. 4.2. Each of the compartments and the design of the profile itself are discussed in brief. For a detailed description, the reader is guided to [5, Chapter 6].

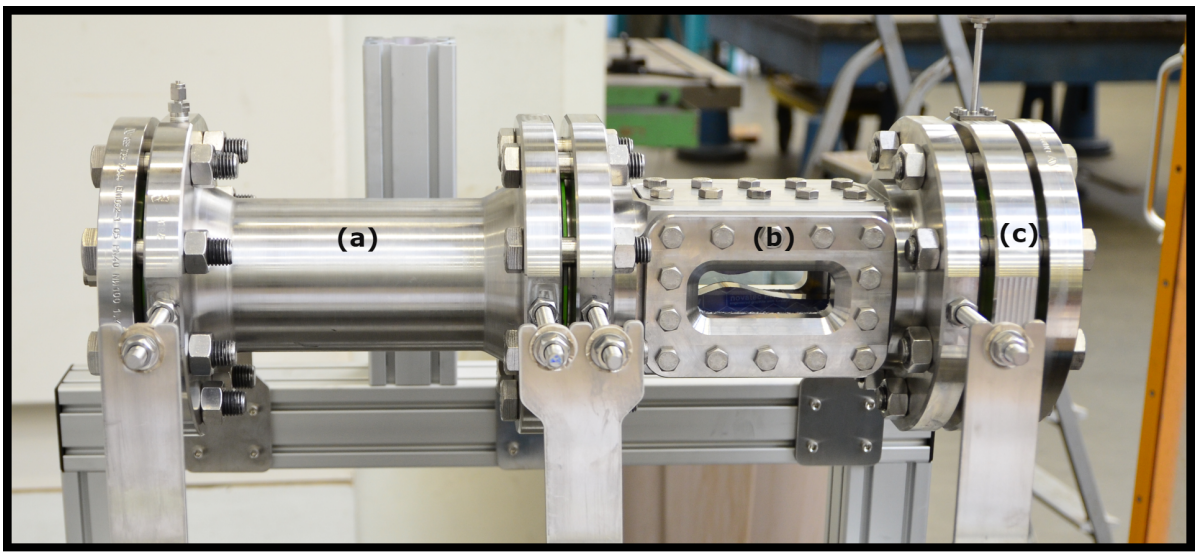

Figure 4.2: Modular nozzle housing containing **(a)** the settling chamber, **(b)** the nozzle test section with optical access and **(c)** the model support system upstream to the reservoir. Taken from [5].

The settling chamber dimensions are computed from the nozzle throat area and the choking mass flow rate. The design of the settling chamber is flexible to accommodate alternate nozzle designs with different mass flow rates. The SC also contains one set of honeycombs and two sets of screens for flow conditioning and is equipped with two sets of pressure measurement devices to calculate pressure drop across the length

of the settling chamber. The nozzle housing has the following modules: (i) the contraction channel, (ii) the converging-diverging nozzle, (iii) the model support compartment and (iv) the instrumentation. The contraction channel provides a transition from a circular to a rectangular cross section and increases mean flow speed. The C-D nozzle consists of two removable portions which form the top and bottom profiles. The shape of the nozzle profile is designed using the Method of Characteristics (MOC) [5, 45] with MM as the working fluid and inlet conditions of $T_0 = 252°C$ and $P_0 = 18.4$ bara and exit back pressure of 2.1 bara.

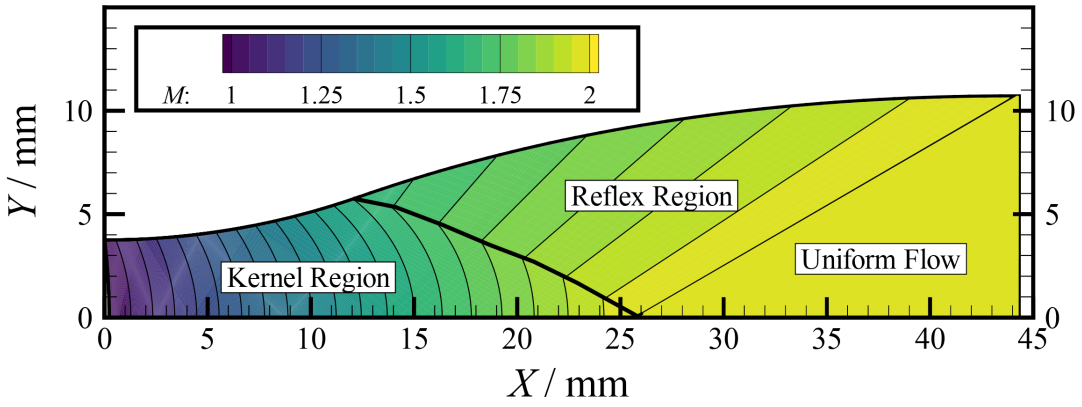

Figure 4.3: Upper half of the diverging section of the nozzle designed using MOC with Mach number contours plotted along the flow domain. Taken from [5].

Figure 4.3 shows half of the nozzle profile designed using an in-house code with fluid parameters estimated using the multi-parameter EoS [24]. The flow domain from the throat to the outlet can be divided into three regions namely, (i) the kernel region, (ii) the reflex region and (iii) the uniform flow region. The kernel region generates the expansion waves that accelerates the flow to the design Mach number. The reflex region is then responsible for deviating the flow to achieve uniform conditions at the outlet. [5] reports large density changes in the kernel region which is a characteristic of dense organic vapour expansions. Downstream of the uniform outflow region of the nozzle is the receiver, which is a low-pressure vessel that partially dissipates the high kinetic energy of the vapour at the outlet leading to a temperature increase. There is electrical tracing along the inlet pipe, nozzle housing, receiver and subsequent piping to the balance of plant to avoid vapour condensation. The nozzle is also equipped with the capability to insert a wedge into the flow at the nozzle exit to generate oblique shock waves. A mechanism to move the nozzle further into the reflex region of the flow will allow the validation of the shock angle prediction in the non-ideal regime. The proposed design of experiments with the wedge involves studying the shock wave behaviour with changing wedge angles.

In previous runs, the movement of the nozzle profile and characterisation of throat height was unknown. To characterise this movement, two crosses are engraved on the top and bottom profiles. It is possible to use end wall of the profiles as an identifier to characterise the movement. However, it was observed that the gaskets and profiles moved differently with respective to each other, hence crosses on the profile were selected as the best option. The first results from the ORCHID nozzle experiments [5] resulted in a Mach distribution that differed from simulations with both a vertical and horizontal offset (Refer Fig. 4.4a). These differences were more significant at the throat and it was hypothesised that this discrepancy could be a result of change in throat aperture due to the thermal elongation of the metals parts and thermal degradation of the gaskets. The design nozzle throat height is 7.5 mm. To quantify the effects of the nozzle profile movement, simulations were performed considering a vertical shift of ±0.5 mm and the results are plotted in Fig. 4.4b. The plot highlights the sensitivity of mid line Mach distribution with nozzle profile shifts, rendering the information on throat height changes valuable to proper experimental characterisation of the expansion. A profile shift of 0.5 mm upwards reduces the area ratio from 2.85 to 2.738. The flow after the throat is in the supersonic region where reduction in the area ratio translates to reduction in Mach number. The effect of profile shift can also be seen on choking mass flow at throat. At the design conditions, the mass flow rates at the throat are 1.0875 kg/s, 1.1651 kg/s and 1.2428 kg/s respectively for the 7 mm, 7.5 mm and 8 mm cases. The difference with the nominal throat case is ± 6.7%. It is also likely the first set of commissioning experiments reported by [5] were performed at a nozzle throat height of approximately 8 mm. Therefore, to accurately measure the throat, two crosses have been engraved on the top and bottom profiles of the nozzle with a known distance of 3 mm from the throat, as shown in Fig. 4.5. A calibration block with a speckled pattern of dots is used to convert the pixels

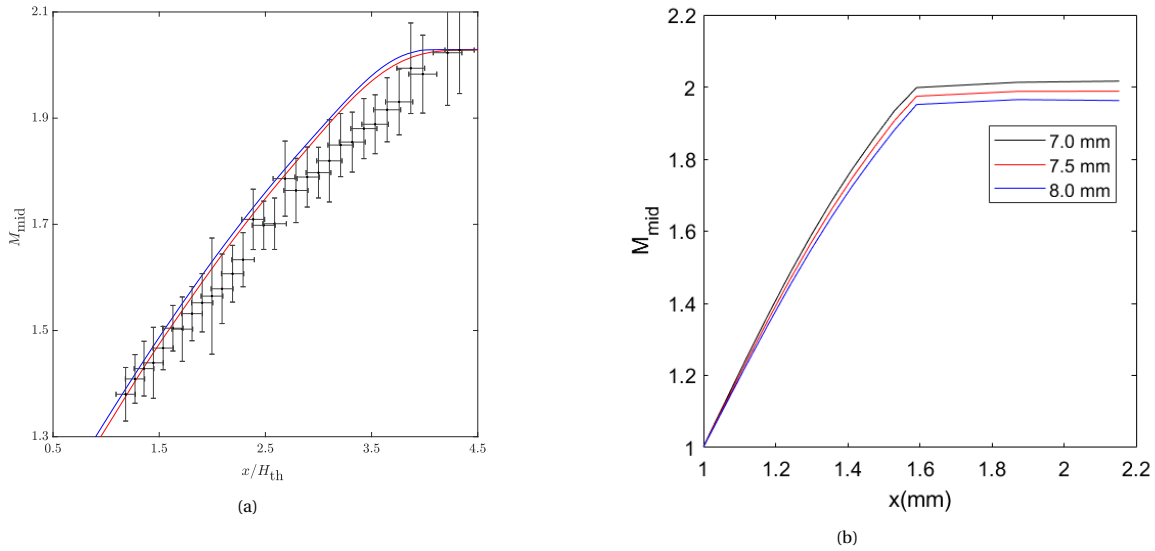

Figure 4.4: **(a)** Estimated Mach numbers from CFD simulations (- RANS, - Euler) with corresponding uncertainty bars along the midplane. Length of the nozzle has been non-dimensionalised with the throat height. Taken from [5]. **(b)** Effect of nozzle profile movement on Mach numbers along the midplane. Simulations are performed at design conditions of 18.4 bara, 525 K at the inlet and back pressure of 2.1 bara. x=1 indicates position of the nozzle throat.

into mm with the *DaVis* environment using the calibration feature. Detailed steps are described in App. B. Alternately, the measured mass flow rates can provide a qualitative understanding on nozzle profile shifts.

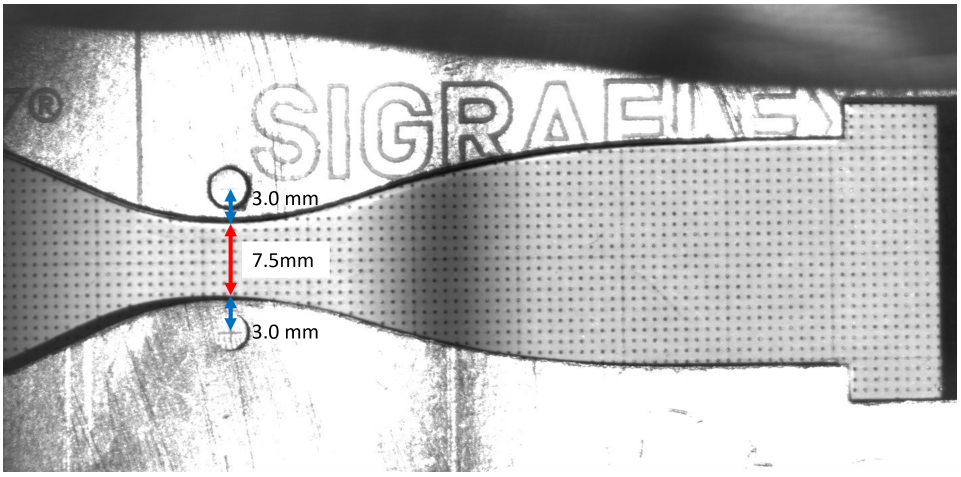

Figure 4.5: A dotted pattern block with markers of size 0.3 mm with 1 mm spacing is used for the calibration of images. The nominal throat height is 7.5 mm and the crosses are engraved at a distance of 3 mm from the profile wall. Measuring the distance of the crosses in the calibrated images provides the actual throat height.

4.1.3. Instrumentation & Data Acquisition System

The automatic collection of data from sensors, instruments and devices is called data acquisition [16]. The data acquisition and control (Data acquisition and Control (DAQC)) system receives information from the sensors, processes & conditions these signals and communicates back to the process using actuators. At the ORCHID, the supervisory control and data acquisition (SCADA) function is performed by *National Instruments compactRIO 9067*, an industrial grade real time capable controller with a processor and a field-programmable gate array (FPGA) with slots for seven I/O modules. The controller is connected via an Industrial Ethernet link to the SCADA PC (Intel(R) Xeon(R) CPU W-2223 @ 3.6 GHz Turbo and 32 Gb of RAM) running the Windows 10 operating system.The system runs the ORCHID COntrol and Data AcQuisition (CODAQ) human machine interface (HMI) program developed with the National Instruments LabVIEW 2016

software suite [5, Chapter 5].

The ORCHID is equipped with a variety of sensors for monitoring, the details of which are listed below:

- **Pressure instrumentation**
  The plant contains 5 *WIKA 232.50* analog Bourdon tube pressure indicators for visual monitoring, 1 *WIKA CPG 1500* precision digital pressure gauge and 10 *Wika UPT 20* pressure transmitters. The ranges are [0,16] barg, [-1,5] barg and [0-40] barg. The measured values, for all of them except the analogue indicators, are transmitted via a 4–20 mA signal to a 16-channel 24-bit A/D compactRIO input module (NI 9208). The measurement in the nozzle test section is carried out with a system of *Wika UPT 20* pressure transmitters and a *Scanivalve* DSA3218 pressure scanner. The combined pressure measurement system is used to estimate (i) the total pressure at the inlet and outlet of the nozzle housing and, (ii) the static pressure along the nozzle profile. Figure 4.6 shows the symmetric distribution of the *Scanivalve* pressure taps along the nozzle profile. A new *Wika UPT20* pressure sensor has been installed before the nozzle test section to provide accurate total pressure measurements for validation of flow through the nozzle.

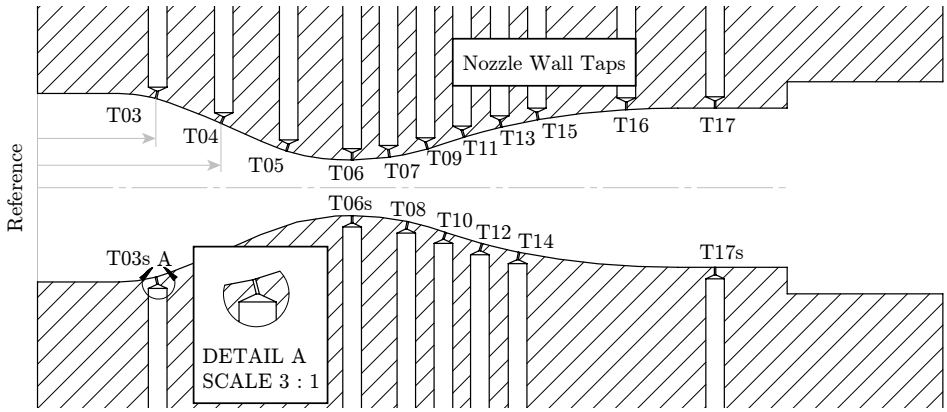

Figure 4.6: Location of the taps along the nozzle and position of the wedge. The inlet height is of 25.4 mm, the throat is 7.5mm and the outlet is 21.4mm high. Taken from [5].

- **Temperature instrumentation**
  The main process temperatures along the ORCHID are recorded by 14 *WIKA TR10* resistive thermometers (RTDs). RTD's measure the temperature by measuring the resistance of an electrical wire inside the sensor. The Nozzle test section is fitted with two *WIKA TR10-C* resistance temperature detectors (RTD) The first, TT015, is located in the second flange of the settling chamber and the other, TT014, is located at the receiver after the nozzle test section. These temperature transmitters measure within the range of 0–300 C, and their corresponding electrical output is a 4-20mA current signal. They are directly connected to a 24-bit A/D input module (NI 9208) of the *compactRIO* controller. Unlike the other RTD in the ORCHID balance of plant, these two sensors do not feature thermowells. Thermowells protect the sensor from flow induced pressure, vibrations or chemical effects from the process fluid, but lower the response time of the sensor.

- **Flowrate & Density instrumentation**
  The working fluid mass flow rate is measured using a *Krohne OPTIMASS 6400C* Coriolis mass flow meter, while the cooling loop volume flow rate is measured using a Blancett B2800 turbine flow meter. Both instruments provide 4–20 mA output signals which are connected to one of the two *compactRIO NI 9208* modules. A recent addition to the measurement infrastructure is the vapour mass flow meter, FT004 (*Krohne OPTIMASS 6000C*) before the test section. It is of Coriolis type and provides direct measurement of mass flow, density and temperature.

4.2. Schlieren Imaging

The nozzle test section is equipped with a glass wall for optical access to visualise the flow during start-up, steady state and shutdown. This not only provides qualitative insights into the flow field but also provide

information on Mach distribution that facilitates a quantitative comparison as well. This section begins with a discussion on fundamentals of schlieren imaging followed by the layout and instrumentation at the ORCHID.

4.2.1. Theoretical Background

Optical measurement techniques allow for non-intrusive investigation of the flow field and offer advantages in terms of spanning a field-of-view and providing instantaneous measurements [74]. When light passes through an inhomogenous media, it bends. The non-ideal compressible flow through the C-D nozzle is characterised by density gradients and this is exploited in methods such as shadowgraphy and schlieren techniques. Such methods are more relevant to the case of a dense vapour flow of complex organic molecules than air or simple molecules, because the change of refractive index and associated bending of light is several times larger allowing the capture of phenomena like Mach waves.

Light slows down on interacting with matter and this speed of light in a given medium, c with refractive index n is related to the speed of light in vacuum, c_o by,

$$n = \frac{c}{c_o} \tag{4.1}$$

Optical inhomogeneities refract the light in proportion to the gradient of the refractive index in the $x-y$ plane [42, 90] and the resulting ray curvature is given by,

$$\frac{\partial^2 x}{\partial z^2} = \frac{1}{n}\frac{\partial n}{\partial x} \quad ; \quad \frac{\partial^2 y}{\partial z^2} = \frac{1}{n}\frac{\partial n}{\partial y} \tag{4.2}$$

Integrating Eqn.4.2 gives the components of the angular ray deflection in the x and y directions as,

$$\epsilon_x = \frac{1}{n}\int \frac{\partial n}{\partial x}\partial z \quad ; \quad \epsilon_y = \frac{1}{n}\int \frac{\partial n}{\partial y}\partial z. \tag{4.3}$$

For two-dimensional schlieren of extent L along the optical axis, Eqn.4.3 becomes,

$$\epsilon_x = \frac{L}{n_0}\frac{\partial n}{\partial x} \quad ; \quad \epsilon_y = \frac{L}{n_0}\frac{\partial n}{\partial y} \tag{4.4}$$

where n_0 is the refractive index of the surrounding medium which is usually air. Since, the system is sensitive to refractive index changes associated with density gradients, a relation between the two is of interest. Mathematical models like the Lorentz-Lorentz relation [62, 65] expresses the refractivity index of the medium in terms of molecular constants, the properties of the fluid and the molecular polarisability. A simplification of this equation is the empirical Gladstone-Dale relation [69], often used for air and simpler molecules. It is given by the linear relation,

$$n = 1 + K\rho \tag{4.5}$$

where K is the Gladstone-Dale constant which is determined experimentally. K for organic fluids such as MM siloxane has not been documented in literature. Hence, a novel theoretical approach proposed by Head [5] is used to calculate the same. A brief discussion on the approach is presented here. The Lorentz-Lorentz relation is inverted resulting in Eqn.4.6 that correlates the refractive index of the medium as a function of density, molar refractivity and molar mass.

$$n = \sqrt{\frac{1 + 2A\cdot\rho/M}{1 - A\cdot\rho/M}} \tag{4.6}$$

Table 4.3: Molar refractivity values for air and two representative organic fluids.

Fluid	**Molar refractivity, A (cm^3/mol)**	**Reference**
Air	6.66	[69]
MM	48.92	[5]
D4	74.56	[107]

Molar refractivity A is usually estimated experimentally, but data is not available for all molecules. Hence using the concept of 'additivity of bond refractions' [107], A can be evaluated as sum of contributions from individual atomic bonds. Thus for complex molecules with larger number of atomic bonds, the molar refractivity is substantially larger than that of mixtures of simple molecules like air. Refer to Tab. 4.3 for a comparison of molar refractivity for air, MM and D_4. Figure 4.7 depicts the change of refratve index with normalised density ranges typical of a supersonic expansion. The gradient of the refractive index for complex organic molecules (indicated by the lines in red and green) can be exploited for visual inspection with lower optical sensitivity.

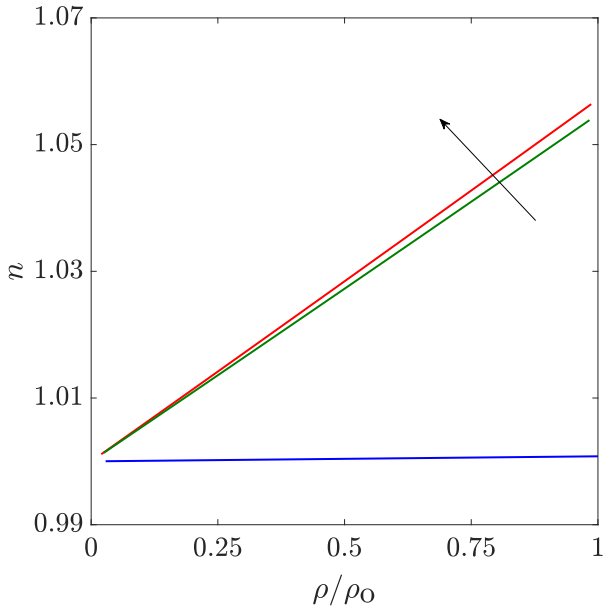

Figure 4.7: The refractive index n vs. normalised density $\frac{\rho}{\rho_o}$ for air (-), MM (-) and D_4 (-). Taken from [5].

4.2.2. Measurement chain

Once the optical properties of the fluid medium are characterised, the next component of the optical investigation setup is the configuration and specifications of the instrumentation. Considering the spatial constraints, a z-type layout is adopted and is schematically shown in Fig. 4.8. All the hardware elements, e.g., light source, lens, pinhole, mirrors and camera are mounted on three separate rigid structures. The light source for the measurement chain is provided by a *cold white* mounted LED from *Thorlabs (Model: MCWHLP1)* with driver *(Model: LEDD1B)* which provides continuous uncollimated light with a typical output power of 2350 mW if driven at a current of 700 mA. During the experimental run, the LED intensity is kept at maximum. The light from the LED then passes through a lens and is focussed onto the pinhole set at 2 mm. The pinhole has a minimum aperture of 0.2 mm and can be adjusted to increase optical sensitivity. This section of the measurement chain is located outside the ventilation hood (See Fig. 4.9).

The light beam from the pinhole which is placed at the focus of lens B is redirected to the test section by mirror A. Both mirrors A and B are flat with a surface accuracy of 4-6 λ with enhanced aluminium coating. The dimensions of both flat mirrors are 127x178 mm (LxH) and are based on the minimum dimensions of the nozzle and part of the testing channel. These two flat mirrors are used to finely adjust the direction of the light beam towards lens C . The light from lens C is refocused to form an inverted image of the source at the knife edge. The inverted image is then projected onto the charge-coupled device (CCD) sensor of the digital camera by means of an independent standing lens or a Nikon camera (referred to as schlieren camera) lens. An additional LED light source and camera is placed beside mirror B facing the front portion of the test section to capture the change in nozzle profile. This camera will be referred to as the geometry camera. Both the schlieren and geometry camera are a *BOBCAT IGV-B1610* equipped with a single 16-bit CCD. Its image resolution is 1628 x 1236 pixels delivering a maximum frame rate of up to 25 frames per second. The pixel size is 4.4 μm and it has a shutter speed/exposure time ranging between 5 μs and 59 ms. Lens A has a focal length of 105 mm and lens B has a focal length of 180 mm.

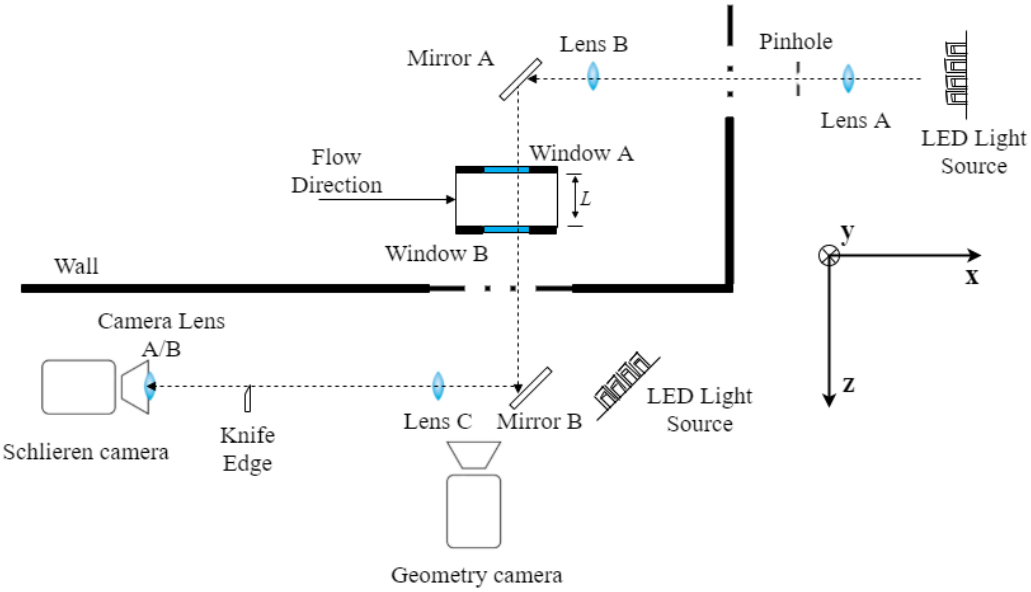

Figure 4.8: Birds-eye schematic view of the schlieren lay-out used for visualising the flow in the ORCHID nozzle test section: a simple lens-type setup with two flat mirrors. Adapted from [5].

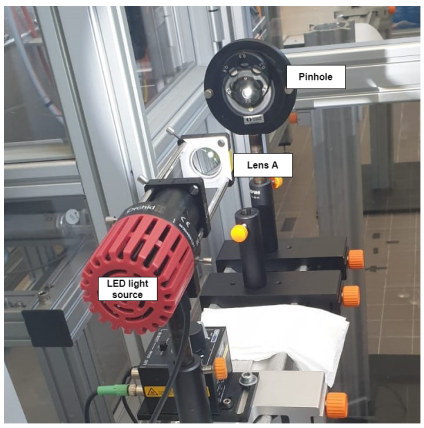

(a)

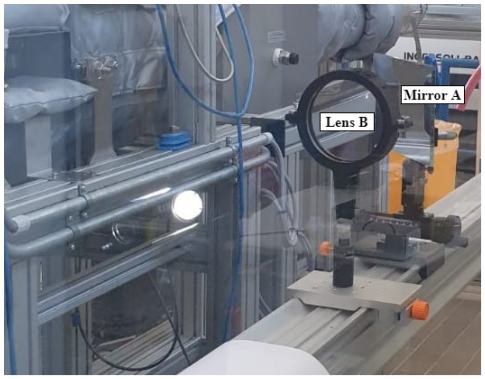

(b)

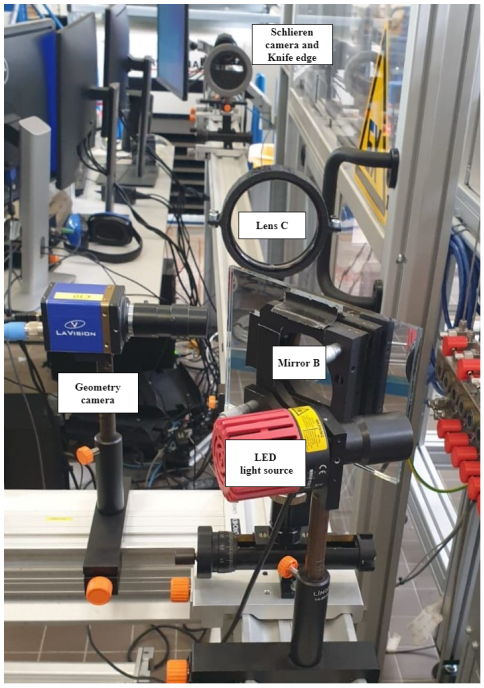

(c)

Figure 4.9: Photographs of the z-type schlieren measurement chain. **(a)** Pinhole & LED light source, **(b)** Lens & mirror setup inside the ventilation cabin, **(c)** Geometry & schlieren camera with accompanying lens and mirror.

4.3. Operating Conditions

An experimental test matrix has been developed (Refer Tab. 4.4) with various inlet and outlet pressures with constant pressure ratio of 8.76. The compressibility factor which reflects the degree of non-ideality is also specified for the inlet and outlet conditions. The test conditions are proposed keeping in mind the operational limits of the ORCHID. The working limits of the ORCHID are constrained by the thermal stability of the working fluid & thermal oil, requirements imposed by the ATEX 137 directive and budgetary limitations. The isentropes of the different test cases are depicted on a $T-s$ diagram in Fig. 4.10. Only cases A and B were conducted at the time of writing the thesis and these results will be reported.

Table 4.4: Operating conditions for various isentropes with constant pressure ratio of 8.76.

Isentrope	Inlet Conditions			Outlet Conditions		
	T/°C	P/ bara	Z	P/ bara	M exit	Z
A	252	2.73	0.9576	0.3116	2	0.9941
B	252	6	0.901	0.6848	2	0.9866
C	252	12	0.7733	1.3696	2	0.9715
D	252	18.4	0.5582	2.1	2	0.9511

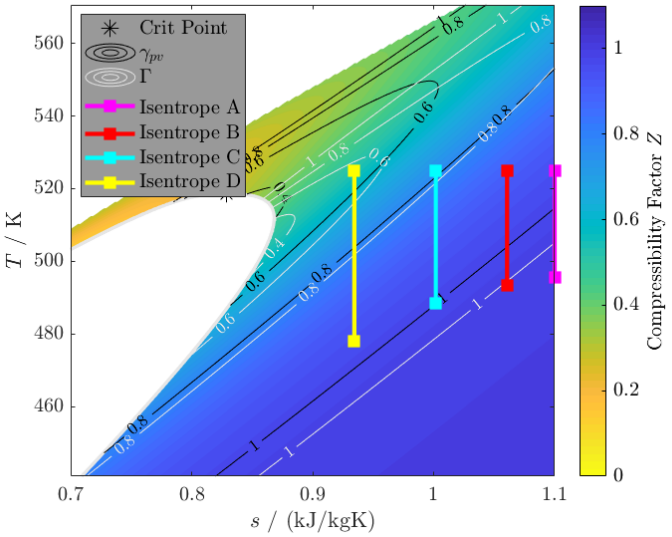

Figure 4.10: T-s diagram of MM siloxane with contours of compressibility factor, Z. The planned isentrope cases summarised in Tab. 4.4 are plotted.

4.4. Experimental Procedure

The gradual startup of the ORCHID is done according to the steps outlined in A.J.Head [5, Chapter 5]. They are briefly discussed in this section. Before the facility can be operated, the fluid tightness of the working fluid loop is verified by leakage tests. A vacuum pump is used to remove the incondensable gases from the WF loop until a pressure close to the vapour pressure of MM is reached. After the vacuum pump is turned off, the pressure rise is recorded. Any anomaly in the pressure rise trend is a red flag for leaks and is followed by a helium leak detection procedure. For the experiments reported in this thesis, a helium leakage protocol was not necessary. Once the leak tightness if verified, the start-up consisting of sequential activation of the ATEX ventilation, aircoolers, cooling loop pump, booster and main pump. Once the components have reached their set point, the start-up continues with heating of the working fluid by controlling control valves of the heating loop to allow part of the thermal oil flow into the primary heat exchanger. The temperature of the thermal oil is then gradually ramped to avoid any thermal stresses in the heat exchanger. This is set at 3°C for the evaporator side and 1°C for the condenser side. The start-up ends with the control of TT005 at the set point of 252°C. A settling period of around 20 minutes (given that the tracing was switched on and the TS was

already sufficiently hot) was needed after stabilisation of operating conditions before opening the main valve (MOV002a) to redirect dense vapour into the test section. Once MOV002a is fully opened and the temperature has stabilised, the back pressure (PT004) is controlled by PICA002. Once steady conditions are achieved and no condensation is visible, schlieren flow images were recorded. Once image acquisitions were complete for Isobar A, the evaporator pressure and back pressure were controlled for the required values while maintaining TT005 at 252°C. After a stabilisation period of 20 minutes, the procedure for flow acquisitions was repeated. Once the experiment concluded, a two-step procedure was followed for the shut-down. First the controllers FICA001 and PICA002 are deactivated allowing higher mass flow rates in the heat exchanger to fasten the cooling process. This is then followed by initiating the automated shutdown procedure. After an appropriate time lag, the cooling pump and air- coolers will also be turned off.

4.5. Results

Once the ORCHID is gradually started up and the target operating conditions are achieved, a stabilisation period of about 20 minutes is required. The pressure data acquisition and schlieren imaging can be done simultaneously, although in the experimental run reported in this thesis the *Scanivalve* system was out of operation. At the time of performing the experiments, synchronous control of both the geometry and schlieren camera was not available and they were done in immediate succession. The geometry images are converted from pixels to mm in the *DaVis* environment and the schlieren images are post processed to extract Mach lines at the throat using an in-house code. The first step to reporting the experimental data is the systematic procedure for steady state identification which is discusssed in Sec. 4.5.1. Following steady state identification, the Type A and Type B uncertainties are quantified for appropriate validation with simulation results.

4.5.1. Steady State Identification

Evaluation of the steadiness of the results is of crucial importance to the validation procedure since the simulations are done under the assumption of steady state. There are multiple methods reported in literature to identify steady state from experimental data [10, 11, 15]. They typically rely on identifying a period of steady state from an analysis of statistical quantities like mean and standard deviation and extracting corresponding data from that period. For the steady state estimation of the ORCHID, Head [5] had employed a combination of the heurestical method prescribed in [63], which was also adopted by Woodland *et al.* [108]. The detailed procedure for the steady state estimation is described below :

Table 4.5: Criteria for steady state identification. Adapted from [108].

Measurement	**Steady state criteria**
Temperature	Difference < 1.0 K
Pressure	Change < 2%
Mass flow	Change < 2%

- a dataset is visually inspected to qualitatively identify periods of steady state for each of the process variables representative of the intended experiment.

- the average value of each process variable of interest obtained from the first 30 and the last 30 samples within the identified period is computed. If they satisfy the steady state criteria proposed by Woodland *et al.* [108], then the process can be considered steady. Table 4.5 provides the comparison criteria for each measurement.

- to verify whether the steady state period has sufficient number of data points, a statistical convergence test is performed as outlined in International Organization for Standardization (ISO) [53]. Statistical convergence is achieved if the mean and standard deviation of the measured quantities remain approximately constant as the number of samples within the time period increases.

- to identify other steady periods of time following the initial qualitative estimation, a statistical test is defined using the average and associated standard deviation of the process variables for this interval, *i.e,* if a sample falls within the range of steady state mean plus (or minus) 3 times the standard deviation, the sample falls under the steady state time window.

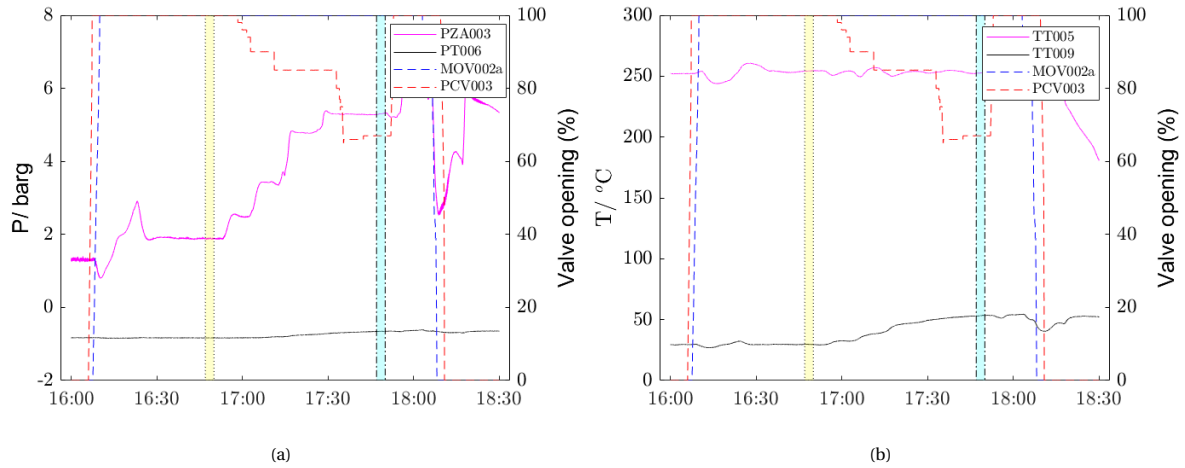

Figure 4.11: Recording of process variables associated with evaporator and condenser where the coloured areas, A (•) and B(•) correspond to two different operating conditions.The percentage aperture of the nozzle inlet valve MOV002a (–) and primary control valve, PCV003 (–) can be read on the right axes. **(a)** Evaporator pressure, PZA003 and condenser pressure, PT006 can be read on the left axis. **(b)** Evaporator temperature, TT005 and condenser temperature, TT009 can be read on the left axis.

For the ORCHID, a hard requirement of steady state criteria is imposed on the following process variables: (i) evaporation temperature (TT005) and pressure (PZA003), (ii) nozzle test section back pressure (PT004), (iii) condensation pressure (PT006), (iv) nozzle test section inlet pressure (PT011) and, (iv) working fluid mass flow rate (FT001). Additionally, to avoid that the steady state assessment is the result of a faulty measurement affected by gross error, also TT015 (settling chamber temperature of the nozzle TS), TT014 (receiver temperature), TT009 (condensation temperature) and PT005 (inlet pressure of the condensor) are tested for steadiness.

Figures 4.11, 4.12 and 4.13 show the recordings of relevant process variables over the time period in which the process run was conducted. Recordings in the time period from 16:00:00 till 18:30:00 (43,201 data points) are considered for the analysis . Within this period, operating conditions for isentropes A and B from Tab. 4.4 were reached. The periods in which MM was flowing through the nozzle can be deduced by the opening of the two valves MOV002a and PCV003, indicated on the right axis of Fig. 4.11 and 4.12. The highlighted regions in the figures correspond to the period in which schlieren images were taken after the values of the evaporation pressure (PZA003), the total inlet pressure PSV001, temperature (TT015) and mass flow (FT001) were sufficiently steady [1]. Period A extends from 16:47:00 to 16:50:00 while period B extends from 17:47:00 to 17:50:00. Both the periods contain 180 data points. A settling time of around 20 minutes was sufficient to start the test run. Figure 4.11 reports the maximum and minimum cycle pressure and temperature (at the evaporator and condenser respectively).

Figure 4.12 reports the test section inlet and outlet process variables while Fig. 4.13 reports the flowrate of MM (in liquid and vapour) and the associated density measurements. In the commissioning experiments elaborated in [5], a pressure loss of around 0.7 bar is considered from the evaporator to the inlet of the nozzle test section. This was an estimate and was not verified. With the added pressure measurement PT011, at the inlet of the TS the actual pressure drop across the lines and valves from the evaporator to the nozzle inlet can be computed. For isentrope A, the pressure loss is around 0.173 barg while for isentrope B it is 0.3208 barg. In the short period following isentrope B, when evaporator side pressure was 8 barg, the pressure loss is around 0.43 barg. The increasing pressure loss is expected given the higher mass flow rates for higher inlet pressure isentropes. Drawing a linear relation between the experimentally reported pressure losses, at design conditions of 18.4 bara, the pressure loss could be around 0.85 barg. The assumed pressure loss of 0.7 barg in [5], could be a possible reason for the differences in experimental and simulation results.

For steady state evaluation, the period from 16:41:00 to 16:51:00 for Isentrope A (and 17:41:00 to 17:51:00 for Isentrope B) were initially evaluated, given that a 10 minutes interval was stipulated by Woodland *et al.* [108]. However the criteria were not met (specifically for temperature) and the steady state time period was clipped to 16:46:00 to 16:51:00 and the temperature threshold was increased to 1.0 K from 0.5 K. This is acceptable since the duration of schlieren acquisitions still falls into this time bracket. The 30 sample averages

[1] Note that the recordings of pressure are reported in barg while the test matrix is constructed with bara units.

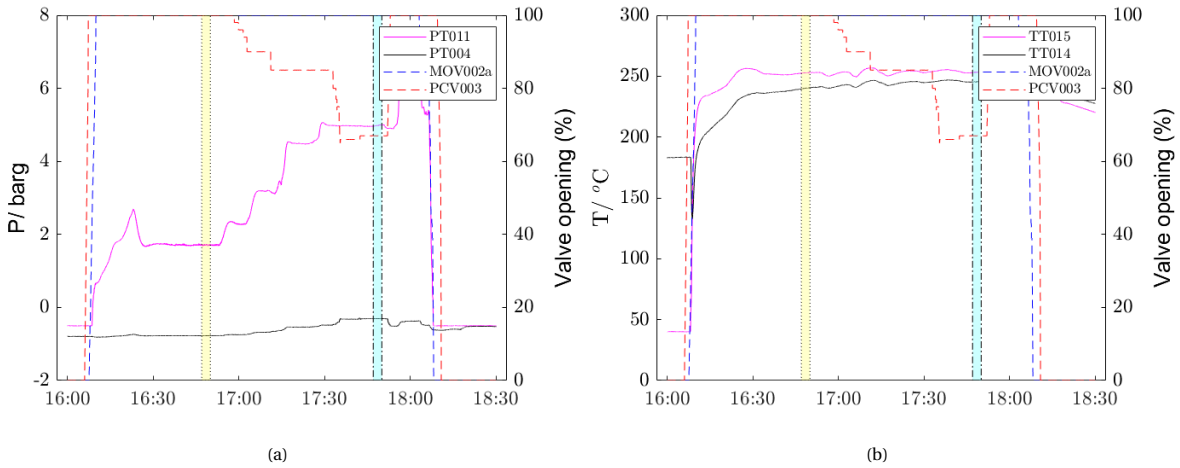

(a) (b)

Figure 4.12: Recording of process variables associated with inlet and outlet of nozzle test section where the coloured areas, A (•) and B(•) correspond to two different operating conditions.The percentage aperture of the nozzle inlet valve MOV002a (–) and primary control valve, PCV003 (–) can be read on the right axes. **(a)** Inlet total pressure, PT011 and receiver pressure, PT004 can be read on the left axis. **(b)** Inlet total temperature, TT015 and receiver temperature, TT014 can be read on the left axis.

at the start and end of the steady state period and the changes are reported in Tab. 4.6. The chosen period satisfies the steady state criteria and a statistical analysis on the process variables during this time period will yield the Type A uncertainties.

Table 4.6: Average of 30 values sampled at the start and end of the steady state period. The differences of the averages satisfy the Woodland criteria stated in Tab. 4.5.

	Isentrope A			Isentrope B		
	16:46:00	16:51:00	Δ	17:46:00	17:51:00	Δ
TT005 / °C	253.93	254.46	0.54 °C	252.14	252.94	0.80 °C
TT009 / °C	29.60	29.36	0.24 °C	52.90	53.59	0.69 °C
TT015 / °C	252.24	252.98	0.74 °C	252.76	253.62	0.87 °C
TT014 / °C	239.37	240.86	1.49 °C	245.16	245.68	0.52 °C
PZA003 / barg	1.90	1.88	1.09%	5.28	5.26	0.35%
PT006 / barg	-0.83	-0.83	0.07%	-0.66	-0.65	1.71%
PT011 / barg	1.72	1.70	1.10%	4.96	4.94	0.37%
PT004 / barg	-0.77	-0.77	0.14%	-0.31	-0.31	0.29%
FT001 / kg/hr	601.11	600.50	0.10%	1348.70	1346.10	0.19%

4.5.2. Experimental Uncertainty Quantification

According to the International Organisation for Standardisation (ISO) [53], the uncertainty associated with measurements can be classified into *Type A* and *Type B* depending on the method of numerical estimation. Type A uncertainties are evaluated by statistical analysis of series of observations and is the standard deviation of the measurements. Type A uncertainties include random errors associated with uncontrolled fluctuations or disturbances. They are unpredictable and non-reproducible. On the other hand, Type B uncertainties are those that are not deduced by a statistical analysis of observations. Instead, they are based on scientific knowledge, technical datasheets or previous measurement data. Measurement uncertainties have been quantified using standard methods outlined by Moffat [70] and Abernathy *et al.*[3]. They are detailed below:

- The standard uncertainty, u is the estimated standard deviation of a measurement or an error source in the measurement chain.

- The expanded uncertainty, U is the uncertainty associated with a measurement or an error source with the desired level of confidence and is given by $U = k.u$. If the distribution associated to the standard

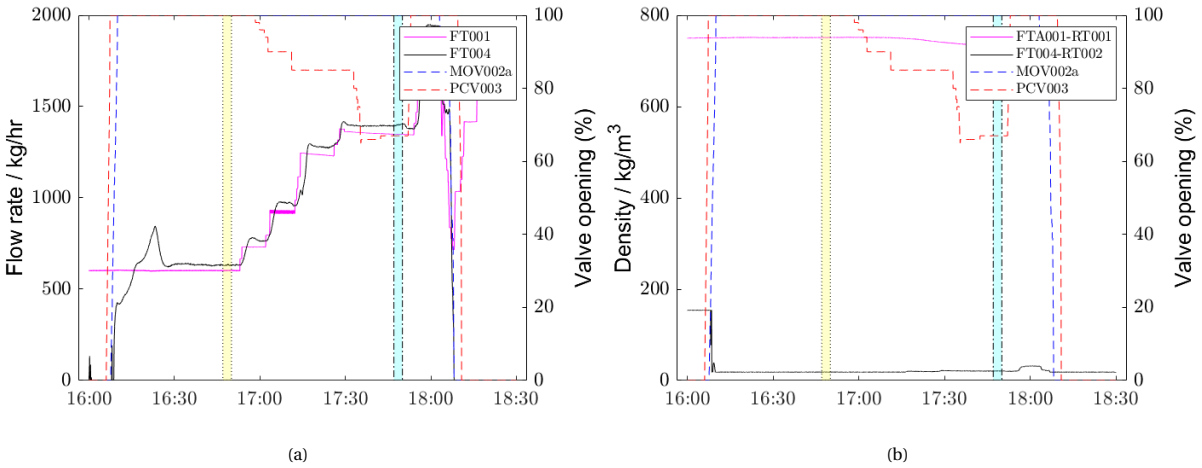

Figure 4.13: Recording of process variables associated with flowmeter measurements where the coloured areas, A (•) and B(•) correspond to two different operating conditions.The percentage aperture of the nozzle inlet valve MOV002a (–) and primary control valve, PCV003 (–) can be read on the right axes. **(a)** Liquid MM mass flow rate, FT001 and vapour MM mass flow rate, FT004 can be read on the left axis **(b)** Liquid density, FTA001-RT001 and vapour density, FT004-RT002 can be read on the left axis.

uncertainty is normal, k is in the range 2-3, where 2 defines an interval with a level of confidence of 95 %, while 3 defines an interval with a level confidence greater than 99 %.

- The combined uncertainty is calculated by propagating individual measurement uncertainties through the measurement chain. This is relevant if the measurement is affected by multiple error sources.

Type A Uncertainties

In order to calculate the Type A uncertainties, the second order moments of the process variables are determined and a coverage factor of 2 is applied which results in an expanded uncertainty, U with 95% confidence interval. Table 4.7 reports the means and expanded Type A uncertainties for isentropes A and B over the steady state period identified in Sec. 4.5.1 for selected process variables. Type A uncertainties of all other process variables can be read from App. C.

Table 4.7: Experimental mean values and related Type A uncertainties for isentropes A and B. A coverage factor of 2 is used to compute the expanded uncertainty. Steady state periods for isentrope A extends from 16:47:00 to 16:50:00 while isentrope B extends from 17:47:00 to 17:50:00 and both the periods contain 180 data points.

		Isentrope A		Isentrope B	
Process variable	**Tag**	**Mean Value**	$U_{Type\,A}$	**Mean Value**	$U_{Type\,A}$
Nozzle inlet temp.	TT015 / °C	252.72	±0.27	253.22	±0.29
Receiver temp.	TT014 / °C	240.04	±0.61	245.50	±0.16
Settling chamber pressure	PT011 / barg	1.71	±0.02	4.98	±0.03
Receiver pressure	PT004 / barg	-0.77	±0.00	-0.31	±0.00
Evaporator temp.	TT005 / °C	254.32	±0.21	252.57	±0.29
Condenser temp.	TT009 / °C	29.72	±0.19	53.28	±0.38
Evaporator pressure	PZA003 / barg	1.88	±0.02	5.30	±0.03
Condenser pressure	PT006 / barg	-0.83	±0.00	-0.65	±0.00
MM liquid mass flow rate	FT001 / kg/h	601.08	±3.90	1347.48	±1.18
MM vapour mass flow rate	FT004 / kg/h	630.53	±4.95	1398.89	±6.93
MM liquid density	FTA001-RT001 / kg/m^3	751.34	±0.06	732.62	±0.06
MM vapour density	FT004-RT002 / kg/m^3	18.37	±0.02	20.70	±0.02
MM liquid temp.	FTA001-TT017 / °C	32.33	±0.03	50.17	±0.43
MM vapour temp.	FT004-TT016 / °C	248.27	±0.42	251.08	±0.29

Type B Uncertainties
Type B uncertainties are associated with the measurement instruments and the A/D conversion, which includes signal conditioning. It is calculated as,

$$U_{\text{Type B}} = \sqrt{U_{\text{instrument}}^2 + U_{\text{A/D}}^2} \tag{4.7}$$

where $U_{\text{instrument}}$ is the expanded systemic uncertainty of the sensor and $U_{\text{A/D}}$ is the expanded uncertainty associated with the analog-digital converter and related signal conditioning. The details of the relevant instrument's full scale range and factory certified accuracy with coverage factor of 2 is reported in Tab. 4.8.

For the temperature instrumentation, the accuracy is Class A or higher according to the EN 60751 standard. Their instrument uncertainties are negligible and calculated as ± 0.1+0.0017|T| $^\circ C$ for Class AA and ± 0.15+0.002|T| $^\circ C$ for Class A. The RTD's TT015, TT014, TT005 and TT009 are Class A and the corresponding instrument uncertainties are calculated accordingly.

Table 4.8: Instrument uncertainties of selected process sensors in the ORCHID.

Process variable	**Tag**	**FS Measuring range**	$\boldsymbol{U}_{\textbf{instrument}}$
Nozzle inlet temp.	TT015 / $^\circ C$	0-300	Class A
Receiver temp.	TT014 / $^\circ C$	0-300	Class A
Settling chamber pressure	PT011 / barg	0-40	0.1%
Receiver pressure	PT004 / barg	-1-5	0.1%
Evaporator temp.	TT005 / $^\circ C$	0-350	Class A
Condenser temp.	TT009 / $^\circ C$	0-300	Class A
Evaporator pressure	PZA003 / barg	0-40	0.1%
Condenser pressure	PT006 / barg	-1-5	0.1%
MM liquid mass flow rate	FT001 / kg/h	420-5580	0.1%
MM vapour mass flow rate	FT004 / kg/s	0.17-1.25	*
MM liquid density	FTA001-RT001 / kg/m^3	100-3000	±1
MM vapour density	FT004-RT002 / kg/m^3	60-150	±1***
MM liquid temp.	FTA001-TT017 / $^\circ C$	-50-400	**
MM vapour temp.	FT004-TT016 / $^\circ C$	-50-400	**

*Instrument uncertainty calculated based on a calibration process with accuracy (%) given by $0.334x^2 - 0.6743x + 0.7251$, where x is the mass flow rate in kg/s for operational density of 140 kg/m^3. The accuracy (%) is given by $0.381x^{-0.376}$ for density range of 60 kg/m^3.Details can be found in the Manufacturing Sizing Datasheet (2021) Krohne Optimass 6000 which was sized for MM at a nominal flowrate of 1.25 kg/s and then checked for a flowrate of 0.17 kg/s.
**Instrument uncertainty given by $\pm 0.5 \pm 0.5\%|T|^\circ$C.
***Assumed to be same as liquid density uncertainty, due to lack of information from supplier. Actual uncertainty needs to be verified.

The A/D converter suffers from the following non-idealities: (1) offset error, (2) gain error, (3) input noise and (4) integral non-linearity. Once the combined standard uncertainty, $u_{A/D}$ is determined, $U_{A/D}$ is calculated assuming a confidence level of 95%. The combined standard uncertainty is taking the residual sum of squares (RSS) of the maximum values of all individual standard uncertainties assuming zero correlation. Given that the integral non-linearity and noise terms are minimal, the combined standard uncertainty due to the A/D converter is,

$$u_{\text{A/D}} = \sqrt{u_{\text{gain}}^2 + u_{\text{offset}}^2} \tag{4.8}$$

where u_{gain} is the gain error uncertainty and u_{offset} is the offset error uncertainty. For normal environmental temperatures like those of the laboratory hall and inside the control cabinet where the signal conditioning and A/D conversion modules are located, the departure from the nominal value of the gain is commonly called gain error uncertainty and is specified as,

$$u_{\text{gain}} = \frac{\delta_{\text{gain}} \cdot X}{100} \tag{4.9}$$

where δ_{gain} is the gain uncertainty in percentage of the full scale value and X is the measured value. Similarly, the offset component of the A/D conversion uncertainty is defined as,

$$u_{\text{offset}} = \frac{\delta_{\text{offset}} \cdot R}{100} \tag{4.10}$$

where δ_{offset} is the offset uncertainty in percentage of the full scale value and R is the range *i.e*, the reading span for which the device is configured. Currently, $\delta_{\text{gain}} = 0.76$ and $\delta_{\text{offset}} = 0.04$ are used to calculate the A/D uncertainty. A more standardised quantification of the gain and offset error has been undertaken along the guidelines stipulated in the NI9208 calibration technical document [1]. Equations 4.11 to 4.14 provide the fitted equations for the transfer functions. The reported gain and offset errors (See Tab. 4.9) are not symmetric due to lack of enough statistical data to quantify the gradient of the transfer function. This can be rectified by taking more samples during the calibration process.

$$\delta_{\text{gain,+}} = 0.18 \tag{4.11}$$

$$\delta_{\text{gain,-}} = -0.06 \tag{4.12}$$

$$\delta_{\text{offset,+}} = 0.0005 \cdot i^2 - 0.0178 \cdot i + 0.1766 \tag{4.13}$$

$$\delta_{\text{offset,-}} = -0.0011 \cdot i^2 + 0.0379 \cdot i - 0.3758 \tag{4.14}$$

where i is the DAQ reading in mA. Table 4.9 and 4.10 reports the upper and lower gain and offset uncertainties associated with the process variables. For a comparison, for TT015 the gain uncertainty is 0.76 with the older approach while the new calibration yields an uncertainty of 0.45. Hence, the gain and offset uncertainties derived from the more rigorous calibration procedure yields more realistic, conservative values.

Table 4.9: Upper and Lower bounds of the gain uncertainties computed for Isentrope A. The period extends from 16:47:00 to 16:50:00 and contains 180 data points.

		Isentrope A		
Process variable	**Tag**	**Mean Value**	$U_{Gain,-}$	$U_{Gain,+}$
Nozzle inlet temp.	TT015 / °C	252.72	-0.15	0.455
Receiver temp.	TT014 / °C	240.04	-0.144	0.432
Settling chamber pressure	PT011 / barg	1.71	-0.001	0.003
Receiver pressure	PT004 / barg	-0.77	0.000	-0.001
Evaporator temp.	TT005 / °C	254.32	-0.153	0.458
Condenser temp.	TT009 / °C	29.72	-0.018	0.053
Evaporator pressure	PZA003 / barg	1.88	-0.001	0.003
Condenser pressure	PT006 / barg	-0.83	0.000	-0.001
MM liquid mass flow rate	FT001 / kg/h	601.08	-0.361	1.082
MM vapour mass flow rate	FT004 / kg/h	630.53	-0.378	1.135
MM liquid density	FTA001-RT001 / kg/m^3	751.34	-0.451	1.352
MM vapour density	FT004-RT002 / kg/m^3	18.37	-0.011	0.033
MM liquid temp.	FTA001-TT017 / °C	32.33	-0.019	0.058
MM vapour temp.	FT004-TT016 / °C	248.27	-0.149	0.447

Expanded Uncertainties
The total expanded uncertainty is calculated as,

$$U = \sqrt{U_{\text{TypeB}}^2 + U_{\text{TypeA}}^2} \tag{4.15}$$

The computed total expanded uncertainties for selected process variables are reported in Tab. 4.11.

Before the start of the experiment for various isentropes, the calibration is first performed using the calibration block and in-built *DaVis* functionalities as detailed in App. B. The calibration image is also used in the image pre-processing stage in order to remove background noise from the image sequence. In addition, this image is used to identify the nozzle walls and thus the location of the throat. Once MOV002a is open, the schlieren acquisitions can begin. For accurate flow imaging, it is important to ensure alignment of the camera, lens, mirrors are stable. The knife edge can be moved vertically to adjust the brightness in the throat region. It was observed that schlieren camera produced typical flow field images even when the knife edge was completely removed. The acquisitions for each isentrope were performed at 25 Hz for a duration of 3 minutes. The flow field was not zoomed into the throat region since the purpose of the experiment was also

Table 4.10: Upper and Lower bounds of the offset uncertainties computed for Isentrope A. The period extends from 16:47:00 to 16:50:00 and contains 180 data points.

		Isentrope A		
Process variable	**Tag**	**Mean Value**	$U_{Offset,-}$	$U_{Offset,+}$
Nozzle inlet temp.	TT015 / °C	252.72	-0.027	0.010
Receiver temp.	TT014 / °C	240.04	-0.026	0.010
Settling chamber pressure	PT011 / barg	1.71	-0.001	0.000
Receiver pressure	PT004 / barg	-0.77	0.001	0.000
Evaporator temp.	TT005 / °C	254.32	-0.029	0.011
Condenser temp.	TT009 / °C	29.72	-0.013	0.006
Evaporator pressure	PZA003 / barg	1.88	-0.001	0.000
Condenser pressure	PT006 / barg	-0.83	0.001	0.000
MM liquid mass flow rate	FT001 / kg/h	601.08	-0.253	0.118
MM vapour mass flow rate	FT004 / kg/h	630.53	-0.241	0.112
MM liquid density	FTA001-RT001 / kg/m^3	751.34	-0.232	0.107
MM vapour density	FT004-RT002 / kg/m^3	18.37	-0.006	0.003
MM liquid temp.	FTA001-TT017 / °C	32.33	-0.015	0.007
MM vapour temp.	FT004-TT016 / °C	248.27	-0.039	0.017

to study the formation of oblique shock waves generated by a 2.5° wedge at the exit of the nozzle. Figure 4.14 shows the recordings of the flow field taken during start-up, Isentrope A, Isentrope B and shut-down. The schlieren images captured during the two isentropes can be further post-processed to extract information regarding the Mach field along the centre plane of the nozzle and to estimate the angle of the oblique shock wave generated by the wedge. For the former, automated post-processing tools are available while for the latter manual extraction of the shock angles is performed. Using the geometry camera and calibration, the throat heights were measured and reported in Tab. 4.12.

Table 4.11: Total expanded uncertainties for operating conditions associated with isentropes A and B. A coverage factor of 2 is used to compute the expanded uncertainty. Steady state periods for isentrope A extends from 16:47:00 to 16:50:00 while isentrope B extends from 17:47:00 to 17:50:00 and both the periods contain 180 data points.

		Isentrope A		Isentrope B	
Process variable	**Tag**	**Mean Value**	U_{total}	**Mean Value**	U_{total}
Nozzle inlet temp.	TT015 / °C	252.72	±2.051	253.22	±2.058
Receiver temp.	TT014 / °C	240.04	±2.027	245.50	±1.983
Settling chamber pressure	PT011 / barg	1.71	±0.0271	4.98	±0.0464
Receiver pressure	PT004 / barg	-0.77	±0.007	-0.31	±0.0043
Evaporator temp.	TT005 / °C	254.32	±2.057	252.57	±2.054
Condenser temp.	TT009 / °C	29.72	±0.366	53.28	± 0.6157
Evaporator pressure	PZA003 / barg	1.88	±0.0286	5.30	± 0.049
Condenser pressure	PT006 / barg	-0.83	±0.0077	-0.65	±0.0071
MM liquid mass flow rate	FT001 / kg/h	601.08	±6.102	1347.48	±10.5
MM vapour mass flow rate	FT004 / kg/h	630.53	±8.014	1398.89	±15.55
MM liquid density	FTA001-RT001 / kg/m^3	751.34	±5.85	732.62	±5.736
MM vapour density	FT004-RT002 / kg/m^3	18.37	±1.0106	20.70	± 1.0155
MM liquid temp.	FTA001-TT017 / °C	32.33	±0.7084	50.17	± 0.95
MM vapour temp.	FT004-TT016 / °C	248.27	±2.606	251.08	±2.615

(a)

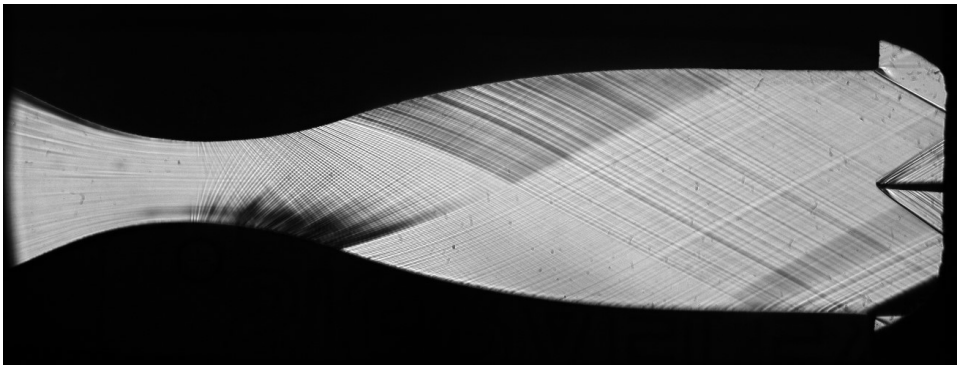

(b)

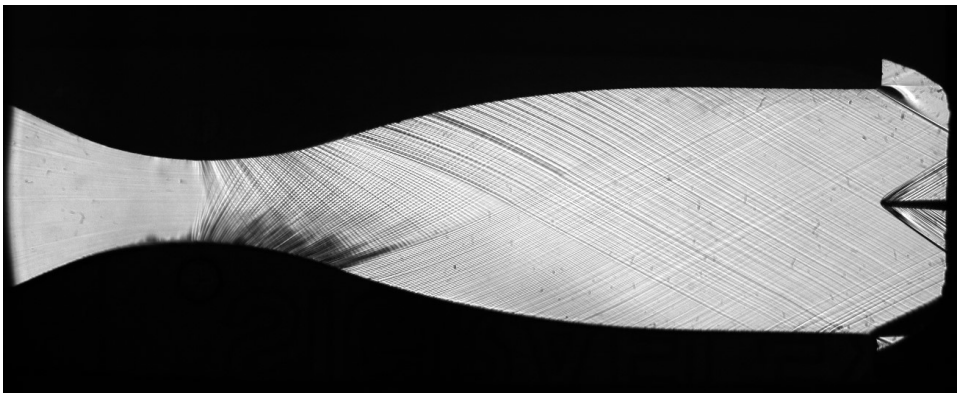

(c)

(d)

Figure 4.14: Exemplary schlieren images depicting **(a)** liquid spots and inhomogenieties during start-up, **(b)** Mach lines and oblique shock observed during isentrope A, **(c)** Mach lines and oblique shock observed during isentrope B and **(d)** a series of mach disks and a lambda shock observed during shut-down.

Table 4.12: Measured throat height during test run.

TS condition	Throat height (mm)	% offset
Calibration (180 °C)	7.713	2.85
Isentrope A (252°C)	7.629	1.72
Isentrope B (252°C)	7.629	1.72

4.6. Validation Assessment

As outlined in Sec. 2.5, a rigorous validation assessment involves a comparison of experimental and simulation averages and uncertainties. The numerical and input uncertainties for the simulations were computed for the design expansion from 18.4 bara, 252°C to 2.1 bara [13, 103]. However, at the time of writing the thesis, experiments at the design conditions were not performed. Additionally, the *Scanivalve* system was not in operation. Hence, the validation assessment adopted here only involves a comparison with deterministic simulations performed at the operating conditions for isentrope A and B listed in Tab. 4.4.

The steady-flow Reynolds averaged Navier-Stokes (RANS) simulations were performed using the open source SU2 flow solver. The Peng-Robinson EoS is used, with constant transport properties. The Spalart-Almaras (SA) model is used for turbulence closure. The advective fluxes are second order discretised according to the ROE scheme. Owing to flow symmetry, the domain is simplified to a half-nozzle profile, shown in Fig. 4.15. Reimann boundary conditions are implemented at the inlet and outlet and symmetry conditions along the mid-plane. The design throat height is 7.5 mm while the inlet and outlet heights are 25.4 and 21.4 mm. The computational domain is meshed using an unstructured grid of tetrahedrons. Following a grid convergence study on the domain [103], a mesh density of 40 k elements was found to be sufficiently mesh independent. A y^+ value less than 1 was maintained throughout the wall. To calculate the shock angle generated by the wedge, an iterative procedure using the jump conditions are implemented instead of including the wedge in the computational domain. This choice was made to avoid convergence issues arising from shock generation and to reduce the numerical uncertainty associated with the mesh generation. The iterative procedure proposed by Grossman [44] and discussed in Sec. 2.4.2 is implemented on the flow solution of a normal half-nozzle.

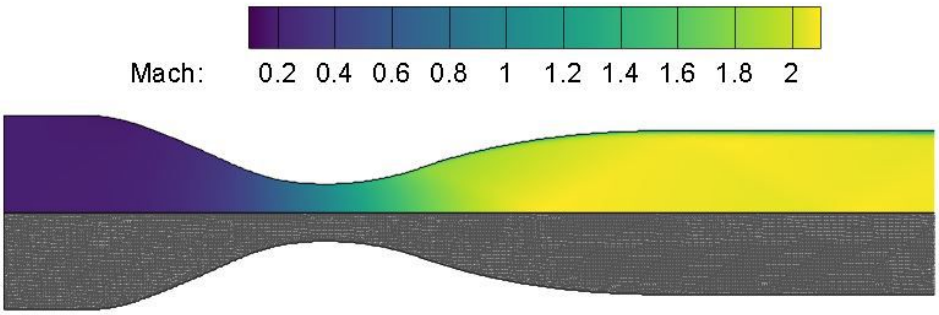

Figure 4.15: Computational domain of half nozzle profile with mesh and Mach contours for Isentrope B.

4.6.1. Flowrate and Density Validation

The mass flowrate and density is measured by *Coriolis* flowmeters in both the liquid and vapour state. The Coriolis twin tube mass flowmeter consists of two measuring tubes, a drive coil and two sensors at either side of the coil (See Fig. 4.16). When the meter is energised, the drive coil vibrates the measuring tubes causing sine wave oscillations which are monitored by the two sensors. When the fluid passes through the tubes, the coriolis effect results in a phase shift of the sine wave. The phase shift, detected by the sensors is directly proportional to the mass flow rate. Density is measured by evaluating the frequency of the vibration.

The liquid MM flowrate is measured by FT001 and is located before the evaporator section. The vapour mass flowrate is measured by FT004 and it is located right before the entrance of the nozzle test section. The measured liquid flowrate shows a deviation of 1% for isentrope A and 8% for isentrope B. The vapour flowrate deviates from simulation results by 6% for isentrope A and 12% for isentrope B.

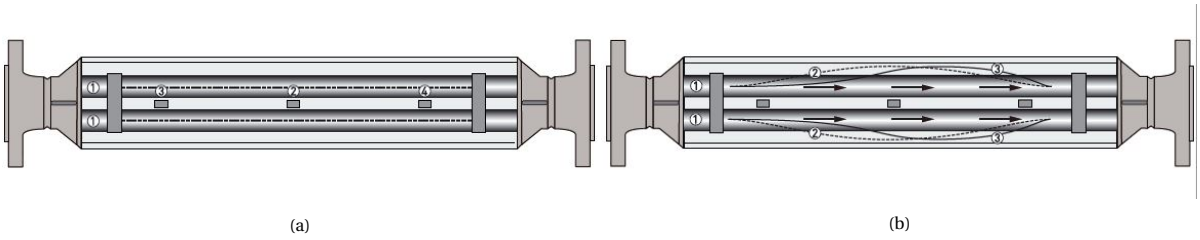

(a) (b)

Figure 4.16: Krohne Optimass 6000 flow meter cross section. **(a)** Static meter not energised and with no flow where (1) are the measuring tubes, (2) is the drive coil, (3) and (4) are the sensors. **(b)** Energised meter with process flow, where the dotted line indicates the sine wave and solid line indicates the phase shift in the sine wave. Taken from [60].

Given the 1D mass flow criteria is satisfied, the mass flow at the throat, inlet and outlet is constant. Table 4.13 reports the mass flow rates from simulations (computed at the throat) and the liquid and vapour mass flow rates measured by FT001 and FT004 respectively. It could be hypothesised that the differences in measured flowrates could be due to bleed over the main valve and due to the higher measurement accuracy of the liquid flow meter over the vapour flow meter. Given that the density calibration and measurements

Table 4.13: Validation assessment for mass flow rate- the simulation mass flow rate is computed at the throat. FT001 and FT004 are the measured liquid and vapour MM flow rates respectively. The measured values are presented along with total expanded uncertainties. The period for isentrope A extends from 16:47:00 to 16:50:00 and the period for isentrope B extends from 17:47:00 to 17:50:00. Both the periods contain 180 sample points.

	Isentrope A		
	Simulation	FT001	FT004
Mass flow rate/ kg/h	594.85	601.08 ± 6.102	630.53 ± 8.014
	Isentrope B		
	Simulation	FT001	FT004
Mass flow rate/ kg/h	1246.6	1347.48 ± 10.5	1398.89 ± 15.55

were done for the first time, the measured densities are compared against prediction from standardised tools like RefProp [64]. The thermodynamic inputs to RefProp are the pressure and temperature measurements in the respective flowmeter line. As seen in Tab. 4.14, the measured liquid densities are quite close to predicted values with less than 1% difference. The discrepancy in vapour density differences could be due to the lower measurement accuracy of the flow meter for gases. A more detailed investigation is required into the response times and accuracy of the flow meter in the vapour region. The *Coriolis* flow meters also provide

Table 4.14: Validation assessment for density - Comparison with prediction from RefProp against measured liquid and vapour MM densities. The measured values are presented along with total expanded uncertainties. The comparison error is also reported.

	Isentrope A			**Isentrope B**		
	RefProp	Measurement	Error	RefProp	Measurement	Error
ρ_{liq}/ kg/m^3	754.20	751.34 ± 5.85	0.4%	731.18	732.62 ± 5.736	0.2%
ρ_{vap}/ kg/m^3	10.50	18.37 ± 1.01	75%	24.58	20.70 ± 1.015	16%

direct temperature measurements using a Pt500 sensor which is a platinum resistance thermometer. In the same process flow line, TT015 (*WIKA TR10-H* RTD) also measures the temperature. It uses a stainless steel metal probe. Both the measured temperatures are in close agreement with each other during steady state but have different transient response times which was observed during shut down.

4.6.2. Mach Field Validation

Mach lines originating from the roughness of the nozzle profiles are visible in the exemplary schlieren images shown in Fig. 4.14. Line detection algorithms can be used to extract information on the angle of the Mach lines and estimate the local Mach number. The line detection infrastructure was developed in Beltrame [9]. It uses the Canny edge detection algorithm to detect the edge of the individual lines in the schlieren images, followed by a Hough transform on the binarised image to detect the lines. A detailed discussion on the methods is beyond the scope of the thesis and the reader is directed to Beltrame [9] for a complete de-

scription. The refinement of the line extraction results is controlled by parameters such as the interrogation window, minimum line length, pixel skip factor and peaks number. The optimisation of the binarisation process is controlled by the edge threshold, Gaussian noise filter and the adjust threshold. Manual adjustments of these parameters are done until satisfactory line detection as shown in Fig. 4.17a is achieved. The calibration procedure explained in App. B provides the scaling factor that translates the image from the pixel plane to an adimensional plane. Image rotation correction is done while acquiring the images in the LaVision DaVis software. In the processing stage, flow symmetry is detected and followed by the midplane line detection step.

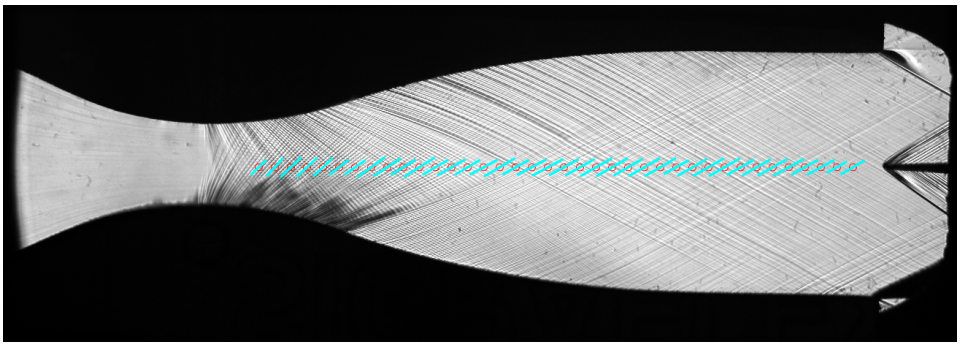

(a)

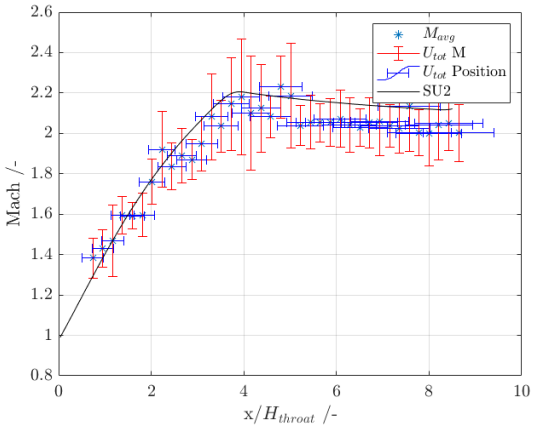

(b)

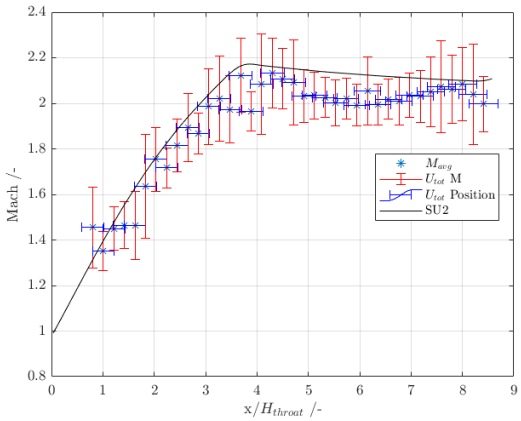

(c)

Figure 4.17: **(a)** Mach line segments identified from the post-processing algorithm superimposed on a schlieren image. Experimentally derived Mach numbers along the nozzle midplane is plotted against RANS CFD simulations done on SU2. The Mach numbers with corresponding uncertainty bars for **(b)** Isentrope A and **(c)** Isentrope B are plotted against the distance from the throat non-dimensionalised against the the throat height, H_{th}.

For an accurate comparison against numerical solutions, it is important to quantify the uncertainties arising from the post-processing process. The error bars plotted in Fig. 4.17 is composed of both *Type A* and *Type B* uncertainties. The *Type B* uncertainty inherent to the post- processing algorithm contains the uncertainty related to the position at which the Mach angle is estimated U_x and the uncertainty related to the estimation of the angle, U_μ. The uncertainty associated with the Mach angle detection can be decomposed into one associated with the image resolution, U_{ir} and one related to the Mach line angle discretisation assumed in the Hough transfer implementation, U_{Hough}. The uncertainty on the flow Mach number $U_{\text{ext, Mach}}$ is determined by propagating the uncertainty in the Mach angle measurement through Eqn. 3.18d.

$$U_{\text{ext, Mach}} = M\sqrt{M^2-1}U_{\text{ext}\,\mu} \tag{4.16}$$

where $U_{\text{ext}\,\mu}$ is the uncertainty associated with the mach angle extraction. The factor $M\sqrt{M^2-1}$ is computed by evaluating the derivative of the Mach number with respect to the Mach angle $\left|\frac{dM(\mu)}{d\mu}\right|$ [9]. The relation implies that higher uncertainties in Mach are expected at the outlet than the throat of the nozzle. Figure 4.17a shows the Mach line segments identified by the code superimposed on a Schlieren image taken during

the process run of Isentrope B. The domain was discretised into 38 windows along the x- axis where each window is populated with a Mach line.

Figures 4.17b and 4.17c plot the experimentally derived Mach numbers with uncertainty bars against CFD RANS simulations at the conditions detailed in Tab. 4.4. The values of the flow Mach number obtained from CFD simulations lie within the uncertainty bars. In previous test runs reported by A.J.Head [5, Chapter 6], a horizontal and vertical offset between the simulation and experimental values was observed close to the throat. In the current test runs, this is rectified by providing the throat height measured using the calibration block. Additionally, due to the lower degree of non-ideality associated with Isentrope A and B compared to the on-design case, the density gradients at the throat are not very steep allowing the tool to detect the Mach lines clearly. As the inlet pressures increases, it is expected that the visibility in the throat region will be lower due to stronger density gradients and significant bending of light. This can be resolved by adjusting the knife-edge and exposure of the camera.

4.6.3. Oblique Shock Validation

Section 4.6.2 dealt with the identification of Mach waves, which are weak expansion waves generated by the gradual change in geometry profile. It is accompanied by negligible pressure change i.e, $(p_1 - p_2) \sim p_1$ where subscripts 1 and 2 indicate positions before and after the Mach wave. Consequently, the entropy is almost constant and the process can be considered isentropic. But when the geometry change is sudden, as in the case of the wedge at the exit, the Mach waves coalesce to form oblique shocks which are accompanied by pressure loss and associated entropy generation. Figure 4.18a is a schlieren image of the oblique shock wave generated by a 2.5° wedge at the exit of the nozzle. The flow field contains interesting flow features such as Mach waves upstream to the wedge, the oblique shock wave generated by the tip of the wedge and an expansion fan at the end of the diverging section of the nozzle. The relation between the flow turning angle, θ and the shock angle β was discussed in Sec. 2.4. Figures 4.18b and 4.18c are the $\theta - \beta$ plots for the on design ORCHID operating conditions which correspond to Isentrope D indicated in Tab. 4.4. The curve was generated by a numerical simulation with the PR EoS and the error bars correspond to the total expanded uncertainty comprised of both numerical and input uncertainties. The reader is guided to Bills [13] and Vello [103] for a more detailed discussion on the computation of the simulation uncertainties.

The current scope of oblique shock validation is restricted only to a 2.5° half angle wedge although higher flow turning angles are planned for future experiments. Manual measurements were made on 5 random samples from schlieren images captured for Isentropes A and B. For Isentrope A a mean shock angle of 31° with a standard deviation of 1° and for isentrope B a mean shock angle of 31.2° with a standard deviation of 0.75° is reported. The higher standard deviation are attributed to human bias error. Hence, the experimental uncertainties must be systemically evaluated for a rigorous validation. Nevertheless, the measured angles are close to the predicted shock angle of 31.87° despite the off-design operating conditions. This could be attributed to the fact that the wedge is in the uniform flow zone of the nozzle, where flow is already in the ideal gas region and is dependent only on the Mach number upstream of the wedge.

The slightly lower angle measured from experiments could also be explained by the lower Mach number predicted for higher throat heights (see Fig. 4.4b). Table 4.12 reports that the actual throat height was higher than the design value of 7.5 mm, which means that the exit Mach is slightly lower than on-design conditions. This translates into a lower shock angle. In the future, a structured approach comparing different flow turning angles and moving the nozzle further into the reflex and kernel region can provide validation for shock angle predictions in the non-ideal regime. As seen in Fig. 4.18d, for smaller flow turning angles, the prediction of ideal gas and a non-ideal EoS (iPRSV EoS) are similar but they diverge for higher flower turning angles resulting in different detachment limits. This result can be experimentally verified using different half angle wedges.

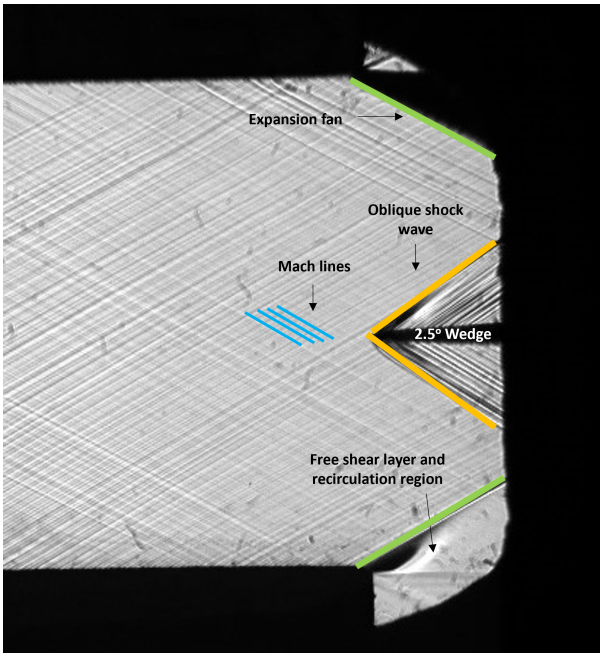

(a)

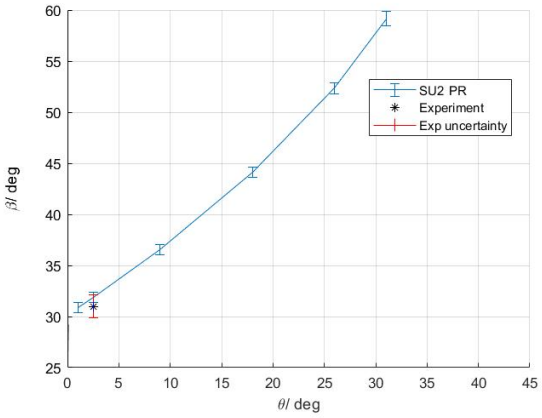

(b)

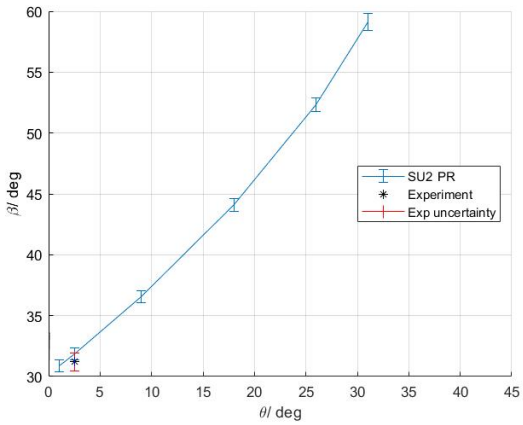

(c)

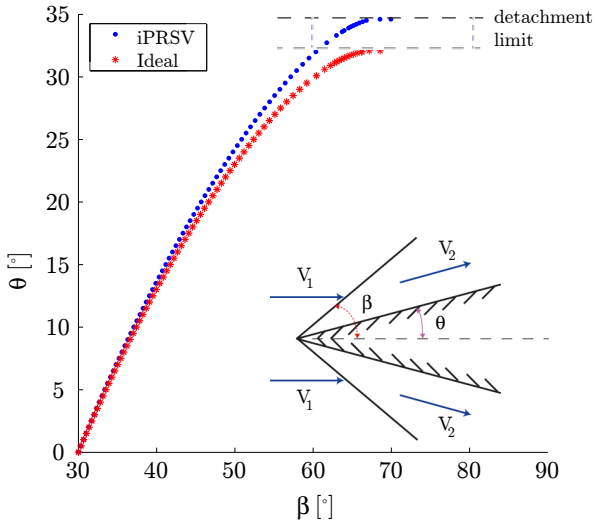

(d)

Figure 4.18: **(a)** Schlieren image of shock wave generated by a 2.5° wedge. Flow features such as shock wave, Mach lines, expansion fan and recirculation regions are indicated. $\theta - \beta$ diagram for on design conditions with total expanded numerical and input uncertainty error bars with experimental measurement of shock angle obtained for **(b)** isentrope A and **(c)** isentrope B. The experimental uncertainty indicates human measurement bias. **(d)** is the $\theta - \beta$ diagram for the MM nozzle considering the iPRSV and Ideal gas thermodynamic model. Taken from [5].

4.7. Summary

Chapter 4 began with a discussion on the state of the art experimental facilities to study NICFD flows and delved into the details of the ORCHID, at the Power & Propulsion department, TU Delft. This thesis is the first document to report the measurements from new instrumentation, specifically the total pressure sensor and the flow meter upstream to the nozzle test section. An experimental test matrix of four isentropes with increasing degree of non-idealities is proposed. In the current experimental campaign, isentrope A and B were performed with schlieren flow visualisations during the test run. A novel nozzle geometry calibration method was also implemented to measure throat heights during the experimental campaign. The optical measurement indicated that the throat height shifts during the operation of the ORCHID and this needs to be considered during the validation campaign. The heuristic steady state identification method implemented by [5] is used to identify the steady state periods. A comparison between a deterministic SU2 simulation and the measured flowrates and density show stronger agreement in the liquid state over the vapour state. This could be due to a combination of leak over the main valve and the lower measurement accuracy of the flow meter in the vapour region. The schlieren images were post-processed using an automated tool to detect the mid-channel Mach along the nozzle. The RANS CFD simulations performed at the off-design conditions yield a Mach distribution that lies within the experimental uncertainty bands. Since the UQ was done only for on-design case, the uncertainty bands do not include the input and numerical uncertainty contributions. Lastly, the oblique shock generated by a 2.5° half-angle wedge at the exit of the nozzle was manually measured. The average measured oblique shock are numerically close to the computed on design oblique shock. This can be attributed to the location of the wedge at the uniform flow region where the flow is ideal and the oblique shock angle only depends on the local Mach number, which is equal to 2 for both the experiments and on-design simulation. Further insights on the effect of non-ideal flow on the oblique shock angle can be gained from moving the wedge into the reflex or kernel region and by increasing the wedge angles.

4.7.1. Recommendations for future experimental campaigns

- During the experiments, it was observed that the *Viton* gaskets leaked and solidified into the grooves between the nozzle profile and the nozzle housing, making the removal of the profiles difficult. Given the material properties of the gasket, it also displayed thermal degradation which affected its ability to hold the nozzle profiles at the required throat height. On one instance, gasket failure was also observed. Hence, it is a worthwhile search to replace the *Viton* gasket with other alternatives available in the market like *Kalrez*.

- During the schlieren imaging campaign, it was suggested that the calibration procedure be done when the MM vapour enters the test section. This could refine the calibration image. At the time of performing the experiments, the geometry and schlieren images were not simultaneously controlled. Issues related to the same were resolved with changing the operating system and connecting a PTU unit and it is now possible to capture images and calibrate them simultaneously within the *DaVis* environment. This will help avoid any possible loss of images and information.

- In the future, Background oriented schlieren (BOS) and Particle image velocimetry (PIV) campaigns are planned. BOS belongs to the same family as schlieren imaging and provides optical density measurements from an image cross-correlation between two static images. The reference image is an undistorted background image and the target image is a distorted background image due to the density changes in the fluid [47]. The existing infrastrcuture at the ORCHID can be easily adapted for BOS making it a logical next step in the validation of NICFD flows with local density measurements as repsonse functions. Although literature on dense gas BOS visualisations are scarce, vaidation exercises have been done for simple supersonic flows [101, 104]. In addition to the two-dimensional absolute density measurements from BOS, PIV campaigns can provide accurate velocity measurements. In combination with existing Mach detection infrastructure, this could provide an indirect method of computing the speed of sound through the nozzle. Challenges related to PIV experiments in NICFD flows was studied by [61] using a non-intrusive vapour analyser. A recent work by Spinelli *et al.* [38] reports direct velocity measurements using the laser Doppler velocimetry technique. A novel atomising device which injects TiO_2 tracer particles into the flow ahead of the test section was designed and commissioned for three test cases. Satisfactory agreement was reported with CFD velocity predictions with a maximum deviation of 6.6% for the supersonic accelerating flow test case.

- In both the commissioning experiments at the ORCHID and the experiments reported in this thesis, a

combination of methods from [63] and [108] was implemented to detect the steady state time interval. The threshold values used are facility specific and there is a need to implement more industry standardised steady state identification methods. Under a strict definition , a steady state is the period in which a property, K of the system is time invariant ($\frac{\partial K}{\partial t} = 0$). This is impractical to satisfy in an experimental campaign and this constraint is relaxed. As an alternative to the method used by [108] and explained in Sec. 4.5.1, methods based on F-tests, t- tests, hotelling T^2 tests etc. exist [63]. Also, comparison of moving standard deviations to threshold reference values implemented by [57] can be used to identify steady state. Another method is the R-test, proposed by [15] which uses a ratio of variances as an evaluation metric. This approach was also applied by [12] to a micro-ORC test bench setup. For a more rigorous detection of steady state, the following approach can be adopted:

- Manual estimation of steady state using Woodland's criteria or visual observation of the process variable. This manual estimation of steady state comes also from experience of the operator with the process. For instance, at the ORCHID a settling time of around 20 - 30 minutes is given for the process variables to stabilise and the period following the settling time can be considered as a candidate period for initial steady state. This initial estimation also depends on the process equipment of interest and empirical time periods are reported in technical documents and standards from ASHRAE.
- A reference standard deviation in the identified period multiplied by a factor of 2 or 3 can be used as a threshold. The selection of an appropriate threshold is key to avoid detecting drift/ transient data or neglect steady state data. The reference standard deviation can be calculated from an evaluation of the statistical convergence of the process variable during the steady state period.
- Compute the forward moving standard deviation over the dataset. The process to be adopted is explained in [63] and [57]. The windows with a standard deviation lesser than the threshold value can be considered steady state.

5

Conclusions

The work done in the thesis dealt with characterising expansions in the non-ideal compressible flow regime through a study on two paradigmatic test cases namely, the linear stator cascade and the converging - diverging (CD) nozzle. Flow through the linear cascade blade row was studied numerically using the open-source flow solver, SU2 while the expansions through the CD nozzle was approached from an experimental perspective. Study of such paradigmatic test cases is essential in understanding the flow physics in a stator of a radial ORC turbine and determine the validity of thermodynamic, turbulence and transport sub-models. Validated models are crucial to achieving efficient and reliable expander designs. The thesis contributes to advancing the overarching research objective of validating the SU2 flow solver for NICFD applications. Hence an attempt has been made to answer the research questions presented in Sec. 1.2. The findings of the thesis are presented below:

1. ***What are the relevant system response quantities to characterise the performance of the stator?***
   Following a thorough literature review, the pressure loss coefficient, entropy loss coefficient, kinetic energy loss coefficient, base pressure loss coefficient and standard deviation of Mach and flow angle were identified as significant to characterise the stator performance. The baseline design of the stator has a pressure loss coefficient of 6.25%, entropy loss coefficient of 11.24 % , base pressure loss coefficient of -7.8% and a standard deviation of $\pm$1.182 and $\pm$0.0257 for exit flow angle and Mach. Experimentally, it is possible to measure the pressure loss coefficients and exit flow uniformity parameters with a combination of static pressure measurements, schlieren flow visualisations and planned particle image velocimetry (PIV) experiments. Additionally, with BOS experiments, it is also possible to extract information on point-wise density of the flow field. The robustness of the stator design was evaluated by a uncertainty quantification study with input uncertainties of inlet pressure, critical point properties and viscosity. The Sobol indices indicate the dominant influence of critical point properties over other inputs selected. Hence, the accurate determination of critical temperature and pressure is crucial to NICFD expansions.

2. ***What are the optimal design of experiments needed to assess the capabilities of the adjoint-based solver?***
   An unconstrained deterministic adjoint shape optimisation with the objective function to reduce entropy generation was performed on the baseline stator design which resulted in a 4% improvement in the pressure loss coefficient and 0.5% improvement in entropy loss coefficient. The unconstrained nature of the optimisation resulted in a compromise on flow uniformity properties with 31.5% increase in exit flow angle standard deviation. The UQ study performed on the optimised geometry revealed minimal robustness improvements. However, any strong conclusions on improvements in robustness from a deterministic optimisation cannot be made. For a more rigorous comparison, stochastic or multi-point optimised designs need to be compared. Nevertheless, the geometry changes arising from the optimisation exercise are too negligible to achieve given the available machining tolerances. It is possible that the current stator is the optimum design and future efforts can be directed to exploring rotor blade rows.

3. ***Can the shockwave angle be accurately quantified and provide useful information for code validation? What is the impact of nozzle geometry on response quantities?***

The ORCHID is a state of the art high temperature ORC test facility where currently fundamental dense gas expansion studies are done through temperature, pressure, flowrate , density measurements and flow field visualisation of a CD nozzle. In the present work, two isentropic expansions of pressure ratio of 8.76 from initial pressure of 2.73 bara and 6 bara are reported. The experimental data was post-processed using a heuristic method to identify steady-state for both the isentropes.

Type A and Type B uncertainties were computed and an improved data acquisition (DAQ) uncertainty calculation was reported. For the first time, vapour density and flowrate and total pressure at the inlet of the nozzle was measured. The comparison of the total pressure at the nozzle inlet and the evaporator pressure indicates that the pressure drop across the piping and valves before the inlet of the nozzle increases with mass flow rate. Thus, the previous estimate of 0.7 barg used in validation studies was a conservative value. Ideally, the liquid and vapour mass flow rates must be equal but around 5% difference is reported. This could be due to bleed over the main valve and the higher measurement accuracy of the liquid flowmeter. The measured liquid MM flowrate shows a maximum deviation of 8% from simulation value. The measured density values were compared against RefProp predictions and satisfactory agreement exists for liquid density measurements. However, the vapour density flowrates are significantly different from the thermodynamic calculation and this could be attributed to the instrument sensitivity and accuracy. The Mach field information was extracted from the schlieren images using a line extraction tool and is in agreement with the CFD results. Oblique shock angles generated by the 2.5° half-angle wedge were manually measured. The average shock angle reported for the two isentropes are 31° and 31.2°. The measured angles are less than 2% deviant from on-design (18.4 bara) shock angle predictions. This is due to the position of the wedge at the exit where the flow is already ideal and the shock angle depends only on the upstream Mach number which is 2 for all the cases due to the consistent pressure ratio.

The thesis also reports a novel method to characterise the geometry of the nozzle in real time using a calibration plate. This allows the determination of the nozzle throat height which is crucial to validation studies since change in area ratio of the nozzle affects the Mach and pressure distribution measured. It was observed that the throat height at the start of the experiments was offset by around 2.85% from the design height of 7.5 mm. During the experiments, this reduced to 1.72% due to thermal expansion of the profiles and degradation of the gaskets. For a 0.5 mm throat height shift, the choked mass flow rate changes by 6.7%. Given the sensitivity of the Mach number to the throat height, it is essential that the mechanical stability of the nozzle profiles is ensured by selecting appropriate gasket materials or installing a mechanical stop.

A

Process & Instrumentation diagram of the ORCHID

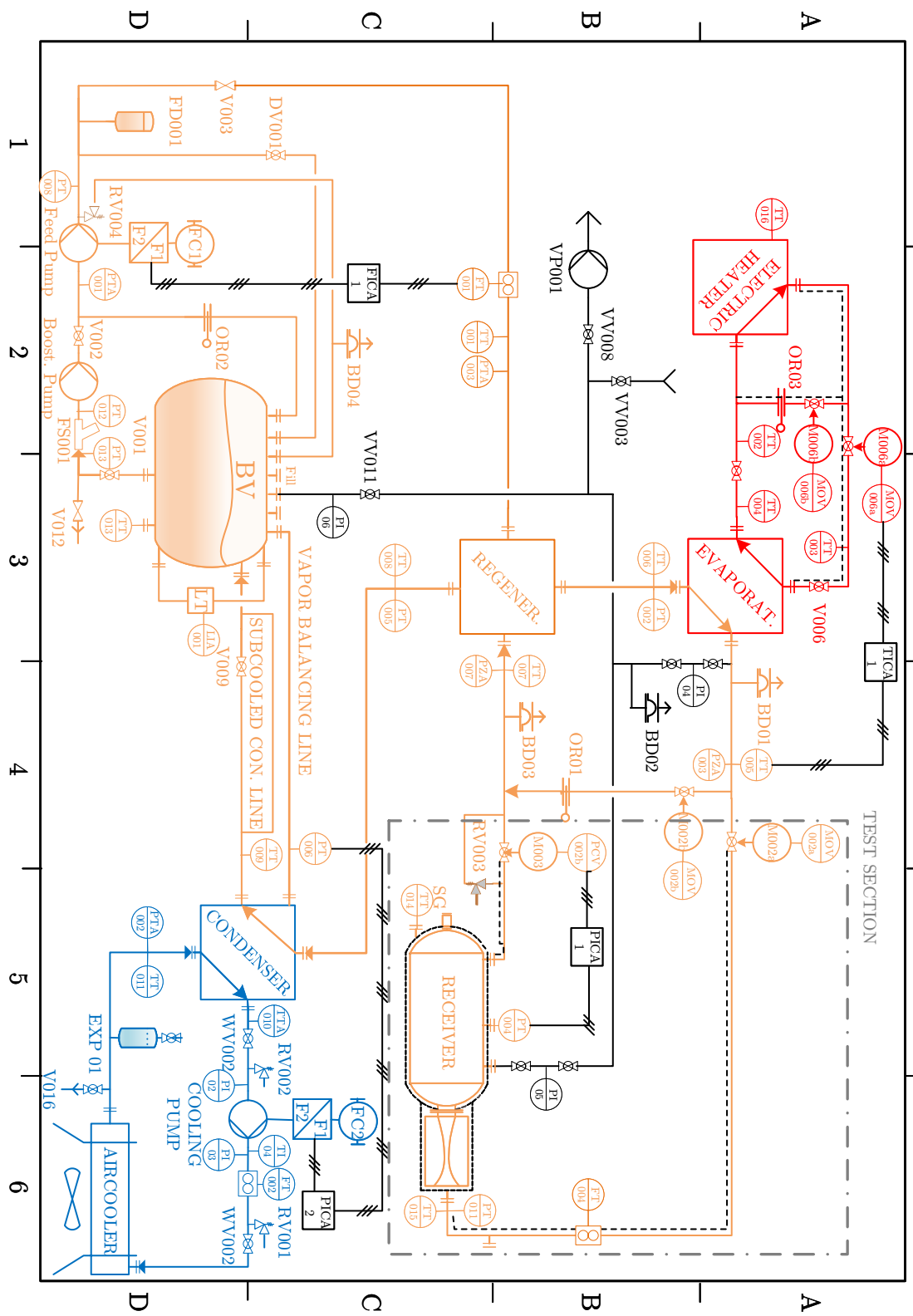

Figure A.1: Piping and Instrumentation Diagram (P&ID) of the ORCHID. Reproduced from [5].

B

Detailed procedure for nozzle calibration

The detailed calibration process described below converts .bmp images to im7 format with shift correction and conversion from pixel to mm space. The process below has to be done for both the cameras.

1. A calibration plate of dimensions 107.15 mm x 28.44 mm with marker dots of thickness 0.3mm and spacing 1mm is used. The number of markers in the x - direction is 107 and in the y - direction is 27. The calibration design is then applied to the negative of the converging-diverging nozzle.

2. Two calibration images are acquired with the block in the mid-plane for the Schlieren camera and the block at the plane of the crosses for the geometry camera.

3. Next, the raw acquired images which are in .bmp format need to be calibrated. For this, first import the calibration image and the Schlieren images. The pixel size used is 7.4 μm.

4. For the calibration, click on scaling -> Calibration using displayed images. Create a new single-plane 2D calibration plate by entering the marker dot properties. The thickness needs to be 1 mm.

5. Set the mapping function as Pinhole and define the orientation such that the resultant image matches with actual flowfield direction. To find the marks, apply a masking to narrow the region of interest. Start the search and the software now identifies the markers. This can be adjusted in the user defined settings tab to adjust the sensitivity of the calibration. The calibration step is complete.

6. Within the processing tab, apply shift correction first and follow that by selecting the image mapping function and applying the image correction (raw->world).

7. Apply the active calibration for all the images and the corrected images will be saved in im7 format that can then be fed into the MATLAB line extraction code.

8. Given that the images have been converted to mm space, it is possible to use the corrected geometry camera images to note the coordinates of the two crosses and compute the throat height.

C

Type A Uncertainties

The Type A uncertainties associated with all the process variables for Isentropes A and B recorded over the steady state period identified in Sec.4.5.1 are reported below.

Table C.1: Averages and Type A expanded uncertainties of the process variables for Isentrope A. Values are computed over the reference period from 16:47:00 to 16:50:00 at 1Hz, i.e., 180 samples. Refer to App.A for instrument identification by their tags.

Temperatures					
Tag	T / °C	$U_{\text{Type A}}$ / ± °C *	Tag	T / °C	$U_{\text{Type A}}$ / ± °C *
TT001	32.0998	0.042	TTA009	29.72	0.19
TT002	270.48	0.09	TTA010	26.12	0.30
TT003	275.10	0.04	TT011	24.05	0.37
TT004	258.27	0.23	TT013	30.28	0.04
TT005	254.32	0.21	TT014	240.04	0.61
TT006	138.04	0.06	TT015	252.72	0.27
TT007	231.29	0.73	FT004-TT016	248.27	0.42
TT008	57.76	0.48	FTA001-TT017	32.33	0.03
Pressures					
Tag	P / barg	$U_{\text{Type A}}$ / ± bar *	Tag	P / barg	$U_{\text{Type A}}$ / ± bar *
PT002	1.86	0.02	PT004	-0.77	0.00
PT005	-0.79	0.00	PT006	-0.83	0.00
PT008	2.12	0.29	PT011	1.71	0.02
PT012	-0.70	0.02	PT013	-0.63	0.02
PTA001	0.81	0.06	PTA002	0.07	0.01
PTA003	1.90	0.02	PTA009	4.04	0.00
PTA010	22.61	0.06	PZA003	1.88	0.02
PZA007	-0.07	0.00			
Flow Rates					
Tag	Avg. Flow rate	$U_{\text{Type A}}$ / ± *			
FT001	601.08	3.90 kg/h			
FT002	629.88	1.83 l/s			
FT004	630.53	4.95 kg/h			
Density					
Tag	Avg. Density / kg/m^3	$U_{\text{Type A}}$ / ± kg/m^3 *			
FT004-RT002	18.37	0.02			
FTA001-RT001	751.34	0.06			

* Coverage factor $k = 2$. The reported values are the absolute expanded uncertainties associated to the Type A errors.

Table C.2: Averages and Type A expanded uncertainties of the process variables for Isentrope B. Values are computed over the reference period from 17:47:00 to 17:50:00 at 1Hz, i.e., 180 samples. Refer to App.A for instrument identification by their tags.

Temperatures					
Tag	T / °C	$U_{\text{Type A}}$ / ± °C *	Tag	T / °C	$U_{\text{Type A}}$ / ± °C *
TT001	49.56	0.45	TTA009	53.28	0.38
TT002	269.48	0.15	TTA010	37.88	0.32
TT003	277.14	0.12	TT011	30.49	0.24
TT004	268.79	0.50	TT013	50.34	0.48
TT005	252.57	0.29	TT014	245.40	0.16
TT006	169.08	0.27	TT015	253.22	0.29
TT007	241.82	0.12	FT004-TT016	251.08	0.29
TT008	84.06	1.50	FTA001-TT017	50.17	0.43
Pressures					
Tag	P / barg	$U_{\text{Type A}}$ / ± bar *	Tag	P / barg	$U_{\text{Type A}}$ / ± bar *
PT002	5.30	0.03	PT004	-0.31	0.00
PT005	-0.61	0.00	PT006	-0.65	0.00
PT008	5.66	0.13	PT011	4.98	0.03
PT012	-0.51	0.07	PT013	-0.45	0.08
PTA001	0.96	0.13	PTA002	0.50	0.01
PTA003	5.29	0.03	PTA009	4.03	0.00
PTA010	22.61	0.07	PZA003	5.30	0.03
PZA007	-0.07	0.00			
Flow Rates					
Tag	Avg. Flow rate	$U_{\text{Type A}}$ / ± *			
FT001	1347.48	1.18 kg/h			
FT002	353.59	1.00 l/s			
FT004	1398.89	6.93 kg/h			
Density					
Tag	Avg. Density / kg/m^3	$U_{\text{Type A}}$ / ± kg/m^3 *			
FT004-RT002	20.70	0.02			
FTA001-RT001	732.62	0.06			

* Coverage factor $k = 2$. The reported values are the absolute expanded uncertainties associated to the Type A errors.

D

Solver Configuration Files

```
%%%%%%%%%%%%%%%%%%%%%%%%%%%%%%%%%%%%%%%%%%%%%%%%%%%%%%%%%%%%%%%%%%%%%%%%%%%%%%%%
%                                                                              %
% SU2 configuration file                                                       %
% Case description: Airfoil RANS ORCHID                                        %
% Author: R. Vello                                                             %
% Institution: Delft University of Technology                                  %
% Date: Feb 28th, 2020                                                         %
% File Version 5.0.0 "Raven"                                                   %
%                                                                              %
%%%%%%%%%%%%%%%%%%%%%%%%%%%%%%%%%%%%%%%%%%%%%%%%%%%%%%%%%%%%%%%%%%%%%%%%%%%%%%%%

% ------------- DIRECT, ADJOINT, AND LINEARIZED PROBLEM DEFINITION ------------%
PHYSICAL_PROBLEM= RANS
KIND_TURB_MODEL= SA
MATH_PROBLEM= DIRECT
RESTART_SOL= YES

% -------------------- COMPRESSIBLE FREE-STREAM DEFINITION --------------------%
MACH_NUMBER= 0.05
AoA= 0.0
FREESTREAM_PRESSURE= 1840000.0
FREESTREAM_TEMPERATURE= 523
FREESTREAM_DENSITY= 122
FREESTREAM_TURBULENCEINTENSITY = 0.1
FREESTREAM_TURB2LAMVISCRATIO = 100.0
FREESTREAM_OPTION= TEMPERATURE_FS
INIT_OPTION= TD_CONDITIONS

% ---------------------- REFERENCE VALUE DEFINITION ---------------------------%
REF_DIMENSIONALIZATION= DIMENSIONAL

% --------------------------------- FLUID MODEL -------------------------------%
FLUID_MODEL= PR_GAS
GAMMA_VALUE= 1.025
GAS_CONSTANT= 51.2
CRITICAL_TEMPERATURE= 518.75
CRITICAL_PRESSURE= 1939000.0
ACENTRIC_FACTOR= 0.418

% --------------------------- VISCOSITY MODEL ---------------------------------%
VISCOSITY_MODEL= CONSTANT_VISCOSITY
MU_CONSTANT= 1.354E-5
MU_REF= 1.716E-5
MU_T_REF= 273.15
SUTHERLAND_CONSTANT= 110.4

% --------------------------- THERMAL CONDUCTIVITY MODEL ----------------------%
CONDUCTIVITY_MODEL= CONSTANT_PRANDTL
```

```
KT_CONSTANT= 0.03547

% ------------------- BOUNDARY CONDITION DEFINITION -------------------------%
MARKER_HEATFLUX= ( wall1, 0.0 )
MARKER_GILES= ( inflow, TOTAL_CONDITIONS_PT, 1840000.0, 525.15, 1.0, 0.0, 0.0,...
1.0, 0.0, outflow, STATIC_PRESSURE, 195000, 0.0, 0.0, 0.0, 0.0, 1.0, 0.0 )
SPATIAL_FOURIER = YES
AVERAGE_PROCESS_KIND= MIXEDOUT
TURBOMACHINERY_KIND= AXIAL
NUM_SPANWISE_SECTIONS= 1
RAMP_OUTLET_PRESSURE= YES
RAMP_OUTLET_PRESSURE_COEFF= (1500000.0, 100.0, 1000)
MARKER_PERIODIC= (periodic1, periodic2, 0.0, 0.0, 0.0, 0.0, 0.0, 0.0, 0.0, 0.045, 0.0)

% ----------------------- SURFACES IDENTIFICATION --------------------------%
MARKER_PLOTTING= ( wall1, periodic1, outflow )
MARKER_MONITORING= ( wall1, periodic1, outflow )
MARKER_TURBOMACHINERY= ( inflow, outflow )

% ------------------------ GRID ADAPTATION STRATEGY -------------------------%
KIND_ADAPT= PERIODIC

% ------------ COMMON PARAMETERS DEFINING THE NUMERICAL METHOD --------------%
NUM_METHOD_GRAD= WEIGHTED_LEAST_SQUARES
CFL_NUMBER= 5.0
CFL_ADAPT= NO

% ----------------------- LINEAR SOLVER DEFINITION -------------------------%
LINEAR_SOLVER= FGMRES
LINEAR_SOLVER_PREC= LU_SGS
LINEAR_SOLVER_ERROR= 1E-4
LINEAR_SOLVER_ITER= 5

% ------------------------ MULTIGRID PARAMETERS ----------------------------%
MGLEVEL= 0

% ----------------------- SLOPE LIMITER DEFINITION -------------------------%
VENKAT_LIMITER_COEFF= 0.5

% -------------------- FLOW NUMERICAL METHOD DEFINITION --------------------%
CONV_NUM_METHOD_FLOW= JST
MUSCL_FLOW= YES
ENTROPY_FIX_COEFF= 0.1
JST_SENSOR_COEFF= ( 0.5, 0.12 )
SLOPE_LIMITER_FLOW= VAN_ALBADA_EDGE
TIME_DISCRE_FLOW= EULER_IMPLICIT
RELAXATION_FACTOR_FLOW= 0.6

% -------------------- TURBULENT NUMERICAL METHOD DEFINITION ----------------%
CONV_NUM_METHOD_TURB= SCALAR_UPWIND
MUSCL_TURB = YES
SLOPE_LIMITER_TURB= VENKATAKRISHNAN
TIME_DISCRE_TURB= EULER_IMPLICIT
CFL_REDUCTION_TURB= 0.01
RELAXATION_FACTOR_TURB= 0.6

% ------------------------- CONVERGENCE PARAMETERS -------------------------%
EXT_ITER= 200000
CONV_CRITERIA= RESIDUAL
RESIDUAL_FUNC_FLOW= RHO
RESIDUAL_REDUCTION= 9999
RESIDUAL_MINVAL= -6.25
STARTCONV_ITER= 10
CAUCHY_ELEMS= 100
CAUCHY_EPS= 1E-6
CAUCHY_FUNC_FLOW= DRAG

% ------------------------ INPUT/OUTPUT INFORMATION ------------------------%
MESH_FILENAME= su2mesh_per.su2
MESH_FORMAT= SU2
MESH_OUT_FILENAME= su2mesh_per.su2
```

```
SOLUTION_FLOW_FILENAME= restart_flow.dat
OUTPUT_FORMAT= TECPLOT
CONV_FILENAME= history
RESTART_FLOW_FILENAME= restart_flow.dat
VOLUME_FLOW_FILENAME= flow
SURFACE_FLOW_FILENAME= surface_flow
WRT_SOL_FREQ= 100
WRT_CON_FREQ= 10
```

Bibliography

[1] Calibration procedure NI 9208 16-channel, 20ma, 24-bit analog input module. Technical report.

[2] Standard for verification and validation in computational fluid dynamics and heat transfer. Technical report, American Society of Mechanical Engineers (ASME), 2009.

[3] RB Abernethy, RP Benedict, and RB Dowdell. Asme measurement uncertainty. 1985.

[4] BM Adams, LE Bauman, WJ Bohnhoff, KR Dalbey, MS Ebeida, JP Eddy, MS Eldred, PD Hough, KT Hu, JD Jakeman, et al. Dakota: a multilevel parallel object-oriented framework for design optimization, parameter estimation, etc.: Version 6.0 user's manual. *Sandia National Lab. Tech. Rept. SAND2014-4633, Albuquerque, New Mexico*, 2015.

[5] A.J.Head. *Novel Experiments for the Investigation of NonIdeal Compressible Fluid Dynamics: The ORCHID and First Results of Optical Measurements*. PhD thesis, 2020.

[6] John D Anderson. *Modern compressible flow*. Tata McGraw-Hill Education, 2003.

[7] Gianfranco Angelino and Piero Colonna Di Paliano. Multicomponent working fluids for organic rankine cycles (orcs). *Energy*, 23(6):449–463, 1998.

[8] JS Bahamonde Noriega. *Integrated Design Methods for Mini Organic Rankine Cycle Power Systems*. PhD thesis, Delft University of Technology, 2018.

[9] Fabio Beltrame. Accuracy assessment of the su2 flow solver for non-ideal organic vapour supersonic expansions using experiemntal data. Master's thesis, TU Delft, 03 2020.

[10] Robert M Bethea and R Russell Rhinehart. *Applied engineering statistics*. Routledge, 2019.

[11] Shrikant A Bhat and Deoki N Saraf. Steady-state identification, gross error detection, and data reconciliation for industrial process units. *Industrial & engineering chemistry research*, 43(15):4323–4336, 2004.

[12] M Bianchi, L Branchini, A De Pascale, V Orlandini, S Ottaviano, A Peretto, F Melino, M Pinelli, PR Spina, and A Suman. Experimental investigation with steady-state detection in a micro-orc test bench. *Energy Procedia*, 126:469–476, 2017.

[13] Liam Bills. Validation of the SU2 flow solver for classical non ideal compressible fluid dynamics. Master's thesis, 2020.

[14] IEC BIPM, ILAC IFCC, IUPAC ISO, and OIML IUPAP. Evaluation of measurement data—supplement 2 to the 'guide to the expression of uncertainty in measurement'—extension to any number of output quantities. *JCGM*, 102:2011, 2011.

[15] Songling Cao and R Russell Rhinehart. An efficient method for on-line identification of steady state. *Journal of Process Control*, 5(6):363–374, 1995.

[16] M Chidambaram. Basics of data acquisition and control. In *Handbook of networked and embedded control systems*, pages 227–257. Springer, 2005.

[17] Ting Horng Chung, Mohammad Ajlan, Lloyd L Lee, and Kenneth E Starling. Generalized multiparameter correlation for nonpolar and polar fluid transport properties. *Industrial & engineering chemistry research*, 27(4):671–679, 1988.

[18] Paola Cinnella, Pietro Congedo, Laura Parussini, and Valentino Pediroda. Quantification of uncertainties in compressible flows with complex thermodynamic behavior. In *19th AIAA Computational Fluid Dynamics*, page 3670. 2009.

[19] Paola Cinnella, Pietro Marco Congedo, Valentino Pediroda, and Lucia Parussini. Sensitivity analysis of dense gas flow simulations to thermodynamic uncertainties. *Physics of Fluids*, 23(11):116101, 2011.

[20] E Richard Cohen. Error and uncertainty in physical measurements. In *Modeling Complex Data for Creating Information*, pages 55–64. Springer, 1996.

[21] Hugh W Coleman and W Glenn Steele. *Experimentation, validation, and uncertainty analysis for engineers*. John Wiley & Sons, 2018.

[22] P Colonna, NR Nannan, ALBERTO Guardone, and Eric W Lemmon. Multiparameter equations of state for selected siloxanes. *Fluid Phase Equilibria*, 244(2):193–211, 2006.

[23] P Colonna, NR Nannan, A Guardone, and TP Van der Stelt. On the computation of the fundamental derivative of gas dynamics using equations of state. *Fluid phase equilibria*, 286(1):43–54, 2009.

[24] P Colonna, TP van der Stelt, and A Guardone. Fluidprop (version 3.0): A program for the estimation of thermophysical properties of fluids. *Asimptote, Delft, The Netherlands, http://www. fluidprop. com*, 2012.

[25] Piero Colonna, Emiliano Casati, Carsten Trapp, Tiemo Mathijssen, Jaakko Larjola, Teemu Turunen-Saaresti, and Antti Uusitalo. Organic rankine cycle power systems: from the concept to current technology, applications, and an outlook to the future. *Journal of Engineering for Gas Turbines and Power*, 137(10), 2015.

[26] Computational Fluid Dynamics Committee. Guide: Guide for the verification and validation of computational fluid dynamics simulations (aiaa g-077-1998 (2002)), 1998.

[27] Pietro Marco Congedo. *Contributions to the reliability of numerical simulations in fluid mechanics. Application to the flow simulation of thermodynamically complex gases*. PhD thesis, Université Sciences et Technologies-Bordeaux I, 2013.

[28] MS Cramer and AB Crickenberger. Prandtl-meyer function for dense gases. *AIAA journal*, 30(2):561–564, 1992.

[29] Zuna Dardi. Mechanical design of the linear cascade. Master's thesis, InHolland, 1 2021.

[30] Michiel Van de Groen. The design of a cascade vapor tunnel test section. Master's thesis, InHolland, 1 2021.

[31] Carlo M De Servi, Matteo Burigana, Matteo Pini, and Piero Colonna. Design method and performance prediction for radial-inflow turbines of high-temperature mini-organic rankine cycle power systems. *Journal of Engineering for Gas Turbines and Power*, 141(9), 2019.

[32] J Denton. *Loss mechanisms in turbomachines*, volume 78897. American Society of Mechanical Engineers, 1993.

[33] JD Denton and L Xu. The trailing edge loss of transonic turbine blades. 1990.

[34] Luis Eça and Martin Hoekstra. A procedure for the estimation of the numerical uncertainty of cfd calculations based on grid refinement studies. *Journal of computational physics*, 262:104–130, 2014.

[35] Thomas D Economon, Francisco Palacios, Sean R Copeland, Trent W Lukaczyk, and Juan J Alonso. Su2: An open-source suite for multiphysics simulation and design. *Aiaa Journal*, 54(3):828–846, 2016.

[36] Clemens Forman, Ibrahim Kolawole Muritala, Robert Pardemann, and Bernd Meyer. Estimating the global waste heat potential. *Renewable and Sustainable Energy Reviews*, 57:1568–1579, 2016.

[37] Simone Gallarini, Andrea Spinelli, Fabio Cozzi, and A Guardone. Design and commissioning of a laser doppler velocimetry seeding system for non-ideal fluid flows. 2016.

[38] Simone Gallarini, Fabio Cozzi, Andrea Spinelli, and Alberto Guardone. Direct velocity measurements in high-temperature non-ideal vapor flows. *Experiments in Fluids*, 62(10):1–18, 2021.

[39] Pablo Garrido de la Serna. Adjoint-based 3d shape optimization for turbomachinery applications. 2019.

[40] Michael Giles. *Non-reflecting boundary conditions for the Euler equations*. Computational Fluid Dynamics Laboratory, Department of Aeronautics and ..., 1988.

[41] Michael Giles. Unsflo: A numerical method for the calculation of unsteady flow in turbomachinery. Technical report, Cambridge, Mass.: Gas Turbine Laboratory, Massachusetts Institute of ..., 1991.

[42] Richard J Goldstein and TH Kuehn. Optical systems for flow measurement: Shadowgraph, schlieren, and interferometric techniques. In *Fluid Mechanics Measurements*, pages 451–508. Routledge, 2017.

[43] Giulio Gori, Marta Zocca, Giorgia Cammi, Andrea Spinelli, Pietro Marco Congedo, and Alberto Guardone. Accuracy assessment of the non-ideal computational fluid dynamics model for siloxane mdm from the open-source su2 suite. *European Journal of Mechanics-B/Fluids*, 79:109–120, 2020.

[44] B Grossman. Fundamental concepts of real gasdynamics. In *Technical Report*. Virginia Polytechnic Institute and State University, 2000.

[45] Alberto Guardone, Andrea Spinelli, and Vincenzo Dossena. Influence of molecular complexity on nozzle design for an organic vapor wind tunnel. *Journal of engineering for gas turbines and power*, 135(4), 2013.

[46] Emil Haur. Designing of the rotating cascade test section for the TU Delft ORCHID facility. Master's thesis, InHolland, 1 2021.

[47] Keisuke Hayasaka and Yoshiyuki Tagawa. Mobile visualization of density fields using smartphone background-oriented schlieren. *Experiments in Fluids*, 60(11):1–15, 2019.

[48] Adam Joseph Head, Carlo De Servi, Emiliano Casati, Matteo Pini, and Piero Colonna. Preliminary design of the orchid: a facility for studying non-ideal compressible fluid dynamics and testing orc expanders. In *Turbo Expo: Power for Land, Sea, and Air*, volume 49743, page V003T25A001. American Society of Mechanical Engineers, 2016.

[49] AJ Head, Matteo Novara, Mauro Gallo, Ferdinand Schrijer, and Piero Colonna. Feasibility of particle image velocimetry for low-speed unconventional vapor flows. *Experimental Thermal and Fluid Science*, 102:589–594, 2019.

[50] Samuel J Hercus and Paola Cinnella. Robust shape optimization of uncertain dense gas flows through a plane turbine cascade. In *Fluids Engineering Division Summer Meeting*, volume 44403, pages 1739–1749, 2011.

[51] Charles Hirsch. Advanced methods for cascade testing. *NASA STI/Recon Technical Report N*, 94:15119, 1993.

[52] Marcia L Huber, Arno Laesecke, and Richard A Perkins. Model for the viscosity and thermal conductivity of refrigerants, including a new correlation for the viscosity of r134a. *Industrial & engineering chemistry research*, 42(13):3163–3178, 2003.

[53] International Organization for Standardization (ISO). Guide to the expression of uncertainty in measurement. *Guide* 100:2008, Joint Committee for Guides in Metrology, 1993. JCGM. Corrected and reprinted, 1995.

[54] Mohammad Ariful Islam, Keishi Kariya, Hirotaka Ishida, Ryo Akasaka, and Akio Miyara. Application of the extended corresponding states model for prediction of the viscosity and thermal conductivity of cis-1, 3, 3, 3-tetrafluoropropene (r1234ze (z)). *Science and Technology for the Built Environment*, 22(8): 1167–1174, 2016.

[55] Siddharth Iyer. Influence of Thermodynamic Property Perturbations on Nozzle Design and Non-Ideal Compressible Flow Phenomena. Master's thesis, 2015.

[56] A Javed. Developing generic design expertise for gas turbine engines: Robust design of a micro centrifugal compressor. 2014.

[57] Minsung Kim, Seok Ho Yoon, Piotr A Domanski, and W Vance Payne. Design of a steady-state detector for fault detection and diagnosis of a residential air conditioner. *International journal of refrigeration*, 31(5):790–799, 2008.

[58] Dimitrios A Kouremenos and Xenofon K Kakatsios. Ideal gas relations for the description of the real gas isentropic changes. *Forschung im Ingenieurwesen A*, 51(6):169–174, 1985.

[59] Leslie SG Kovasznay. The hot-wire anemometer in supersonic flow. *Journal of the Aeronautical Sciences*, 17(9):565–572, 1950.

[60] *OPTIMASS 6000 Technical Datasheet*. Krohne, 3 2021. Rev. 5.

[61] Harshil Lakkad. NICFD and the PIV technique: Feasibility in low speed and high speed flows. Master's thesis, TU Delft, 10 2017.

[62] Sigurd Yves Larsen, Raymond D Mountain, and Robert Zwanzig. On the validity of the lorentz—lorenz equation near the critical point. *The Journal of Chemical Physics*, 42(6):2187–2190, 1965.

[63] Steven Lecompte, Sergei Gusev, Bruno Vanslambrouck, and Michel De Paepe. Experimental results of a small-scale organic rankine cycle: Steady state identification and application to off-design model validation. *Applied Energy*, 226:82–106, 2018.

[64] Eric W Lemmon, Marcia L Huber, and Mark O McLinden. Nist reference fluid thermodynamic and transport properties–refprop. *NIST standard reference database*, 23:v7, 2002.

[65] Hendrik Antoon Lorentz. Ueber die beziehung zwischen der fortpflanzungsgeschwindigkeit des lichtes und der körperdichte. *Annalen der Physik*, 245(4):641–665, 1880.

[66] E Macchi. Design criteria for turbines operating with fluids having a low speed of sound. *Von Karman Inst. for Fluid Dyn. Closed Cycle Gas Turbines,*, 2, 1977.

[67] T Mathijssen, M Gallo, E Casati, NR Nannan, C Zamfirescu, A Guardone, and P Colonna. The flexible asymmetric shock tube (fast): a ludwieg tube facility for wave propagation measurements in high-temperature vapours of organic fluids. *Experiments in Fluids*, 56(10):1–12, 2015.

[68] Ian A McLure and Eric Dickinson. Vapour pressure of hexamethyldisiloxane near its critical point: corresponding-states principle for dimethylsiloxanes. *The Journal of Chemical Thermodynamics*, 8(1): 93–95, 1976.

[69] Wolgang Merzkirch. *Flow visualization*. Elsevier, 2012.

[70] Robert J Moffat. Describing the uncertainties in experimental results. *Experimental thermal and fluid science*, 1(1):3–17, 1988.

[71] Michael J Moran, Howard N Shapiro, Daisie D Boettner, and Margaret B Bailey. *Fundamentals of engineering thermodynamics*. John Wiley & Sons, 2010.

[72] Pim Nederstigt. Real gas thermodynamics: and the isentropic behavior of substances. 2017.

[73] Richard G Newell and Daniel Raimi. Global energy outlook comparison methods: 2020 update, 2020.

[74] Pradipta Kumar Panigrahi and Krishnamurthy Muralidhar. *Schlieren and shadowgraph methods in heat and mass transfer*, volume 2. Springer, 2012.

[75] Ashish Patel, Rafael Diez, Rene Pecnik, et al. Turbulence modelling for flows with strong variations in thermo-physical properties. *International Journal of Heat and Fluid Flow*, 73:114–123, 2018.

[76] M Pianko and F Wazelt. Propulsion and energetics panel working group 14 on suitable averaging techniques in non-uniform internal flows. Technical report, ADVISORY GROUP FOR AEROSPACE RESEARCH AND DEVELOPMENT NEUILLY-SUR-SEINE (FRANCE), 1983.

[77] M Pini, G Persico, and Vincenzo Dossena. Robust adjoint-based shape optimization of supersonic turbomachinery cascades. In *Turbo Expo: Power for Land, Sea, and Air*, volume 45615, page V02BT39A043. American Society of Mechanical Engineers, 2014.

[78] Matteo Pini, S Vitale, Piero Colonna, Giulio Gori, A Guardone, T Economon, JJ Alonso, and F Palacios. Su2: the open-source software for non-ideal compressible flows. In *Journal of Physics: Conference Series*, volume 821, page 012013. IOP Publishing, 2017.

[79] Bruce E Poling, John M Prausnitz, and John P O'connell. *Properties of gases and liquids*. McGraw-Hill Education, 2001.

[80] A PRACTICAL GUIDE TO A PROSPEROUS, LOW CARBON EUROPE, and WWW ROADMAP2050 EU. Roadmap 2050.

[81] F. De Raedt. Non-reflecting boundary conditions for non-ideal compressible fluid flows, 2015.

[82] Nassim Razaaly, Giulio Gori, Olivier Le Maitre, Gianluca Iaccarino, and Pietro Marco Congedo. Robust optimization of orc turbine cascades operating with siloxane mdm. In *CTR Summer Program 2018*, 2018.

[83] Felix Reinker, Eugeny Y Kenig, and Stefan aus der Wiesche. Clowt: A multifunctional test facility for the investigation of organic vapor flows. In *Fluids Engineering Division Summer Meeting*, volume 51562, page V002T14A004. American Society of Mechanical Engineers, 2018.

[84] Felix Reinker et al. Application of hot-wire anemometry in the high subsonic organic vapor flow regime. In *International Seminar on Non-Ideal Compressible-Fluid Dynamics for Propulsion & Power*, pages 135–143. Springer, 2020.

[85] Miles Robertson, Peter Newton, Tao Chen, Aaron Costall, and Ricardo Martinez-Botas. Experimental and numerical study of supersonic non-ideal flows for organic rankine cycle applications. *Journal of Engineering for Gas Turbines and Power*, 142(8), 2020.

[86] Alessandro Romei, Pietro Marco Congedo, and Giacomo Persico. Assessment of deterministic shape optimizations within a stochastic framework for supersonic organic rankine cycle nozzle cascades. *Journal of Engineering for Gas Turbines and Power*, 141(7), 2019.

[87] Alessandro Romei, Davide Vimercati, Giacomo Persico, and Alberto Guardone. Non-ideal compressible flows in supersonic turbine cascades. *Journal of Fluid Mechanics*, 882, 2020.

[88] Spencer L Seager and Michael R Slabaugh. *Chemistry for today: General, organic, and biochemistry*. Cengage Learning, 2013.

[89] Aldo Serafino. *Multi-fidelity Robust Design Optimization Methods for Organic Rankine Cycles*. PhD thesis, HESAM Université, 2020.

[90] Gary S Settles. Schlieren and shadowgraph techniques- visualizing phenomena in transparent media(book). *Berlin, Germany: Springer-Verlag GmbH, 2001.*, 2001.

[91] C Sieverding, M Decuyper, J Colpin, and O Amana. Model tests for the detailed investigation of the trailing edge flow in convergent transonic turbine cascades. In *Turbo Expo: Power for Land, Sea, and Air*, volume 79740, page V01AT01A030. American Society of Mechanical Engineers, 1976.

[92] Aleksandr Vladimirovich Smol'yakov and Viktor Mikhailovich Tkachenko. Measurement of turbulent fluctuations. In *The Measurement of Turbulent Fluctuations*, pages 46–128. Springer, 1983.

[93] Philippe Spalart and Steven Allmaras. A one-equation turbulence model for aerodynamic flows. In *30th aerospace sciences meeting and exhibit*, page 439, 1992.

[94] Roland Span and Wolfgang Wagner. A new equation of state for carbon dioxide covering the fluid region from the triple-point temperature to 1100 k at pressures up to 800 mpa. *Journal of physical and chemical reference data*, 25(6):1509–1596, 1996.

[95] Andrea Spinelli, Matteo Pini, Vincenzo Dossena, Paolo Gaetani, and Francesco Casella. Design, simulation, and construction of a test rig for organic vapors. *Journal of engineering for gas turbines and power*, 135(4), 2013.

[96] Bertrand F Tchanche, Pierre Loonis, Mathieu Pétrissans, and Harry Ramenah. Organic rankine cycle systems principles, opportunities and challenges. In *2013 25th International Conference on Microelectronics (ICM)*, pages 1–4. IEEE, 2013.

[97] Simen Tennoe, Geir Halnes, and Gaute T Einevoll. Uncertainpy: a python toolbox for uncertainty quantification and sensitivity analysis in computational neuroscience. *Frontiers in neuroinformatics*, 12:49, 2018.

[98] Philip A Thompson. A fundamental derivative in gasdynamics. *The Physics of Fluids*, 14(9):1843–1849, 1971.

[99] Valentina Valori. Rayleigh-bénard convection of a supercritical fluid: Piv and heat transfer study. 2018.

[100] TP Van der Stelt, NR Nannan, and P Colonna. The iprsv equation of state. *Fluid phase equilibria*, 330: 24–35, 2012.

[101] Nils Paul Van Hinsberg and Thomas Rösgen. Density measurements using near-field background-oriented schlieren. *Experiments in fluids*, 55(4):1–11, 2014.

[102] An Van Schepdael, Aurélie Carlier, and Liesbet Geris. Sensitivity analysis by design of experiments. In *Uncertainty in Biology*, pages 327–366. Springer, 2016.

[103] Riccardo Vello. A validation infrastructure for non-ideal compressible fluid dynamics with applications to orc turbines. Master's thesis.

[104] L Venkatakrishnan and GEA Meier. Density measurements using the background oriented schlieren technique. *Experiments in Fluids*, 37(2):237–247, 2004.

[105] Salvatore Vitale, Giulio Gori, Matteo Pini, Alberto Guardone, Thomas D Economon, Francisco Palacios, Juan J Alonso, and Piero Colonna. Extension of the su2 open source cfd code to the simulation of turbulent flows of fuids modelled with complex thermophysical laws. In *22nd AIAA Computational Fluid Dynamics Conference*, page 2760, 2015.

[106] Wayne W Wakeland, Robert H Martin, and David Raffo. Using design of experiments, sensitivity analysis, and hybrid simulation to evaluate changes to a software development process: a case study. *Software Process: Improvement and Practice*, 9(2):107–119, 2004.

[107] EL Warrick. The application of bond refractions to organo-silicon chemistry. *Journal of the American Chemical Society*, 68(12):2455–2459, 1946.

[108] Brandon J Woodland, James E Braun, Eckhard A Groll, and W Travis Horton. Experimental testing of an organic rankine cycle with scroll-type expander. 2012.